

**Calcined clays as supplementary cementitious materials:
raw material characterization, reactivity and impact on the early
hydration and sulfate demand**

Matthias Maier

Vollständiger Abdruck der von der Fakultät für Bauingenieurwesen und Umweltwissenschaften
der Universität der Bundeswehr München zur Erlangung des akademischen Grades eines

Doktors der Naturwissenschaften (Dr. rer. nat.)

genehmigten Dissertation.

Gutachter/Gutachterin:

1. Univ.-Prof. Dr.-Ing. Karl-Christian Thienel
2. Prof. Dr. rer. nat. Jürgen Neubauer
3. Prof. Dr. Alisa Machner

Die Dissertation wurde am 09.05.2022 bei der Universität der Bundeswehr München
eingereicht und durch die Fakultät für Bauingenieurwesen und Umweltwissenschaften
am 12.07.2022 angenommen. Die mündliche Prüfung fand am 29.07.2022 statt.

Danksagung

Ich möchte mich zuallererst bei Professor Dr.-Ing. Karl-Christian Thienel für die ausgezeichnete Betreuung der Arbeit bedanken. Das große Vertrauen, welches er mir durch die Freiheit zur Entwicklung eigener Forschungsideen entgegenbrachte, sowie die stetige Diskussionsbereitschaft und Unterstützung bei deren Umsetzung, waren der Grundstein für diese Arbeit.

Prof. Dr. Alisa Machner und Prof. Dr. Jürgen Neubauer danke ich für das Interesse, die Arbeit zu begutachten und die spannende Diskussion in der Prüfung.

Des Weiteren möchte ich mich bei Dr.-Ing. Nancy Beuntner bedanken, die mit ihrem enormen Einsatz für das ganze Institut dafür sorgt, dass der wissenschaftliche Betrieb läuft und gleichzeitig ständige Ansprechpartnerin für fachliche genauso wie persönliche Anliegen ist.

Bei meinen Kolleginnen und Kollegen bedanke ich mich für die einzigartige Arbeitsatmosphäre. Dr. Sebastian Scherb danke ich dafür, dass er jederzeit für ausgedehnte Diskussionen von Forschungsideen, Versuchsplänen, Mess- (und Fußball) - ergebnissen zur Verfügung stand und somit diese Arbeit wesentlich bereichert hat. Bei Ricarda Sposito möchte ich mich für die Anregung zu den gemeinsamen Publikationen und die durchwegs angenehme und bereichernde Arbeit daran bedanken. Caro Chucholowski, Timo Haller, Abubakar Muhammad, Paul Waibl und Johannes Berger danke ich für die super Zusammenarbeit und stets gute Stimmung im Büro! Trotz Pandemie und Lockdowns blieb das ganze Institut immer in engem Kontakt.

Dem gesamten Laborteam möchte ich für die Unterstützung bei meinen Versuchen danken, insbesondere Dr. Mathias Köberl für die Hilfe bei der Thermoanalyse und FTIR Spektroskopie, Karola Feldmann für die vielen Calcinierungen und chemischen Analysen, Wolfgang Saur für die Unterstützung am REM und Thomas Pohl für die BET Messungen.

Professor Dr. Steffen Krause und seinen Mitarbeiterinnen am Institut für Siedlungswasserwirtschaft danke ich für die unkomplizierte Zusammenarbeit bei den Analysen mittels ICP-OES und Lasergranulometrie.

Mein ganz besonderer Dank gilt meiner Familie, vor allem meiner Frau Caroline und meinen Kindern Laura, Leopold und Moritz. Ihr seid stets mein größter Ansporn und mein ganzer Stolz!

Abstract

The aimed reduction of carbon dioxide emission resulting from cement production requires an increasing substitution of cement clinker by supplementary cementitious materials (SCMs). The group of materials that holds the greatest potential in serving this demand are calcined clays, which therefore attracted much attention from researchers during the past decade. However, the great diversity of clay resources together with their mineralogical complexity on the one hand and open questions regarding their impact on hydration mechanisms on the other, are still factors preventing a more widespread use. This thesis therefore aims at improving the knowledge concerning the influence of clay mineralogy on the pozzolanic reactivity and the mechanisms regarding the impact of calcined clays on the early cement hydration.

The first part of the work presents an evaluation of methods for the characterization and reactivity assessment of common clays that are available as raw materials for calcined clays. While a major part of previous studies focused on kaolinitic clays, this study also includes common clays dominated by 2:1 clay minerals. A multiple-technique approach comprising quantitative XRD analysis implementing structure models that consider different types of disorder, complemented by thermal analysis and infrared spectroscopy, enables a reliable mineralogical characterization of the raw clays. The influence of 2:1 clay minerals on the pozzolanic reactivity is clearly verified while stacking disorder in kaolinite influences the rate of heat development but not the cumulative heat during R^3 test. Solubility measurements of aluminum and silicon and R^3 -test provide consistent results and are proven to be suitable for the assessment of common clays in a wide range of mineralogical compositions.

The second part of the work deals with the influence of calcined clays on early cement hydration, with a special focus on the aluminate reaction. Investigations in a C_3A model system containing calcium sulfate allow the examination of their exclusive impact on the early aluminate reaction. Calcined kaolinite and illite are shown to drastically accelerate the C_3A dissolution and the associated ettringite formation, while limestone does not. This observation is related to a preferable adsorption of calcium and sulfate ions or ion pair complexes onto the surface of the calcined clay minerals, which is strongly related to their surface charge and area.

The acceleration of the aluminate reaction in a blended Portland limestone cement is attributed to the same mechanisms so that previously produced theories based on the SCM's alumina content or accelerated C-S-H precipitation through the filler effect have to be extended by direct ion adsorption onto calcined clays. The filler effect of calcined clays is lower than it would be expected based on their large specific surface area in comparison to limestone. The influence of aluminum ions provided by the metakaolin is considered minor with regard to the acceleration of sulfate depletion but enhances the sulfate requirement for a proper resulfation of blended cement. This effect is most evident in the C_3A model system.

The new findings can improve the assessment of potential raw materials for the production of calcined clays and increase the knowledge required for an optimal mix design of calcined clay blended cement.

Kurzfassung

Calcinierter Tone gelten als die aussichtsreichsten Kandidaten, um die steigende Nachfrage nach Zementersatzstoffen im Zuge der CO₂-Reduktionsstrategie der Zementindustrie zu bedienen. Da Tone aufgrund ihrer diversen mineralogischen Zusammensetzung ein breites Spektrum an Eigenschaften aufweisen, stellen die Bewertung der Reaktivität und der veränderten Reaktionsmechanismen in zementären Systemen eine große Herausforderung dar. Die vorliegende Arbeit zielt ab auf ein verbessertes Verständnis der Zusammenhänge zwischen Tonmineralogie und puzzolaner Reaktivität sowie der Mechanismen, welche den Einfluss calcinierter Tone auf die frühe Zementhydratation erklären.

Im ersten Teil der Arbeit werden Methoden für die Charakterisierung und Beurteilung der Reaktivität von potentiellen Rohstoffen für die Produktion calcinierter Tone evaluiert. Während sich ein Großteil früherer Studien auf kaolinitische Tone konzentrierte, umfasst diese Studie auch Tonvorkommen mit hohen Anteilen an Dreischichttonmineralen. Die Anwendung von quantitativer XRD-Analyse unter Verwendung von Strukturmodellen für fehlgeordnete Tonminerale liefert, ergänzt durch Thermoanalyse und Infrarotspektroskopie, eine zuverlässige und umfängliche mineralogische Charakterisierung der Rohtone. Der Einfluss von 2:1-Tonmineralen auf die puzzolane Reaktivität wird eindeutig nachgewiesen, während der Fehl Ordnungsgrad in Kaolinit vor allem die Geschwindigkeit der Wärmeentwicklung, nicht aber die Gesamtwärme während des R³-Tests beeinflusst. Die Bestimmung der Löslichkeit von Aluminium und Silizium und der R³-Test liefern konsistente Ergebnisse und eignen sich nachweislich für die Bewertung von Tönen mit einem breiten Spektrum an mineralogischer Zusammensetzungen.

Der zweite Teil der Arbeit befasst sich mit dem Einfluss von calcinierten Tönen auf die frühe Zementhydratation, wobei der Schwerpunkt auf der aluminatischen Reaktion liegt. Die Entwicklung eines C₃A Modellsystems ermöglicht die Untersuchung der Auswirkungen ausschließlich auf die frühe aluminatische Reaktion. Es zeigt sich, dass die Auflösung von C₃A und die damit einhergehende Ettringitbildung durch calcinierten kaolinitischen und illitischen Ton gleichermaßen beschleunigt wird, während dies für Calcit nicht beobachtet wird. Diese Mechanismen werden einer bevorzugten Adsorption von Calcium- und Sulfationen oder Ionenpaarkomplexen auf der negativ geladenen Oberfläche der calcinierten Tonminerale zugewiesen. Die Beschleunigung der aluminatischen Reaktion in einem Portlandkalksteinzement, substituiert mit 30 % calciniertem Ton, bestätigt die im Modellsystem beschriebenen Mechanismen. Theorien aus vorangehenden Studien, welche auf dem Aluminiumgehalt des SCM oder der beschleunigten C-S-H-Bildung basieren, müssen somit um die direkte Adsorption von Sulfat auf den Oberflächen calcinierter Tone erweitert werden. Der Einfluss von zusätzlichem Aluminium aus dem Metakaolin wird im Hinblick auf die Beschleunigung der Sulfatträgerauflösung als gering eingestuft, erhöht jedoch den Sulfatbedarf für eine optimale Resultatisierung des Zements. Dieser Effekt zeigt sich am deutlichsten im C₃A Modellsystem.

Die Erkenntnisse dieser Arbeit ermöglichen eine systematische Bewertung potentieller Rohstoffe für die Herstellung calcinierter Tone. Ferner liefern sie wichtige Grundlagen für die gezielte Einstellung der Eigenschaften von Kompositzementen mit calcinierten Tönen.

Table of Contents

Danksagung	I
Abstract	II
Kurzfassung	III
Table of Contents	IV
Glossary	VI
List of Figures	VIII
1 Introduction	1
1.1 Background	1
1.2 Objective of the thesis	2
2 State of knowledge	3
2.1 Clays	3
2.1.1 Definition and classification of clays	3
2.1.2 Formation and occurrence of clay deposits	3
2.1.3 Structural characterization of clay minerals	5
2.1.4 Thermal treatment of clay minerals	6
2.1.5 Properties of (calcined) clay particles in suspensions	8
2.1.6 Particle characteristics of clay minerals	9
2.1.7 Mineralogical characterization of clays by X-ray powder diffraction	9
2.2 Portland cement hydration	10
2.2.1 Cement hydration in general	10
2.2.2 Aluminate reaction	11
2.3 Supplementary cementitious materials (SCMs)	12
2.3.1 Classification of SCMs	12
2.3.2 Reactivity tests for SCMs	13
2.3.3 Physical reaction mechanisms	13
2.3.4 Chemical reaction mechanisms	14
2.3.5 Impact of calcined clays on early hydration	15
2.3.6 Impact of calcined clays on phase assemblage	16
3 Summary of the methods applied	17

4	Main results	19
4.1	Mineralogical properties determining the reactivity of calcined clays	19
4.1.1	Mineralogical characterization of the raw materials.....	19
4.1.2	Assessment of reactivity	21
4.2	Impact of calcined clays on the early cement hydration	23
4.2.1	The relation of surface area and filler effect	24
4.2.2	Acceleration of the aluminate reaction	26
4.3	Mechanisms behind the increased sulfate demand of calcined clay blended cements.....	29
5	Conclusion	32
6	Perspectives.....	33
7	References	34
8	Publications	41
8.1	Mineralogical characterization and reactivity test of common clays suitable as supplementary cementitious material.....	41
8.2	Hydration of cubic tricalcium aluminate in the presence of calcined clays.....	54
8.3	Influence of particle characteristics of calcined clays and limestone on the early hydration and sulfate demand of blended cement.....	70
9	Appendix	86

Glossary

Cement chemistry notation

C	CaO
S	SiO ₂
A	Al ₂ O ₃
F	Fe ₂ O ₃
H	H ₂ O
\bar{S}	SO ₃
c	CO ₂

Cement phase notation

C ₃ S	Tricalcium silicate (alite)
C ₂ S	Dicalcium silicate (belite)
C ₃ A	Tricalcium aluminate
C ₄ AF	Tetracalcium aluminoferrite
C-S-H	Calcium silicate hydrate
C-A-S-H	Calcium aluminum silicate hydrate
CAH	Calcium aluminate hydrate
CH	Calcium hydroxide (portlandite)
C ₄ AcH ₁₁	Monocarboaluminate (AFm-Mc)
C ₄ Ac _{0.5} H _{11.5}	Hemicarboaluminate (AFm-Hc)
C ₄ A \bar{S} ₁₂	Monosulfoaluminate (AFm-Ms)
C ₆ A \bar{S} ₃ H ₃₂	Ettringite (AFt)
C ₃ AH ₆	Hydrogarnet (katoite)
C \bar{S}	Calcium sulfate (anhydrite)
C \bar{S} H _{0.5}	Calcium sulfate hemihydrate (bassanite)
C \bar{S} H ₂	Calcium sulfate dihydrate (gypsum)
AS ₂	Metakaolin

Methods abbreviations

ATR	Attenuated total reflection
BET	Specific surface area after Brunauer, Emmett and Teller
FTIR	Fourier transformed infrared spectroscopy
(hkl)	Miller indices
ICP-OES	Inductively coupled plasma optical emission spectrometry
TG/DTG	Thermogravimetry / differential thermogravimetry
PSD	Particle size distribution
R ³	R ³ reactivity test
SEM	Scanning electron microscopy
SSA	Specific surface area
XRD	X-ray diffraction

Other abbreviations

AGFI	Aparicio-Galán-Ferrell index
CC	Calcined clay
CI	Calcined illitic clay
CKc	Calcined coarse kaolinitic clay
CKf	Calcined fine kaolinitic clay
di	Diocahedral
DoH	Degree of hydration
FWHM	Full width at half maximum
LC ³	Limestone calcined clay cement

LS	Limestone
μLS	Micro limestone
MK	Metakaolin
OPC	Ordinary portland cement
P ₀	FTIR-based index for degree of disorder in kaolinite
PLC	Portland limestone cement
SCM	Supplementary cementitious material
tri	Trioctahedral
wt%	Percentage by weight
ξ	Layer charge

List of Figures

- Figure 1** Global distribution of clay-sized mineral groups in the top- and subsoil (modified after Ito & Wagai [23])..... 4
- Figure 2** Geological map of Germany 1:1,000,000 with deposits of clay and claystone, active clay pits and cement plants (adapted from [26]). 4
- Figure 3** The basic structural components of clay minerals: a) a sheet of corner-linked tetrahedra, where the red spheres represent oxygen atoms and the sphere in the center of the tetrahedra show silicon atoms and b) the edge-sharing octahedral sheet with a six-fold coordinated cation (e.g. Al^{3+}) in the center of the octahedra. The figures were drawn using the VESTA software on the basis of the kaolinite structure model [30]. 5
- Figure 4** Simplified illustration of the course of the calcined clay's pozzolanic reactivity as a function of calcination temperature (Modified after [39])..... 7
- Figure 5** Simplified illustration of the arrangement of clay layers (a) to form particles (b), aggregates (c) and assemblies of aggregates (d), leading to different kinds of pores in clays (redrawn after [16]). 9
- Figure 6** Exemplary heat flow curve during the early hydration of an ordinary Portland cement including the shoulder peak corresponding to secondary ettringite precipitation and the subsequent broad peak representing AFm phase formation (redrawn after [79] and [88]. I: initial period, II: dormant or induction period, III: main period, IIIa: accelerating period, IIIb: decelerating period. 11
- Figure 7** Mechanisms explaining the filler effect of SCMs in blended cement (drawn according to descriptions in [110, 112-114]). 14
- Figure 8** Reaction degree of different SCM in comparison to alite provided by Skibsted and Snellings [33]. 15
- Figure 9** Diffractogram of a texture specimen of the < 2 μm fraction of a smectite-rich marl (MOSM) under air-dried (AD) and glycolated (EG) conditions. 20
- Figure 10** Peak deconvolution according the proposed procedure by Aparicio et al [78] for a poorly (a, FUP), a moderately (b, KBZ) and a highly ordered kaolinite (c, KK) using the program Fityk [139]. The green line represents the fitted kaolinite peaks and the light grey line the fitted peaks of secondary phases and the background. The red line marks the sum of the curves and the dark grey line the difference between measured and fitted curve. 20
- Figure 11** Rietveld refinement for a common clay containing illite-smectite interstratifications (a, "AC") and a kaolinite-rich clay with moderately disordered kaolinite modeled by a combination of an ideal and a disordered kaolinite structure (b, "KBZ") [141]. 21
- Figure 12** Correlation between calcined kaolinite content determined based on the initial kaolinite content as determined by TGA and XRD and the reactivity

	based on the evolved heat after 3 days R^3 reactivity test (modified after [141]).....	22
Figure 13	Connection between degree of order in kaolinite determined by the amount quantified by the ordered structure model (a), the AGFI index (b) and the P_0 -index (c) and heat flow maximum during R^3 calorimetry test.....	22
Figure 14	Heat flow curves of a) PLC blended with 30 wt% of calcined clays and limestone without extra sulfate dosage and b) PLC_CC82 with different amounts of added sulfate carrier [143].	23
Figure 15	Chemical reactivity of the investigated clays in the C_3A model system using R^3 test and solubility in the alkaline model solution (MOH) [144].	24
Figure 16	Correlation of the SSA of the systems blended with μLS and different calcined clays (CC) with the appearance of the heat flow maximum of the silicate reaction. The maxima were determined in the systems with adjusted sulfate carrier from chapter 8.3.....	25
Figure 17	SEM images of the used μLS (a) and CC69 (b), underlining the strong agglomeration of the clay platelets to form larger particles (the scale applies for both images; modified after [143])	26
Figure 18	Phase development and heat flow curves in the C_3A model systems with 5 wt% $C\bar{S}$ a) without calcined clay (Ref 5%), b) with 20 wt% CKf, c) with 20 wt% CI and d) with 20 wt% CKc [144]	27
Figure 19	Correlation between combined SSA of C_3A model systems Ref, CKc, CKf and CI and the maximum of sulfate depletion peak (SDP) (modified after [144]). Variation of SSA was realized by using different replacement levels between 5 and 30 wt% Further details are given in chapter 8.2.....	28
Figure 20	Correlation of SO_3 content (taking into account the SO_3 bound by ettringite) and amount of reacted C_3S at the aluminate onset [143].....	29
Figure 21	Model of adsorption mechanisms inhibiting the retardation of C_3A hydration in the C_3A -Quartz-Gypsum system (a) and the C_3A -Quartz-Gypsum-MK system (b).	30
Figure 22	Evolved heat of the C_3A model systems with a) 20 wt% calcined fine kaolinitic clay (CKf) and b) 20 wt% of calcined illitic clay (CI) and different amounts of $C\bar{S}$. (c) provides the ettringite formation in the C_3A model systems with 20 wt% $C\bar{S}$ and 20 wt% CKf or 20 wt% CI.....	31

1 Introduction

1.1 Background

Concrete is the most manufactured product on earth on a volumetric scale [1]. Cement, the commonly used binder in concrete, is currently produced in a quantity of 4 gigatonnes (GT) per year [2]. Neither common construction materials can be increased in a quantity that would be sufficient to replace a major part of currently used concrete, nor alternative clinker or binder are believed to replace a significant amount of cement in the short- or mid-term [3]. For this reason, and in the face of the huge demand for building materials in emerging countries, cement production is expected to further increase between 12 and 23 % by 2050 [1]. The production of one ton of Portland cement clinker generates about 0.84 tons of CO₂ on average, of which about two thirds are ascribed to limestone decomposition [3]. Since cement producers are therefore currently responsible for about 6 – 7 % of global anthropogenic CO₂ emissions [4], their sense of urgency is obvious with regards to the goal of greenhouse gas neutrality by 2050. In order to meet this obligation, cement industry focuses on different strategies, following the technology roadmap provided by the International Energy Agency (IEA) [1]. One of them is the implementation of carbon capture, usage and storage technology (CCUS), which is however considered as a mid-till-long-term solution and, due to the high expense, the least favored option.

The short-term solution with the greatest potential of CO₂ mitigation is a further reduction of the clinker content in cement. Until today, this was achieved for the most part by using two groups of industrial side streams as supplementary cementitious materials (SCMs) [5]: fly ash from coal combustion and ground granulated blast furnace slag from pig iron production. As the availability of these materials is going to decline or even disappear in a carbon neutral economy, there is an urgent need for alternatives.

The only suitable materials, which are available in a sufficient quantity during the next decades are natural fillers (e.g. limestone powder) or calcined clays. While the replacement of cement through limestone powder or other fillers is limited concerning strength and durability, the implementation of calcined clays alone or in combination with limestone can provide significant contribution to strength development by densifying the microstructure [6, 7]. Even though a strong focus of the cement research community on this subject has increased knowledge regarding reactivity assessment and reaction mechanisms of calcined clays in cementitious systems dramatically during the past decade (e.g. [8-11]), there are still important gaps to be closed.

These include on the one hand the suitability of available resources of common clays as SCMs and appropriate assessment methods. This issue is addressed in the first part of the thesis, where clays from geologically diverse deposits are extensively characterized concerning their mineralogical composition and assessed regarding their pozzolanic reactivity. On the other hand, the influence of calcined clays on the early hydration of blended cements, which is still considered as one of their challenges, is not yet completely understood. This concerns especially the aluminat clinker reaction, which is significantly altered in the presence of calcined clay minerals, particularly metakaolin. Consequently, the second and major part of this thesis focusses on the mechanisms that influence the C₃A hydration in calcined clay blended cementitious systems.

1.2 Objective of the thesis

The general objective of this thesis is to improve the understanding of suitability of common clay resources as raw materials for the production of calcined clays as SCM on the one hand, and on the other to gather further insights into the influence of calcined clays on the early cement hydration, with focus on the aluminate reaction. Therefore, the following research questions were addressed:

1. How is the pozzolanic reactivity after calcination linked to the mineralogical characteristics of the raw clays?
2. Which methods are suitable to assess these parameters?
3. How do different types of calcined clays influence the hydration of the clinker phases in blended cement?
4. What are the mechanisms behind the accelerated aluminate reaction and the associated increased sulfate demand in calcined clay blended cement?

These questions were processed in three peer-reviewed journal papers that are provided in chapter 8. The main outcomes of these papers are discussed in chapter 4.

2 State of knowledge

2.1 Clays

2.1.1 Definition and classification of clays

The definition of the term clay has been widely discussed throughout the past, however, today most clay scientists unite behind the definition proposed by the “Association International pour l’Etude des Argiles” (AIPEA) and the “Clay Mineral Society” (CMS) [12]. They define clay as “naturally occurring material composed primarily of fine-grained minerals, which is generally plastic at appropriate water contents and will harden when dried or fired”. This definition is mainly based on the technical properties that make clays very suitable raw materials for the production of ceramics. In the field of soil science, the term clay is applied to classify the size fraction smaller than 2 μm [13] or the fraction between 1 and 4 μm according to the Wentworth scale [14].

Clays are usually composed of clay minerals and non-clay minerals. The latter are either non-weathered residual minerals, such as quartz, micas or feldspars, newly formed minerals like calcite, dolomite, siderite or pyrite, or weathering products which do not belong to the group of clay minerals, e.g. goethite and hematite. The term clay mineral is used for the hydrated phyllosilicates that give clays their characteristic properties that are specified in the definition of clay [12, 15].

The classification of clay types is manifold and can be applied based on the dominant clay minerals, the geological formation, the technical application or other properties [16]. Clays that are considered as potential SCM are usually divided into kaolinitic clays (low and high grade), common clays or illitic clays and bentonites or smectitic clays [17, 18].

2.1.2 Formation and occurrence of clay deposits

Clays make up the major part of sedimentary rocks [19], as they represent the products of the weathering process of rockforming silicates. This explains their geological abundance and world wide availability. The geological setting for the genesis of clay deposits can be diverse. The formation of clay deposits generally starts with the physical degradation and chemical dissolution of the primary minerals [20]. A principal distinction can be made in primary clay deposits, where the newly formed clay minerals stay at the position of formation, and secondary clay deposits, where the clays go through the processes of erosion, transportation and sedimentation. These processes can cause segregation of the various clay minerals as well as mixing with other minerals or uptake of alkalis [21]. The kind of clay mineral formed depends on the primary rocks, climatic conditions, pH and vegetation at the time of formation on the other hand. The climatic areas with the highest clay formation rates are the Taiga-podsol-zone and the Tropic forest zone [22]. In the latter, the weathering mantle can reach a thickness up to 120 m. The described formation processes result in a diverse and heterogenic distribution and composition of clay deposits over the globe, which was comprehensively visualized by Ito and Wagai [23] (Figure 1).

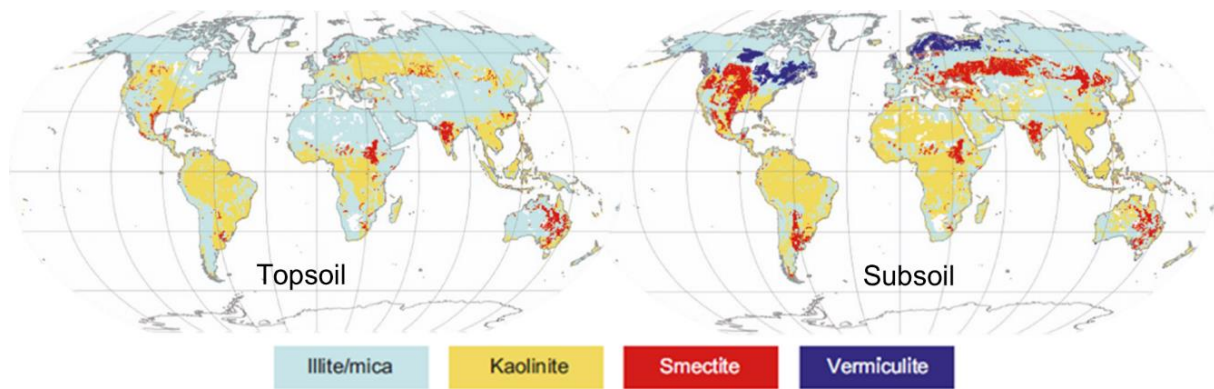


Figure 1 Global distribution of clay-sized mineral groups in the top- and subsoil (modified after Ito & Wagai [23])

In the case of Germany, the distribution of clay resources is provided by the map of mineral resources of Germany [24]. This map was combined with the geological map of Germany [25] and supplemented by active clay pits and cement plants in Figure 2 [26]. This presentation can help to identify possible resources for the production of calcined clay blended cements on the basis of existing clay pits or potential clay deposits.

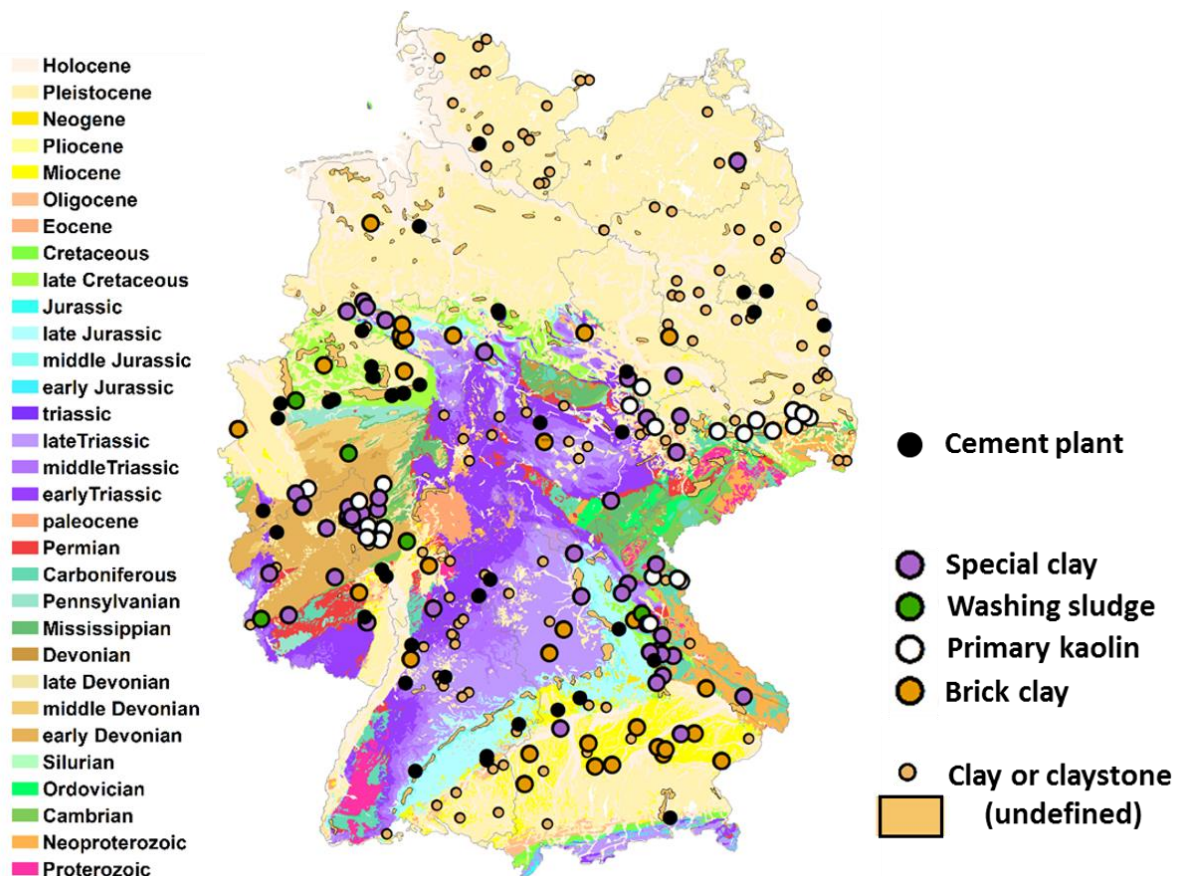


Figure 2 Geological map of Germany 1:1,000,000 with deposits of clay and claystone, active clay pits and cement plants (adapted from [26]).

2.1.3 Structural characterization of clay minerals

Clay minerals belong to the group of phyllosilicates. The basic structural unit of phyllosilicates is a continuous sheet of corner-linked tetrahedrons (Figure 3a). The center of the tetrahedron is usually occupied by Si^{4+} cations, which can be substituted by Al^{3+} or less frequently by Fe^{3+} [27]. These cations are coordinated by four oxygen atoms. The basal oxygen atoms connect the tetrahedrons while the apical ones are oriented towards an octahedral sheet and are shared with the octahedrally coordinated cation [28]. The center of the octahedron can be occupied by a range of cations, among which the most common are Al^{3+} , Fe^{3+} , Mg^{2+} , and Fe^{2+} [29]. The octahedral sheet is connected via shared edges (Figure 3b). Octahedrons can occur in cis- and trans-orientation, depending on the position of the hydroxyl (OH) groups. Different types of phyllosilicates can be distinguished concerning the arrangement of the single sheets. In the 1:1 layer type (one tetrahedral and one octahedral sheet: T-O), one side of the octahedral layer is connected to the apical oxygen atoms of the tetrahedral sheet, while the other side is occupied by OH groups. The 2:1 layer type (T-O-T) is characterized by a second sheet of tetrahedrons connected by their apical oxygen atoms with the other side of the octahedron.

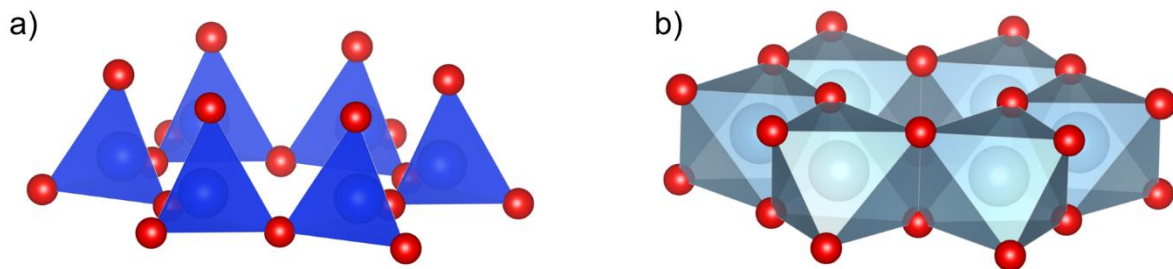


Figure 3 The basic structural components of clay minerals: a) a sheet of corner-linked tetrahedra, where the red spheres represent oxygen atoms and the sphere in the center of the tetrahedra show silicon atoms and b) the edge-sharing octahedral sheet with a six-fold coordinated cation (e.g. Al^{3+}) in the center of the octahedra. The figures were drawn using the VESTA software on the basis of the kaolinite structure model [30].

The layer types are further differentiated into groups, based on their layer charge, and into subgroups, based on the occupation of the octahedral position [28] (Table 1). Layers in clay minerals are either neutral or negatively charged. A negative layer charge is induced by vacancies or isomorphic substitutions in the tetrahedral (e.g. Al^{3+} for Si^{4+}) or octahedral sites [29]. The layer charge is a characteristic value for 2:1 clay minerals and responsible for important properties. In dioctahedral clay minerals the octahedral positions are occupied by trivalent cations (e.g. Al^{3+} or Fe^{3+}) so that a neutral layer charge requires the occupation of two out of three sites. Trioctahedral layers are characterized by divalent cations (e.g. Mg^{2+} or Fe^{2+}) which occupy three out of three positions [28].

The T-O or T-O-T layers form stacks in which the space between the single layers is referred to as interlayer. The interlayer distance is another characteristic attribute of clay minerals also termed as basal spacing. In the case of electric neutral layers, the interlayer space is usually empty. If the layer is negatively charged, an occupation of the interlayer by cations is required for charge compensation [18]. In swellable clay minerals these cations can reach variable hydration states that induce a change in the interlayer distance. In the case of chlorite group (2:1:1 clay minerals), the interlayer is occupied by an additional octahedral sheet.

Table 1 Classification of clay minerals, revised and shortened following [16] (ξ = layer charge)

Layer type	Group	Subgroup/ octahedral character	Species (examples)	Interlayer cation
1:1 T-O	Serpentine- kaolin ($\xi \approx 0$)	Serpentine (tr) Kaolin (di)	Chrysotile, antigorite Kaolinite, halloysite	
2:1 T-O-T	Talc- pyrophyllite ($\xi \approx 0$)	Talc (tr) Pyrophyllite (di)	Talc Pyrophyllite	
	Smectite ($\xi \approx 0.2-0.6$)	Smectite (tr) Smectite (di)	Saponite Montmorillonite	Na^+ , Ca^{2+} , Mg^{2+} , (K^+ , Al^{3+} , $\text{Fe}^{2+/3+}$, H_3O^+) hydrated
	Vermiculite ($\xi \approx 0.6-0.9$)	Vermiculite (tr, di)		Mg^{2+} , Ca^{2+} hydrated
	Interlayer deficient mica ($\xi \approx 0.6-0.85$)	Interlayer deficient mica (tr, di)	Illite, glauconite	K^+ , H_3O^+ (Na^+ , Ca^{2+}) non- hydrated
	Mica ($\xi \approx 0.9-1.0$)	Mica (tr, di)	Biotite Muscovite	K^+ (Na^+) ($>50\%$) non-hydrated

An arrangement of the layers in various sequences can generate different polytypes of one clay mineral. In many naturally occurring clay minerals, the crystal structure can furthermore possess a certain degree of disorder due to stacking faults or in the form of turbostratic disorder. Furthermore, structurally similar minerals, e.g. illite and smectite, can occur as mixed-layer clay minerals, resulting from interstratification of their layers in more or less ordered sequences [31].

2.1.4 Thermal treatment of clay minerals

During heating of clay minerals, three main reaction processes can take place: dehydration up to 300 °C, dehydroxylation between 400 and 900 °C, and formation of new crystalline phases at temperatures of 800 °C and higher [17]. While especially the second process is desired in order to receive reactive phases, the latter should be avoided, as the formation of crystalline or glass phases usually goes along with loss of reactivity [32, 33], as illustrated in Figure 4. An overview of reactions that can take place during heating of a common clay is given in Table 2. Concerning the optimum activation temperature, one has to differentiate between the different clay minerals. The following equations describe the dehydroxylation reactions in kaolinite, as an example for a 1:1 clay mineral (1), and illite, as an example of a 2:1 clay mineral (2):

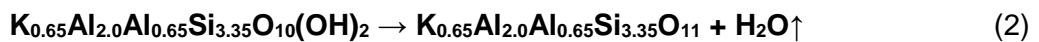
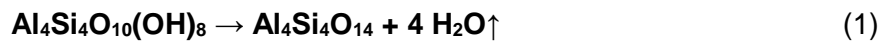
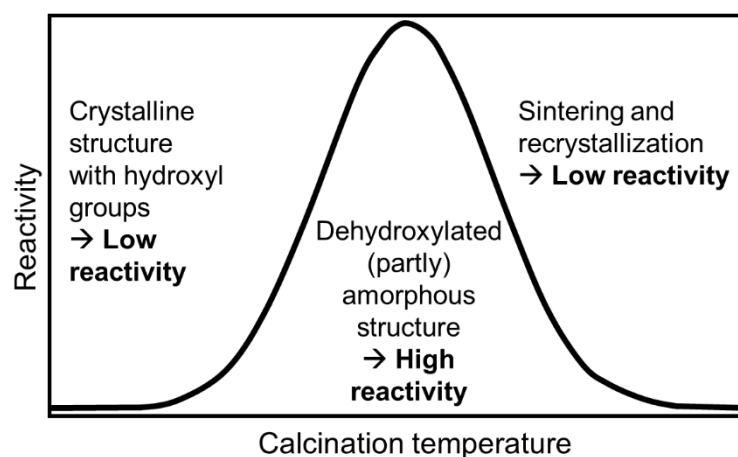


Table 2 Typical reactions taking place during the thermal treatment of common clays and their respective temperature range [34]

Temperature	Enthalpy	Reaction
80 – 225 °C	Endothermal	Evaporation of free water and dehydration of clay minerals
220 – 450 °C	Exothermal	Combustion of highly volatile organics
225 – 450 °C	Endothermal	Decomposition of hydroxides
380 – 420 °C	Exothermal	Decomposition of pyrite
450 – 700 °C	Exothermal	Combustion of low-volatile organics
400 – 850 °C	Endothermal	Dehydroxylation of clay minerals
650 – 850 °C	Endothermal	Decomposition of carbonates
> 850 °C	Exothermal	Formation of new crystalline phases

The gain of pozzolanic reactivity through calcination results from a change of coordination of Al and Si due to the loss of OH groups. This can be followed by ^{27}Al NMR before and after calcination. In kaolinite, the coordination changes from $\text{Al}^{[6]}$ to $\text{Al}^{[5]}$ and $\text{Al}^{[4]}$ as a consequence of the release of OH-groups that were initially bound to the Al [35]. In the FTIR spectra, this is indicated by a disappearance of the OH stretching bands and Al-OH bands [36]. Dietel et al. [37] observed for a common clay containing about 50 wt% 2:1 clay minerals and 12 wt% kaolinite a continuous shift from $\text{Al}^{[6]}$ via $\text{Al}^{[5]}$ to $\text{Al}^{[4]}$. While $\text{Al}^{[5]}$ reached a maximum at 650 °C, it decreased with elevating temperature and disappeared at 925 °C. This went along with a renewed increase of $\text{Al}^{[4]}$, due to formation of crystalline phases. The Al in five-folded coordination reveals a preferential dissolution under alkaline conditions, which can explain the high reactivity of metakaolin [32]. The silicon environments change from Q^3 sites in the intact silicate sheets to a range of different environments from Q^1 - Q^4 that is typical for a strongly disordered material [38]. This is also apparent from the change of FTIR spectra after dehydroxylation, where characteristic sharp Si-O adsorption bands merge to a broad single band representing amorphous SiO_2 [36]. In the case of kaolinite, the dehydroxylation induces the loss of long range order, which can be revealed by disappearance of the characteristic bragg reflections and the occurrence of an amorphous hump in the diffractograms.

**Figure 4** Simplified illustration of the course of the calcined clay's pozzolanic reactivity as a function of calcination temperature (Modified after [39]).

That is why metakaolin is considered as an amorphous material, while it is important to state that it differs fundamentally from glassy amorphous materials such as fly ash. At temperatures above 900 °C, the crystallization of a cubic spinel-type phase sets in, which subsequently reacts to mullite. The recrystallization process marks a significant decrease in the material's pozzolanic reactivity. The dehydroxylation peak temperature of kaolinite depends on the degree of disorder in the kaolinite structure and can vary between 500 and 600 °C. Disordered kaolinite favors the diffusion of hydroxyls due to a mismatch between the layers, which leads to an accelerated dehydroxylation [40]. In 2:1 clay minerals, the loss of OH groups is a more diverse process. Swellable 2:1 clay minerals (e.g. smectites or illite-smectite mixed layer minerals) lose their interlayer water usually below 200 °C. Even though this process has an influence on the crystal structure by reducing the interlayer distance in (00l)-direction, it must be differentiated from the dehydroxylation process, which induces change of coordination of Si and Al sites. The dehydroxylation of 2:1 clay minerals can vary in a wide temperature range [41] and depends on the interlayer cation, the octahedral cations as well as trans- and cis-vacancies in the octahedral sheet [42].

2.1.5 Properties of (calcined) clay particles in suspensions

The properties of clay suspensions are profoundly studied, as they are the basis for a variety of ceramic forming processes [43, p. 568 ff.]. However, lack of data exists concerning the behavior of dehydroxylated clay minerals in aqueous suspensions. When applied as SCMs, the surface properties of calcined clays are of great significance regarding the interaction with the cementitious pore solution. This is why the knowledge about the reactions at the interface between solid surfaces and the liquid phase in raw clay suspensions shall be reviewed here in order to discuss possible mechanisms in calcined clay systems.

When oxides are dispersed in water, they usually reveal a pH-dependent, variable electric surface charge due to unsaturated bonds at the particle surface [43, p. 568 f.]. In clay minerals, isomorphous substitutions in the tetrahedral and octahedral sheet additionally induce a permanent surface charge in the siloxane surface. This surface is present on both basal planes of 2:1 clay minerals and on the tetrahedral side of 1:1 clay minerals (silica facet) [44]. The gibbsite facet, which is the hydroxide surface of the octahedral sheet in 1:1 clay minerals, possesses a negative surface charge at a pH above 7 [45]. Clay minerals therefore reveal a permanent charge on the basal planes and a variable charge on the edges.

In aqueous suspensions, charged particles are surrounded by dissolved ions. The charged particle surface attracts ions with contrary charge that form a rigidly attached layer, the so-called Stern-layer [43, p. 572]. This layer is in turn surrounded by the diffuse layer, which is built up by co- and counter-ions, where the concentration of the latter decreases with the distance from the charged surface [46]. When a suspended particle is in motion, a shear plane evolves between the Stern layer and the diffuse layer. The charge potential between the shear plane and the diffuse layer can be measured directly and is specified as zeta potential (ζ), which is often used as approximation for the charge potential of the particle surface [46]. The zeta potential of clay minerals is known to be strongly negative under alkaline conditions, while the presence of Ca^{2+} induces a rapid charge reversal due to adsorption onto the surfaces of the clay particles. This charge reversal was also measured in synthetic pore solution [47]. The shift of an initially strongly negative zeta potential at a pH above 12 to less negative or positive values as a result of Ca-adsorption was also proved for calcined clays [48-50]. Since several

studies emphasized the role of ion adsorption during Portland cement hydration [51-53], the described behavior of calcined clays needs to be addressed, when discussing their impact on cement hydration.

2.1.6 Particle characteristics of clay minerals

A clay mineral particle is generally formed by an assemblage of several layers. In the case of kaolinite, stacks between 70 and 200 layers are assumed to build up an average particle, based on the typical crystal thickness and the thickness of an individual layer [54]. Bergaya and Lagaly [16] recommended to use the term particle for an assembly of layers and the term aggregate for an assembly of particles. The particles and aggregates in clays can arrange in various ways, leading to different types of available spaces (Figure 5). The specific surface area (SSA) as determined by the BET method therefore represents to a large part internal surfaces. These internal surfaces can appear in the form of interparticle and interaggregate space, while the interlayer space is usually not accessible for N_2 molecules [55]. This is one reason, why there is no clear correlation between SSA and particle size distribution, since it is difficult to dissolve all pores and interparticle spaces before and during measurement. Apart from that, assessment of particle size of clays is a challenge itself, since the assumption of spherical particles, on which most established methods (laser diffraction, sedimentation) are built up, does not apply for clay particles and therefore calculated equivalent diameters differ significantly from the true particle dimensions [56]. There are furthermore methodical differences, so that clay minerals are interpreted larger by laser diffraction compared to methods based on sedimentation [57].

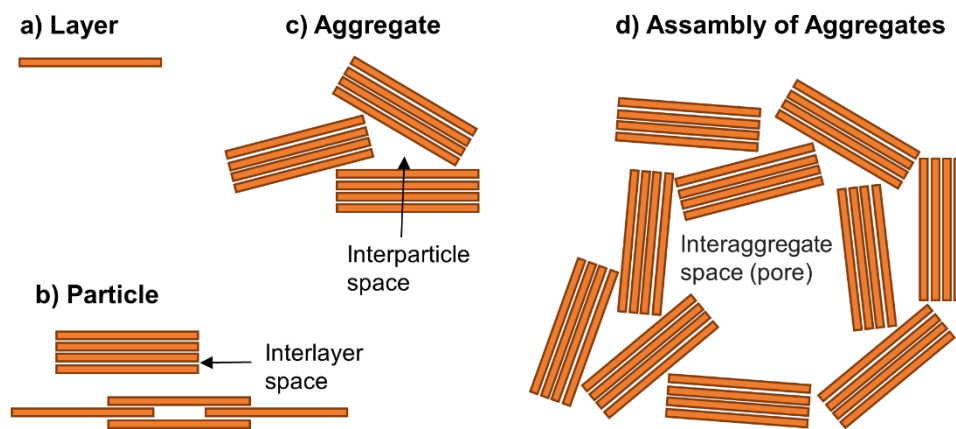


Figure 5 Simplified illustration of the arrangement of clay layers (a) to form particles (b), aggregates (c) and assemblies of aggregates (d), leading to different kinds of pores in clays (redrawn after [16]).

Typical values for the SSA of common clay minerals are 10 – 20 m²/g for kaolinite, 50 – 100 m²/g for illite and 10 – 800 m²/g for montmorillonite [58]. The surface area decreases significantly during thermal treatment of 2:1 clay minerals while it is nearly unaffected for kaolinite up to the recrystallization temperature.

2.1.7 Mineralogical characterization of clays by X-ray powder diffraction

A comprehensive overview of the methods for characterization of clay resources is given by RILEM Technical Committee 282-CCL [59]. The most important and widespread method applied for the mineralogical analysis of clays is X-ray powder diffraction. This method is mandatory when aiming at quantitative phase analyses of clays, but may well be supplemented

by further methods. Clays belong to the most challenging materials to be studied by XRD, due to their complex structures that often possess a certain degree of disorder. However, significant progress has been made during the past decades [60]. A special sample preparation, which includes size fractioning and preparation of texture specimen of the smaller 2 μm fraction that are measured in air dried condition and after ethylene glycole treatment, is compulsory for a correct mineral identification. Quantification can be carried out on powder diffractograms from the bulk samples. Rietveld refinement is the most common method, while it includes some difficulties associated with clay minerals' nature. The first one is the preferred orientation of clay minerals along the (00l) lattice plane that causes increased intensities of the (00l) reflections. This can be reduced by special sample preparation techniques as side loading, or even more sophisticated, spray drying [61]. Furthermore, a correction during Rietveld refinement is possible through the March-Dollase model [62] or by algorithms using spherical harmonics functions [63]. There have been different approaches for modelling strongly disordered structures with the goal of their quantification. One quite successful approach is the full-pattern summation of X-ray powder diffraction data [64]. In this approach, pure mineral standards are measured and their diffractograms are fitted to the diffractograms of the investigated sample. This method, however, requires a large amount of pure mineral standards as well as an elimination of preferred orientation as far as possible. The second approach, Rietveld refinement, does not require the collection of a database of pure reference materials, but is able to calculate the diffractogram based on structural and instrumental parameters [65, 66]. Its drawback is however that common structural models are unable to implement defects or interstratification. Nevertheless, progress has been made in modelling these kinds of disturbed crystalline structures [67-70] and implementation in common program codes, e.g. Profex-BGMN [71, 72] or TOPAS [73] enables their quantification. Furthermore, also the PONKCS approach [74] can be applied successfully for modelling strongly disordered phases during Rietveld refinement, as has already been shown by Taylor and Matulis [75], long before the method became popular for quantifying amorphous phases. Lorentz et al. [76] revealed that the stacking faults in kaolinite can be adequately modeled by using a combination of kaolinite, nacrite and dickite structures. Apart from quantitative analysis, XRD is also capable of defining the degree of disorder in kaolinite based on different established indexes, e.g. Hinckley index [77] or Aparicio-Galán-Ferrell index (AGFI) [78].

2.2 Portland cement hydration

2.2.1 Cement hydration in general

During the past decade, enormous progress in experimental methods and evaluation routines on the one hand and thermodynamic modelling on the other have improved the understanding of Portland cement hydration enormously. As soon as the complex multiphase mixture Portland cement gets in contact with water, different chemical and physical processes start to run off in parallel. These processes involve dissolution, diffusion, nucleation, growth, complexation and adsorption [79]. Based on the heat development (Figure 6), the early hydration of Portland cement can be divided into different phases. Immediately after mixing, a short and intense heat flow peak appears. During this period, an initial dissolution of the clinker phases - specifically C_3S and C_3A - and sulfates takes place together with a coincident precipitation of ettringite [79, 80]. A rapid slowdown of reaction initiates the so-called "induction period", which however can be rather recognized as a short minimum in the heat flow curve. The mechanisms behind this slowdown of hydration have been heavily debated among the cement research community during the past decades [81]. The two most popular theories can

be referred to as the “protective layer (membrane) theory” and the “geochemical (dissolution controlled) theory” [82, 83]. The “protective layer theory” describes the formation of an early hydration product on the surface of the C_3S grains, inhibiting their further dissolution, comparable to the formerly assumed AFt or AFm layer on the surface of C_3A . However, meanwhile most evidence supports the “geochemical theory”, which claims that the induction period is a consequence of the slowed down C_3S dissolution due to a lower degree of undersaturation as the system approaches equilibrium [82-85]. C-S-H starts to precipitate as X-ray amorphous, colloidal material [86]. With a temporal offset in relation to the onset of accelerating period, the short-range ordered C-S-H converts to a long-range ordered C-S-H, which is detectable by XRD, as described by Bergold et al. [87]. This precipitation coincides with a significant drop in Ca concentration in the pore solution, which was assigned to a newly emerging equilibrium corresponding to the solubility product of C-S-H [51]. The strong heat development during the main period is associated with a rapid dissolution of C_3S and precipitation of C-S-H.

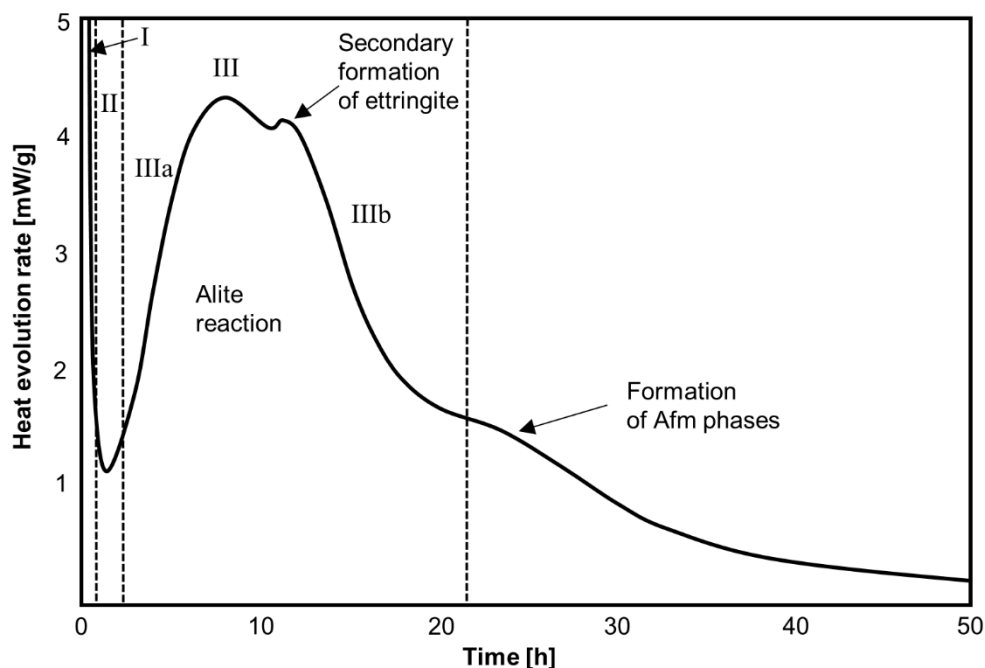


Figure 6 Exemplary heat flow curve during the early hydration of an ordinary Portland cement including the shoulder peak corresponding to secondary ettringite precipitation and the subsequent broad peak representing AFm phase formation (redrawn after [79] and [88]. I: initial period, II: dormant or induction period, III: main period, IIIa: accelerating period, IIIb: decelerating period.

In a properly sulfated Portland cement, a second heat flow peak appears during decelerating period. This peak, which is often rather recognized as a shoulder of the alite peak, corresponds to the depletion of the solid sulfate carrier [89], which triggers an accelerated ettringite formation. A third, usually broader peak is associated with the formation of AFm at the expense of C_3A and ettringite or carbonate, if present. The occurrence of deceleration period is often connected to a change from dissolution- to diffusion-controlled hydration, however, there are more possible mechanisms to consider, such as consumption of small particles, lack of water and space and change in the growth mechanism of C-S-H [79].

2.2.2 Aluminate reaction

The hydration of tricalcium aluminate (C_3A) in Portland cement is referred to as aluminate reaction. C_3A occurs in cement clinker in the form of two different polymorphs: cubic and

orthorhombic C_3A . The crystal structure depends on the amount of sodium available in the raw material [90]. Pure C_3A crystallizes in the cubic structure. At a substitution level of 2.4 – 3.7 wt% of Ca^{2+} by Na^+ , cubic and orthorhombic C_3A usually co-exist [91]. This is mostly the case in common cement clinker. The two polymorphs differ significantly with respect to their dissolution behavior and hydration kinetics [92, 93]. The reaction of C_3A with water results in a strong exothermic dissolution, immediately followed by a formation of calcium aluminate hydrate (CAH) phases, which initially precipitate as C_4AH_{19} and C_2AH_8 , or most likely solid solutions or intercalated mixtures of both [79]. Since these phases are thermodynamically unstable, they further react to form hydrogarnet (C_3AH_6) [94]. As the precipitation of the mentioned phases proceeds rapidly and forms large crystals, it would induce flash set of the cement paste. Hence, calcium sulfate is added as setting regulator. The retarding effect of calcium sulfate on the C_3A hydration has often been attributed to an ettringite layer that forms a diffusion barrier [95]. This mechanism was meanwhile refuted by several authors due to two observations: first, the network of ettringite crystals is too porous to act as a physical barrier against ions [81, 96] and second, the renewed C_3A hydration starts before ettringite is consumed to form AFm phases [79]. Geng et al. [96] ruled out any diffusion barrier to control the rate of C_3A dissolution. Even though, they provided evidence for a rapidly formed layer of amorphous AFm phases on the C_3A surface, they could prove that these phases do not act as a diffusion-barrier. Despite the mechanisms are still matter of debate, evidence was gathered during recent years supporting the theory of an adsorbed ionic species, resulting from the dissolution of calcium sulfate, that hinders the further dissolution of C_3A [52, 97]. Myers et al. [93] described the formation of an Al-rich leached layer as a consequence of incongruent dissolution at the C_3A /solution interface and identified the adsorption of Ca-S ion pair complexes onto this layer as the key inhibitor of C_3A dissolution in presence of $CaSO_4$ [52]. In this context, it is important to mention that a retardation by sulfate ions alone does not take place. Liu et al. [98] found, that Na_2SO_4 only slightly retards C_3A hydration, while $CaSO_4$ ($C\bar{S}$) shows a significantly stronger effect and the strongest retardation is induced by $MgSO_4$. As long as $C\bar{S}$ is available for dissolution, the phase resulting from C_3A hydration at ambient conditions is ettringite ($C_6A\bar{S}_3H_{32}$). The precipitation of ettringite takes place at different rates. A fast initial precipitation is observed shortly after the mixing with water. The precipitation rate subsequently slows down until the solid sulfate carrier is depleted. Jansen et al. [51] could show, that the amount of initially dissolved C_3A is sufficient for the ettringite precipitation until this point. Eventually, sulfate gets desorbed from the C_3A surface and ettringite precipitation rate increases again. After all sulfate is bound by ettringite, monosulfate ($C_4A\bar{S}H_{12}$) precipitates at the expense of ettringite and the remaining C_3A . If carbonate ions are present in the pore solution, which is the case for cements containing limestone, ettringite is stabilized and carboaluminates form instead of monosulfate [99].

2.3 Supplementary cementitious materials (SCMs)

2.3.1 Classification of SCMs

SCMs are commonly differentiated into inert, pozzolanic and latent hydraulic materials [100]. This classification however is not always clear, as materials generally classified as inert can influence cement hydration to different extends and the pozzolanic reaction can differ significantly between various materials with regard to reaction kinetic and hydrate phase formation [33]. One can generally distinguish between two principal reaction mechanisms of SCMs in blended cement: physical effects, which occur for all kinds of materials and are usually comprised under the term “filler effect” and a chemical contribution through the release of ions, which contribute to the formation of hydrate phases.

2.3.2 Reactivity tests for SCMs

A wide range of testing procedures has been developed during the past decades, with the objective of a fast and reliable assessment of the reactivity of SCMs. According to Snellings and Scrivener [101], the reactivity of an SCM can be determined based on the following parameters: consumption of portlandite, reaction degree of the SCM, amount of bound water and heat release or volume change during the reaction. The most popular tests using the parameter of portlandite consumption are (modified) Chapelle and Frattini test, of which the latter is the basis for the current standard DIN EN 196-5 [102]. The drawback of DIN EN 196-5 is, however, that it is not recommended as a quantitative assessment of pozzolanity but only differentiates between pozzolanic or non-pozzolanic behavior. From this it is also apparent that the method is not designed for latent hydraulic materials. A round robin organized by RILEM TC 267-TRM including 11 different SCMs revealed insufficient correlation with 28 days strength activity index and poor interlaboratory reproducibility of the current standardized methods [103]. In combination with an increasing use of SCMs, which tend to become more complex and diverse, raised the need for rapid screening tests, which have the ability to quantitatively assess and compare the reactivity of SCMs with different reaction mechanisms. The R^3 test, developed by Avet et al. [104], provides the greatest potential in this context, as it shows a good correlation to 28 days strength and requires a short preparation time together with a moderate duration of the testing procedure (3 – 7 days) [105]. The method uses a model system consisting of portlandite and an alkali-sulfate (KOH, K_2SO_4) solution. This provides enough CH for the pozzolanic reaction and a high enough alkalinity to ensure hydration of latent hydraulic materials. Additionally, calcite is added, in order to provide carbonate ions, which, in combination with sulfate, ensure an efficient reaction of the aluminum provided by the SCM. In order to accelerate the reactions, the test is performed at 40 °C. The reactivity can be assessed either by determination of the bound water or by isothermal calorimetry. Even though, this test retrieves even after one day quite good correlations with relative strength for kaolinitic clays, it has been shown that slower SCMs require at least 3, better 7 days. Suraneni and Weiss [106] proposed a modified R^3 test that excludes K_2SO_4 and calcite, raises the temperature to 50 °C and the test duration to 10 days and determines the CH consumption in addition to the heat release. This allows a differentiation of the SCMs based on their reaction mechanisms. A more direct way of determining the reactivity is to measure the solubility of ions, that take part in strength contributing reactions. The measurement of reactive SiO_2 as a standardized parameter in DIN EN 197-1 [107] has been proven to be unreliable, especially regarding the assessment of calcined clays [105, 108]. This can be drawn back, inter alia, to the neglect of reactive aluminum. Buchwald et al. [109] therefore established a testing procedure for metakaolin, where 1 g of material is eluted for 20 h in 10 % NaOH solution and the dissolved Al and Si is measured via ICP-OES. This method was shown to correlate well with the strength activity index for a clay calcined at different temperatures [6].

2.3.3 Physical reaction mechanisms

The mechanisms behind the filler effect have been studied by several working groups and are summarized in Figure 7 following the descriptions of Zhang et al. [110]. Besides the hereafter-explained enhancing effects on the clinker hydration, the replacement of clinker with an inert SCM reduces the reactivity (e.g. represented by the heat flow) normalized on the whole system, simply due to the replacement of reactive clinker with less reactive materials [111]. The enhancing effects on the clinker hydration become visible by normalizing the heat flow on the clinker content.

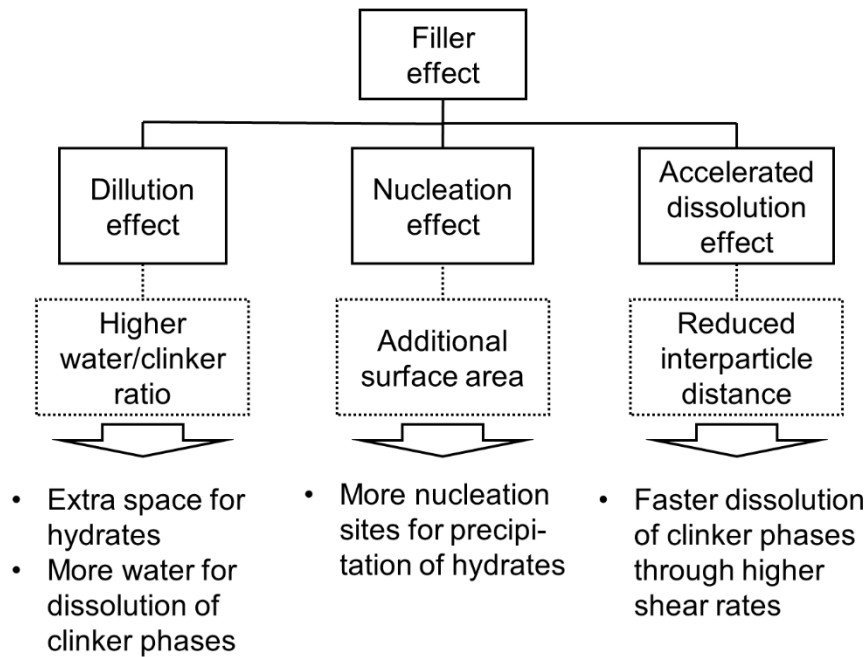


Figure 7 Mechanisms explaining the filler effect of SCMs in blended cement (drawn according to descriptions in [110, 112-114]).

Part of the influence of inert fillers on the clinker hydration can be traced back to the increased water to clinker ratio [112]. When cement clinker is partly replaced by an inert SCM and the water to binder ratio remains unchanged, there is more water available for dissolution of clinker phases and more space for hydrates to precipitate. Furthermore, depending on its fineness and available surface area, the SCM provides additional nucleation sites for the crystallization of hydrate phases [113]. Several studies have shown that this effect is strongly controlled by the type of surface. Limestone, for instance, acts as a more efficient nucleation site compared to other fillers [113, 115, 116]. A further effect induced by the addition of fine fillers was revealed by Berodier and Scrivener [114], who could identify a higher shear rate induced by the reduction of interparticle distance as the mechanism accelerating the dissolution of clinker phases. Kumar et al. [116] pointed up a correlation between SSA and replacement level of the SCM with the heat flow rate during C_3S hydration.

2.3.4 Chemical reaction mechanisms

Lothenbach et al. [112] named physical effects as the dominating ones during the first day of hydration, since the chemical reactivity highly depends on the alkalinity of the pore solutions, which only builds up slowly. However, highly reactive SCM, such as metakaolin or blast furnace slag (BFS) can reveal significant reaction degrees within one day, as shown in Figure 8 [33] or by Naber et al. [117] for metakaolin or microsilica. The chemical reactivity of established SCMs usually originates from amorphous phases, largely composed of SiO_4 and AlO_4 tetrahedrons, which partly dissolve under alkaline conditions [33]. If portlandite is consumed during SCM hydration, one speaks of a pozzolanic reaction, while hydraulic and latent hydraulic materials hydrate on their own or, in case of the latter, after alkaline or sulfate activation [91, p. 261 ff]. The beneficial effect of chemical reactive SMCs results from the formation of additional hydrate phases that fill up pore space and hence create a denser microstructure [112]. Furthermore, the C-S-H composition is altered in presence of SCM, usually revealing a lower Ca/Si ratio and incorporating Al. The pore solution in blended cementitious systems possesses a lower pH compared to pure OPC systems.

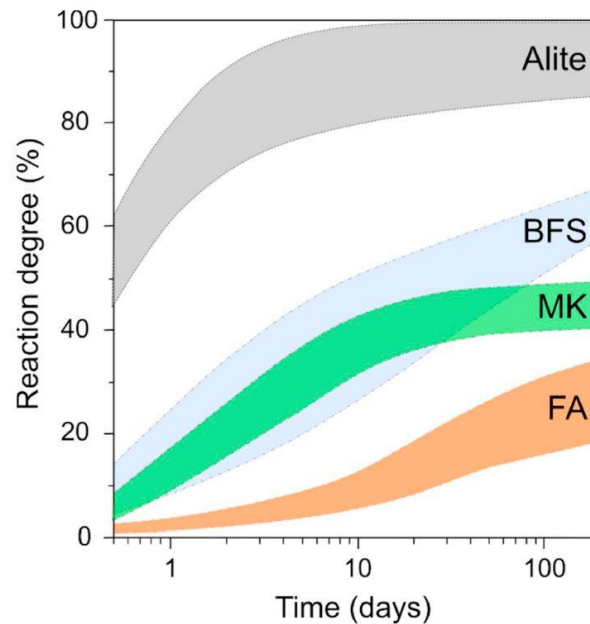


Figure 8 Reaction degree of different SCM in comparison to alite provided by Skibsted and Snellings [33].

2.3.5 Impact of calcined clays on early hydration

Calcined clay is a collective term for a considerably heterogeneous group of materials, facing the fact, that the composition and properties of clays vary widely (see chapter 2.1). Calcined clays used as SCM retrieve their pozzolanic properties from (partly) dehydroxylated clay minerals. The reactivity therefore depends to the most part on type and amount of clay minerals as well as material temperature and dwell time during calcination. The typical LC³ formulations usually incorporate calcined kaolinitic clays with a metakaolin content of at least 40 wt% [7]. Beuntner and Thienel [118] found significant differences in the reaction mechanisms of a calcined common clay and MK during early hydration. While MK strongly accelerates the silicate and aluminate reaction, the former tends to be delayed and the latter is slightly promoted in the presence of calcined common clay. The impact of calcined clays on the silicate reaction can be well explained by the physical mechanisms referred to in 2.3.3. However, their impact on the aluminate reaction has led to some controversy in the literature. In the pioneering work of Antoni et al. [10], the discussion was opened, whether the acceleration is driven solely by the additional surface area or if aluminates originating from MK already play a role at this stage. Either way, the authors emphasized the need for additional gypsum addition to ensure a proper hydration of C₃S. Several subsequent studies referred to the aluminum released by MK as the trigger for an accelerated and enhanced aluminate heat flow peak [90, 119, 120]. While this seems logical at first, evidence proving this mechanism in blended cement has never been brought up. Zunino and Scrivener [121] compared a nearly pure metakaolin with a moderate SSA with a calcined clay with 50 wt% MK and high SSA. As the latter provoked a much stronger acceleration of the aluminate peak, they emphasized the SSA as the dominant factor. This was supported by observations made with limestone blended systems, that were adjusted to the MK blended ones, showing a similar acceleration. The faster sulfate depletion in blended cements was therefore related to the faster C-S-H precipitation induced by the filler effect and the adsorption of sulfate onto the C-S-H. The uptake of sulfate into C-S-H has been proven in previous studies [122, 123]. However, recent investigations in clinker free systems with different calcined phyllosilicates revealed a pronounced aluminate heat flow peak together

with an enhanced ettringite formation [124]. Even though this may not be transferred directly to cementitious systems, it still proves that metakaolin is capable of forming ettringite in presence of calcium sulfate and absence of C_3A at an early stage of hydration.

2.3.6 Impact of calcined clays on phase assemblage

In addition to the classical pozzolanic reaction, where SCM consume CH to form C-S-H, calcined clays supply a significant amount of aluminum that is to a certain extent incorporated into C-A-S-H, but to a large part available for the precipitation of AFm phases and AFt. This results in the formation of additional ettringite when sufficient sulfate is available. When sulfate is depleted and carbonate ions are present in the pore solution, the aluminum is further consumed by carboaluminates. Only at a AS_2/CH ratio of above 1, strätlingite becomes thermodynamically stable [11]. The stabilization of ettringite by carbonate ions is the prerequisite for the synergetic effect of limestone and calcined clay in LC^3 cement. While in limestone free cements monosulfate is formed at the expense of ettringite after sulfate depletion, the latter is stabilized in presence of carbonates and carboaluminates form instead [99]. This increases the total volume of hydrate phases. In binary Portland limestone cements, this reaction can take place only until the aluminates from the clinker are depleted. In ternary LC^3 cements, the supply of aluminum ions is maintained by the MK or other calcined clay minerals. This leads to an increased amount of hemi- and monocarboaluminate which in turn reduces porosity and permeability and enhances strength [7]. During isothermal calorimetry, this reaction is visible as a third heat flow peak after the silicate and aluminate peak [125].

3 Summary of the methods applied

X-ray diffraction (XRD)

All XRD measurements were carried out in Bragg Brentano geometry in a PANalytical Empyrean diffractometer, operated with CuK α radiation ($\lambda = 1.5406 \text{ \AA}$) at 40 kV and 40 mA. The instrument is equipped with a PIXcel1D linear detector and a primary Bragg-Brentano^{HD} monochromator. A secondary Ni-filter was applied instead during measurements of texture specimen, where a variable divergence slit was used. XRD served as main method to characterize the raw clays. Texture specimen were prepared using the $< 2 \mu\text{m}$ fraction. Therefore, the sample was desagglomerated using ultrasonic treatment and a small amount of sodium pyrophosphate as dispersing agent. The suspension was filled in a beaker and left for the appropriate settling time according to Stokes law. Texture specimen were prepared following the glass slide method and measured in air dried and glycolated condition. A detailed description of the sample preparation can be found in [59] and [126]. Powder specimen of the bulk samples were prepared in a side loading tool in order to reduce preferred orientation. In situ XRD was carried out on cement pastes that were prepared in special sample holders, placed on a temperature control device and covered by a Kapton film. Four scans per hour were taken in a range between 6° to $40^\circ 2\theta$. The pattern of the Kapton film was fitted according to [127]. Quantitative phase analysis was carried out using Rietveld refinement [128] extended by the external standard approach [129, 130] using the software Profex-BGMN [71, 72]. Diffractograms with identical phase assemblage were handled in batch refinements. Lattice parameters and crystallite sizes of the starting materials were obtained from measurements of the dry powders and usually kept fixed during refinement of the pastes but refined for the precipitating hydrate phases. Recrystallized Zircon functioned as external standard and the mass attenuation coefficient (MAC) of each sample was calculated from the MACs of the single elements and their weight fractions obtained by chemical analysis.

Thermal analysis (TGA)

Thermal analysis was applied in order to analyze the dehydroxylation reaction of the investigated raw clays. Measurements were conducted in a Netzsch STA 449 F3 Jupiter. An amount of approx. 200 mg of the ground sample was filled into Al₂O₃ crucibles and measured from room temperature to 1000 °C at a heating rate of 10 K/min. Data was processed in Origin 2018b. The mass losses due to dehydration, dehydroxylation and decarbonation were determined using the tangent method [131].

Attenuated total reflection Fourier transform infrared spectroscopy (ATR-FTIR)

Infrared spectroscopy supplemented the qualitative raw clay analysis before calcination, and allowed an evaluation of the dehydroxylation process based on the disappearance of the OH bands after calcination. FTIR spectra were collected using a Nicolet iS10 FTIR spectrometer (ThermoFisher Scientific) in ATR mode. The spectrometer was equipped with a mid-infrared KBr beamsplitter, an EverGlo TM MIR radiation source ($\bar{\nu} = 15,798\text{cm}^{-1}$), a diamond ATR crystal and a dTGS detector.

Isothermal calorimetry

A TAM Air isothermal calorimeter (TA instruments) was used for heat flow measurements of hydrating pastes at 25 °C and for the R³ reactivity test [132] at 40 °C. External sample preparation was carried out by stirring the pastes manually with a spatula for 60 seconds. The ampules were transferred into the calorimeter chamber within 2 minutes after water addition. Data evaluation was carried out in Origin 2018b/2019b. The cumulative heat was derived by

integration of the heat flow curve and converting the unit to J/g by multiplying the received values with the factor 3.6.

Inductively coupled plasma – optical emission spectroscopy (ICP-OES)

ICP-OES was employed on lithium metaborate flux fusions in order to determine the chemical composition or on eluates gained by elution of calcined clays in 10% NaOH solution. The latter were prepared by eluting one gram of sample in 400 ml solution for 20 h on an interval agitator, filtering the suspensions and acidifying the eluate to pH 1. The solutions were measured in a Varian 720 ES spectrometer (Agilent Technologies, Santa Clara, CA, USA) according to [133].

Scanning electron microscopy (SEM)

SEM analysis was performed with a Zeiss EVO[®] LS 15 microscope operated at an acceleration voltage of 20 kV and a working distance between 7.5 and 9 mm. Samples were sprinkled either on two-component adhesive or adhesive carbon tabs and coated with gold.

Zeta potential

The zeta potential of calcined clays was investigated with a DT-310 spectrometer (Dispersion Technology Instruments) using the electroacoustic method [134]. Depending on the experimental setup, samples were either dispersed manually at a solid content of 50 wt% and measured under static conditions, or dispersed by a magnetic stirrer in suspensions with a solid content of 25 wt% and measured during agitation. Titration experiments were performed using an automatic titration unit, while the pH was kept constant through dropwise addition of 1M KOH solution.

Thermodynamic modelling

Gibbs Energy Minimization Software for Geochemical Modeling (GEMS) [135] was applied in combination with the Cemdata18 database [136] in order to calculate phase assemblage in the C₃A model systems at thermodynamic equilibrium.

Calculation of reaction enthalpies

The theoretical heat evolution based on the amount of dissolved clinker phases and precipitated ettringite was calculated using the enthalpies for the underlying reactions following Jansen et al. [89].

4 Main results

The main scientific contributions of this thesis have been published in three peer-reviewed publications presented in chapter 8. The key outcomes of these contributions are summarized and put into context in the following part. Chapter 4.1 summarizes the new findings concerning the assessment of clays for the use as SCM and correlation of raw clay mineralogy with the reactivity after calcination. The parameters influencing the early cement hydration in presence of calcined clays are elucidated in Chapter 4.2, with special attention on the aluminate reaction. Chapter 4.3 illuminates the derived mechanisms that are brought up as reasons for the increased sulfate demand of calcined clay blended cements.

4.1 Mineralogical properties determining the reactivity of calcined clays

As described in chapter 2, it is of vast importance, to correlate raw material properties with reactivity after thermal activation in order to assess potential clay deposits for production of calcined clays. Apart from that, the methods evaluated in this chapter are important tools to characterize the raw and calcined clays used in the further course of the present work. Therefore 13 different raw clays were investigated concerning their mineralogical properties and reactivity after calcination. Special sample preparation was applied in order to reliably distinguish between the different contained clay minerals. Implementation of structure models considering turbostratical and stacking disorder allowed a reliable quantification of the raw clays. Supporting techniques such as thermal analysis and FTIR spectroscopy were applied to verify the results. The degree of kaolinite disorder in the kaolinite-rich clays was assessed using different methods based on XRD and FTIR.

4.1.1 Mineralogical characterization of the raw materials

Common clays usually represent complex multiphase-mixtures of clay- and none clay-minerals, often including disordered structures, as for instance irregular interstratifications. In order to determine the contribution of the individual clay minerals to the reactivity and their influence of reaction kinetics, an extensive and reliable mineralogical characterization was considered as an important prerequisite. The first step in doing so was to identify the clay minerals in oriented specimen of the separated $< 2 \mu\text{m}$ fraction. In order to verify swellable 2:1 clay minerals, the samples were measured in air-dried and ethylene glycol saturated condition. These measurements are exemplarily shown for a smectite-rich marl (MOSM) in Figure 9. The intercalation of ethylene glycol into the smectite interlayer induces a shift of the (001) reflection from $6.2^\circ 2\theta$ ($d_{001} = 14.3 \text{ \AA}$) to $5.2^\circ 2\theta$ ($d_{001} = 17.0 \text{ \AA}$). The respective diffractograms for further 2:1 clay mineral dominated clays are provided in chapter 8.1, Fig. 1. Qualitative phase analysis was furthermore supported by assessing the characteristic absorption bands of the FTIR spectra.

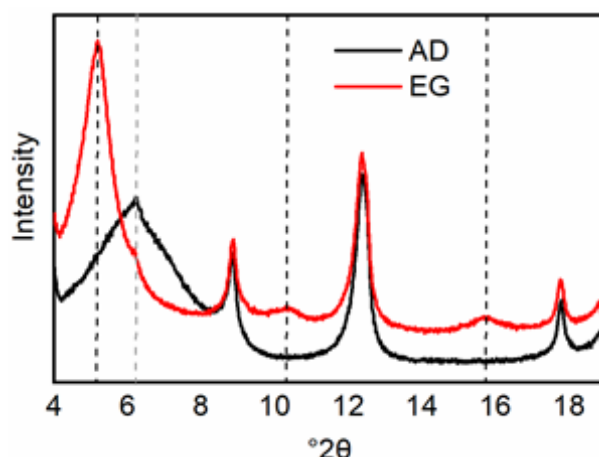


Figure 9 Diffractogram of a texture specimen of the < 2 μm fraction of a smectite-rich marl (MOSM) under air-dried (AD) and glycolated (EG) conditions.

For the correct quantification of kaolinite, occurrence of stacking disorder has to be identified. This parameter is known to affect dehydroxylation behavior as well as pozzolanic reactivity after calcination [38, 137, 138]. While different methods based on empirical indexes have been established, the one that is the least prone to disturbance by other phases is the AGFI [78]. This index equals the sum of the $(1\bar{1}0)$ (A) and the $(11\bar{1})$ (B) peak heights divided by two times the (020) peak height (C). The determination of the correct heights requires a peak deconvolution procedure that is provided in Figure 10 for one highly (“KK”), one moderately (“KBZ”) and one poorly ordered kaolinite (“FUP”). The excerpts from the diffractograms between 19 and 23 $^{\circ}2\theta$ (Figure 10) reveal that the $(1\bar{1}0)$ and $(11\bar{1})$ reflections are heavily disturbed by the stacking disorder and merge to one broad diffuse peak in the case of the strongly disordered sample. This has to be considered during Rietveld refinement, where the usage of ideal structure models leads to unsatisfactory results. The refinement of moderately disordered kaolinites yields the most adequately results when combining an ideal and a disordered structure model (Figure 11b). It is not distinguishable if this is associated with a physical phase mixture or segregation of different domains.

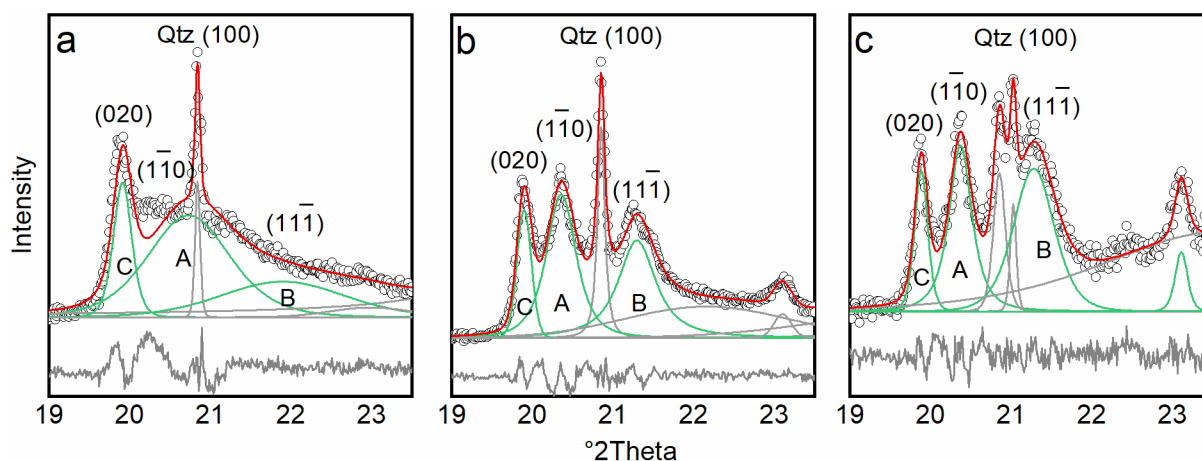


Figure 10 Peak deconvolution according to the proposed procedure by Aparicio et al [78] for a poorly (a, FUP), a moderately (b, KBZ) and a highly ordered kaolinite (c, KK) using the program Fityk [139]. The green line represents the fitted kaolinite peaks and the light grey line the fitted peaks of secondary phases and the background. The red line marks the sum of the curves and the dark grey line the difference between measured and fitted curve.

The correct quantification of illite-smectite interstratifications requires a different approach. The type of interstratification was identified by trying models with different degrees of long-range ordering according to Ufer et al. [68, 140] first in one-dimensional fits of the texture specimen and eventually by implementing them into the Rietveld refinement of the powder patterns. The refined pattern of a common clay containing illite-smectite interstratifications together with disordered kaolinite is illustrated in Figure 11a.

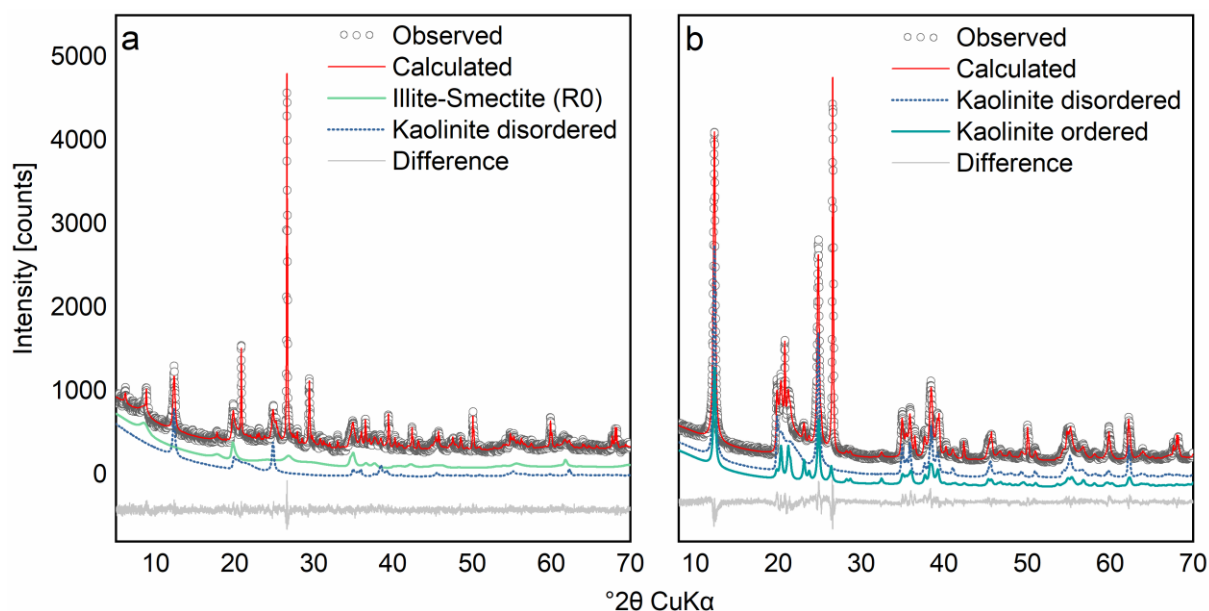


Figure 11 Rietveld refinement for a common clay containing illite-smectite interstratifications (a, “AC”) and a kaolinite-rich clay with moderately disordered kaolinite modeled by a combination of an ideal and a disordered kaolinite structure (b, “KBZ”) [141].

The results from quantitative XRD analysis were verified using TG/DTG. The tangent method allows a quantification of the clay minerals based on the mass loss and the theoretical amount of crystalline bound water. However, in practice, especially when analyzing complex clays, strong overlap of the dehydroxylation processes hinder an accurate quantification. This applies in particular for 2:1 clay minerals, which contain less OH-groups than for instance kaolinite. However, in case of the latter, quantitative XRD and TG/DTG yielded comparable results (chapter 8.1, Fig. 6). It is therefore recommended to verify the determined phase contents by both methods.

4.1.2 Assessment of reactivity

As demonstrated by Avet et al. [104], the reactivity of calcined clay is largely controlled by the kaolinite content (Figure 12). However, when considering the clays with a kaolinite content less than 30 wt%, the impact of 2:1 clay minerals becomes significant. This is of major importance, since many of the economically viable clay resources lie in this range. The R^3 test, which was initially established for the reactivity assessment of calcined kaolinitic clays, was applied for the first time on calcined common clays with a broad range of mineralogical composition, where it was shown to reflect the contribution of calcined 2:1 clay minerals as well. The calculation of the calcined kaolinite content as outlined in 8.1 can be carried out adequately based on values calculated by TGA or XRD, as apparent from Figure 12.

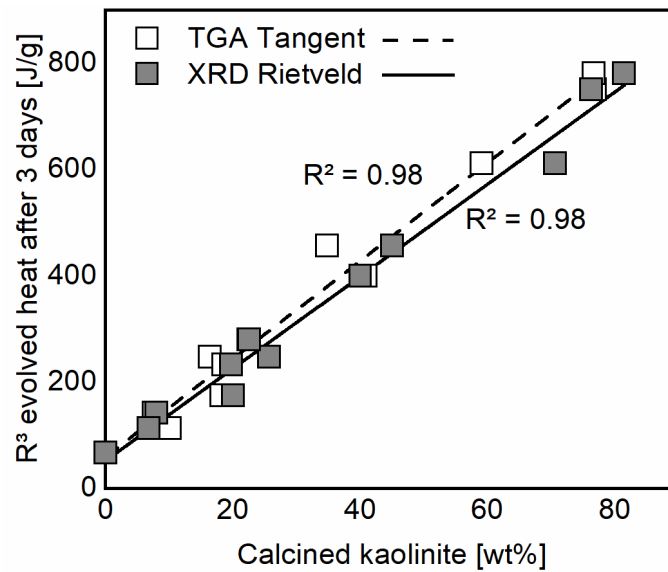


Figure 12 Correlation between calcined kaolinite content determined based on the initial kaolinite content as determined by TGA and XRD and the reactivity based on the evolved heat after 3 days R^3 reactivity test (modified after [141]).

It was further revealed for the first time that the R^3 calorimetry test is not only capable to differentiate between the general reactivity of calcined clays, but also allows conclusions on the reaction kinetic of different SCMs based on the determination of the heat flow peak. In the case of kaolinitic clays, the position of the latter was proven to be strongly influenced by the degree of disorder, while this parameter has no significant effect on the total heat after 72 h. Since the Hinckley index is prone to interference by quartz and other accompanying minerals [78] and the P_0 -index determined by FTIR is influenced by the presence of other clay minerals, the AGFI index was identified as the most reliable one (Figure 13). These correlations can further improve the assessment of clays not only based on their overall reactivity but also based on reaction kinetic, which is a decisive parameter with regards to early hydration behavior and strength development.

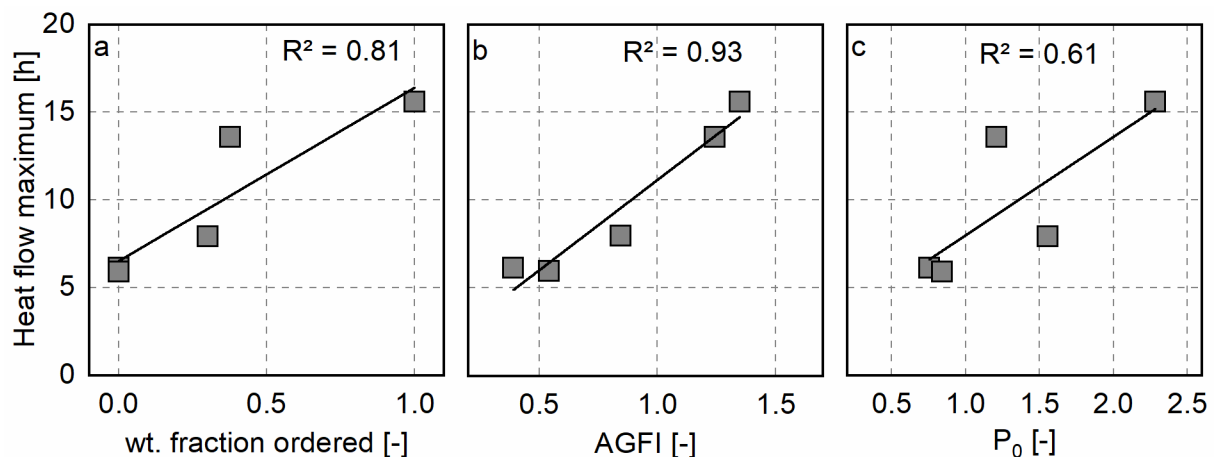


Figure 13 Connection between degree of order in kaolinite determined by the amount quantified by the ordered structure model (a), the AGFI index (b) and the P_0 -index (c) and heat flow maximum during R^3 calorimetry test.

The reactivity assessment by the R^3 test as well as Al and Si solubility provided consistent results (Fig. 5 in chapter 8.1). Both methods revealed that common clays with moderate kaolinite content and significant amount of 2:1 clay minerals can perform in the range between the established SCMs fly ash and slag [142] after proper thermal activation.

4.2 Impact of calcined clays on the early cement hydration

The silicate and aluminate clinker reaction alters significantly in presence of calcined clays. Especially the aluminate heat flow peak during isothermal calorimetry is clearly accelerated and enhanced, often resulting in a superposition of the silicate peak (Figure 14a). A restoration of two separated heat flow peaks, which is necessary for an unimpeded alite hydration, requires an addition of a significantly higher amount of sulfate carrier (4-5 wt%) based on the clinker content (Figure 14b). This chapter aims at revealing the underlying mechanisms by using two different experimental approaches.

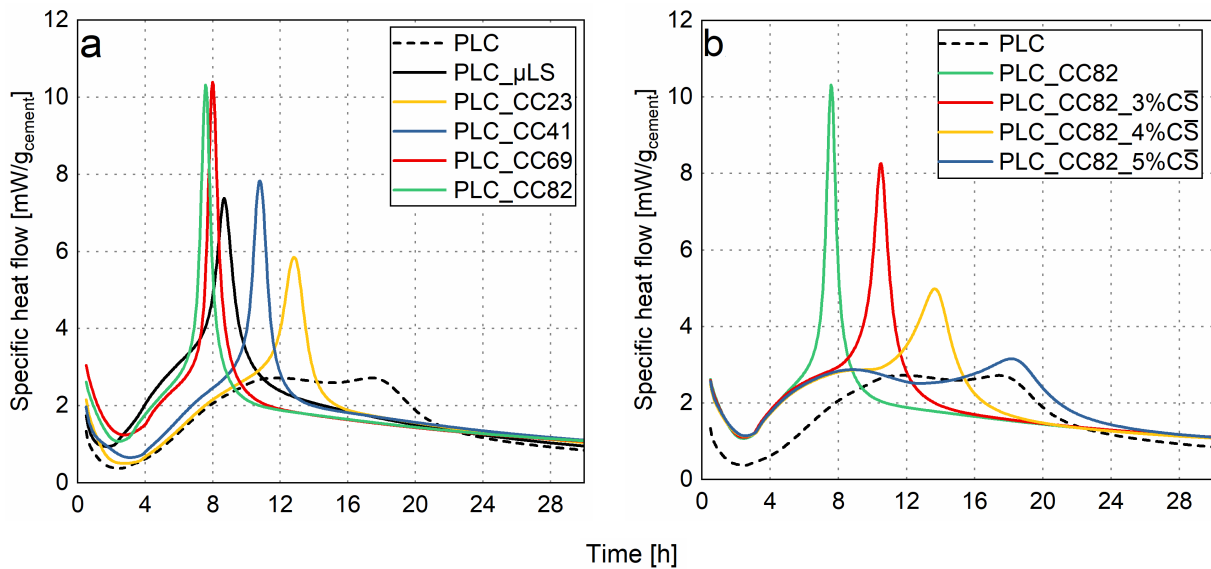


Figure 14 Heat flow curves of a) PLC blended with 30 wt% of calcined clays and limestone without extra sulfate dosage and b) PLC_CC82 with different amounts of added sulfate carrier [143].

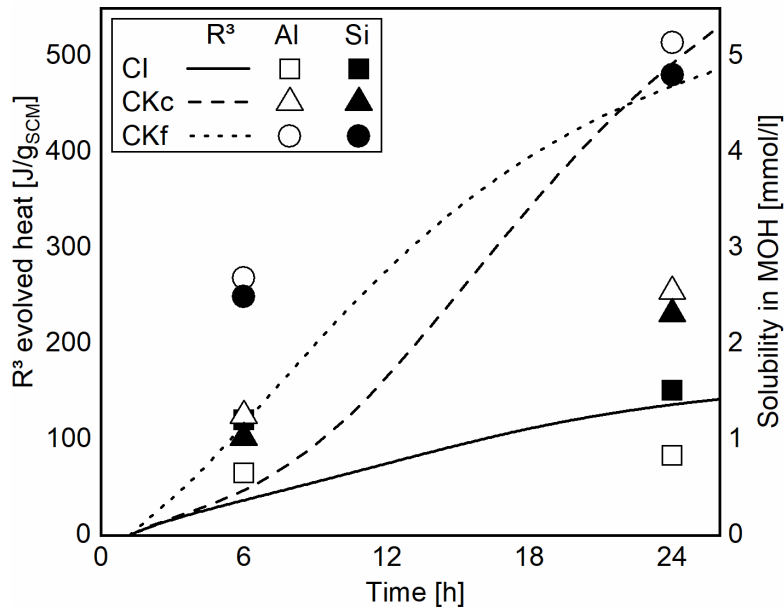
The aluminate reaction was isolated in a C_3A model system (chapter 8.2) containing cubic C_3A , a mixture of gypsum and bassanite (3:1), and quartz powder in order to simulate unhydrated clinker phases. An alkaline mixed hydroxide solution ("MOH", pH = 13.6) served to generate a reactive environment for the calcined clays in absence of portlandite. A reference system containing 10 wt% C_3A , 5 wt% gypsum and bassanite and 85 wt% Quartz was established and designated as C_3A_5CS . The impact of four different materials, namely a fine (CKf) and a coarse (CKc) calcined kaolinitic clay, an illitic clay (CI) and a nanolimestone (nLS), was investigated by replacing the quartz at different levels. The influence on a real cementitious system (chapter 8.3) was explored using a Portland limestone cement (PLC) blended with 30 wt% of four different calcined clays with different calcined kaolinite contents and SSA (CC23, CC41, CC69, CC82) resulting in LC³-type cements, and a microlimestone (μLS) in order to examine an exclusive filler effect. An overview of the investigated systems is provided in Table 3.

Table 3 Overview of the investigated systems in the C₃A model systems (top) and the PLC system (bottom).

	Quartz	C ₃ A	C \bar{S}	SCM ¹	w/s
C ₃ A_5C \bar{S} (Ref)	85	10	5	-	0.6 ³
C ₃ A_5C \bar{S} _xSCM	85-x	10	5	5, 10, 15, 20, 30	0.6 ³
C ₃ A_xC \bar{S} _20SCM	70-x	10	10, 15, 20	20	0.6 ³
	PLC		C \bar{S}	SCM	
PLC	100		2.7 ¹	-	0.5
PLC_CCXX/ μ LS	70 ²		1.9 ¹ , 3.0, 4.0, 5.0	30 ²	0.5

1) included in the PLC; 2) minus the added C \bar{S} ; 3) MOH solution

The calcined clays chosen for the investigations in both systems were selected with regards to a preferably wide range of chemical reactivity. This was achieved by using four calcined clays with different calcined kaolinite contents in the PLC system and a calcined illitic and two calcined kaolinitic clays with different degree of disorder in the C₃A model system. The assessment regarding chemical reactivity according to the methods described in chapter 8.1 is provided in Figure 15 for CI, CKc and CKf. Despite CKc containing a higher amount of calcined kaolinite than CKf, it provides a significantly lower amount of dissolved aluminum and silicon in the used MOH solution. This can well be explained by the difference in degree of order and SSA, as outlined in chapter 4.1.1.

**Figure 15** Chemical reactivity of the investigated clays in the C₃A model system using R³ test and solubility in the alkaline model solution (MOH) [144].

4.2.1 The relation of surface area and filler effect

The investigations presented in chapter 8.3 reveal that, other than in the case of fillers like quartz or limestone, there is no simple correlation in calcined clay blended cements between SSA (usually determined by nitrogen adsorption using the BET method) and acceleration of the silicate reaction. This can partly be drawn back to the strong agglomeration of clay platelets and stacking of several layers, which form a single particle (see Figure 5). This is evident from Figure 16, where no further acceleration of the silicate peak is observed between the two points

on the right. A major part of the surface of the clay platelets, which is often described as inner surface, is not available to act as nucleation area for hydrate phases, as there is too little space available. Furthermore, as the primary clay particles tend to form agglomerated, larger particles, the ability to decrease interparticle distances between the clinker grains, and thereby accelerate clinker dissolution is reduced, compared to limestone or quartz with similar SSA. Since calcined clays are able to absorb high amounts of water [124, 145], the dilution effect might be reduced as well. These mechanisms and the fact that calcite acts as preferred nucleation site for C-S-H (see chapter 2.3.3) explain, why the acceleration of the silicate peak is significantly stronger in the system with added μ LS compared to the systems with calcined clays, even if the calcined clays provide a surface area many times higher, as apparent from Figure 16. Kumar et al. [116] already observed in C_3S blends with limestone and quartz, that when the available surface area exceeds that of C_3S by a factor of 2.5, the acceleration of the hydration becomes less efficient, due to increasing agglomeration of the particles. Thus, the filler effect of calcined clays cannot be assessed by the increase of SSA alone.

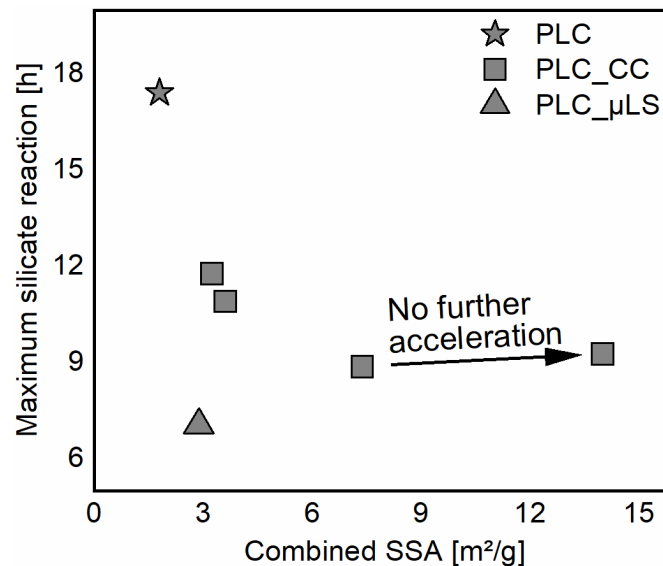


Figure 16 Correlation of the SSA of the systems blended with μ LS and different calcined clays (CC) with the appearance of the heat flow maximum of the silicate reaction. The maxima were determined in the systems with adjusted sulfate carrier from chapter 8.3.

The strong agglomeration of calcined clay particles becomes evident from the SEM images in Figure 17. The μ LS forms scattered particles that provide a higher fraction of their measured SSA as possible nucleation area. Furthermore, the scattered particles can act more efficiently in reducing the interparticle distance. CC69 provides a significantly higher SSA, which is, however, only to a small extent available as nucleation area. This is clearly identified as a further reason for the poorer physical effects of calcined clays compared to limestone with identical SSA. The physical mechanisms of SCMs reviewed in chapter 2.3.1 therefore need to be adapted for calcined clays, concerning their special surface properties that are summarized in chapter 2.1.5. These new findings mark an essential basis for the following discussions on the correlation between filler effect and accelerated aluminate reaction. Furthermore, they indicate the potential of an optimized dispersion of calcined clays, regarding enhanced early age properties.

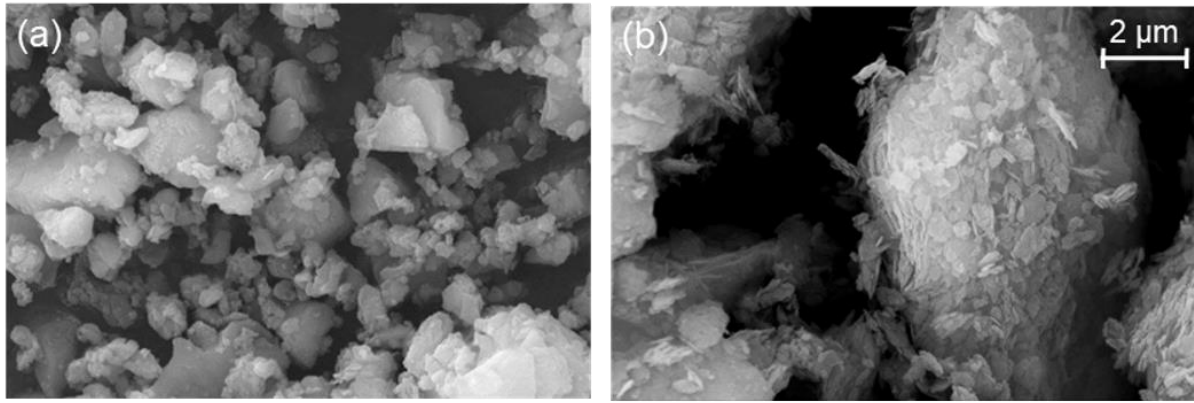


Figure 17 SEM images of the used μ LS (a) and CC69 (b), underlining the strong agglomeration of the clay platelets to form larger particles (the scale applies for both images; modified after [143])

4.2.2 Acceleration of the aluminate reaction

The acceleration of the aluminate peak in heat flow curves of calcined clay blended cement without adjusted sulfate carrier is often explained by the additional alumina provided by the calcined clay minerals, in particular metakaolin, as discussed for instance in [90]. This connection is not supported by the results obtained in the C_3A model systems. When comparing the influence of the calcined illitic clay with the calcined kaolinitic clays on the isolated C_3A hydration in the presence of calcium sulfate, the acceleration is apparently much more driven by the specific surface area (chapter 8.2). CKf and CI induce a significantly stronger acceleration of C_3A hydration compared to CKc due to their higher SSA and despite their lower metakaolin content (Figure 18). These observations also contradict the theory that the acceleration of sulfate depletion is dominantly caused by adsorption of sulfate onto C-S-H, which is faster precipitated due to the filler effect [121], as they were made in absence of a silicate reaction.

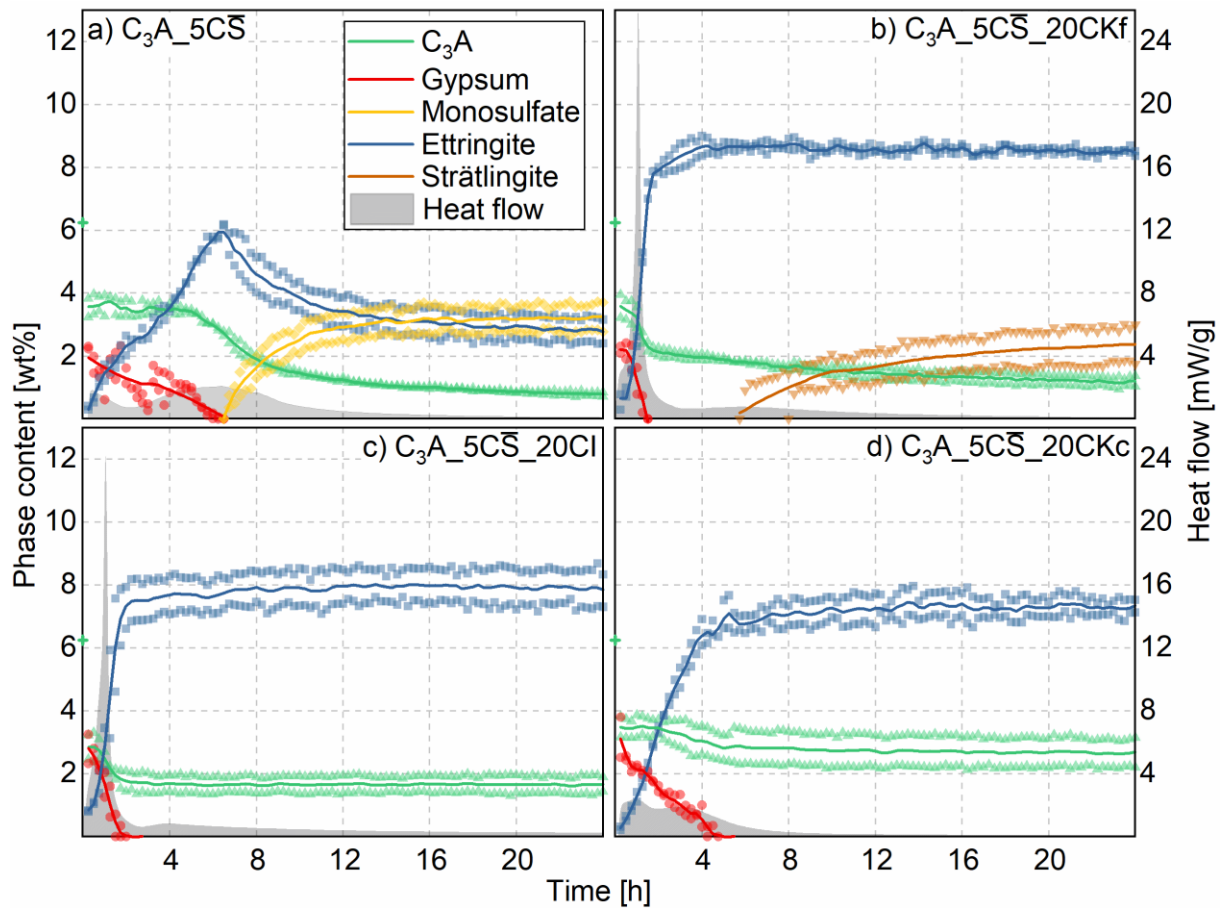


Figure 18 Phase development and heat flow curves in the C_3A model systems with 5 wt% CS
a) without calcined clay (Ref 5%), b) with 20 wt% CKf, c) with 20 wt% Cl and d) with 20 wt% CKc [144]

A sole explanation of the observations by the additional supply of surface area as nucleation site was furthermore refuted by a correlation of the combined surface areas of the systems with the sulfate depletion peak, revealing that there are significant differences depending on the type of calcined clay (Figure 19). Evidence for a chemical contribution of the calcined clay could only be gathered in the systems with CKf, where formation of strätlingite follows sulfate depletion (Figure 18). However, it is remarkable that the formation of monosulfate is suppressed in the systems with Cl and CKc. This was led back to a stabilization of ettringite as it was found by XRD measurements after 7 days, where the thermodynamic stable AFm phase was found to be strätlingite. The reason why this phase could not be detected during the first 24 h of hydration is the lower solubility of silicon from Cl and CKc compared to CKf (Figure 15).

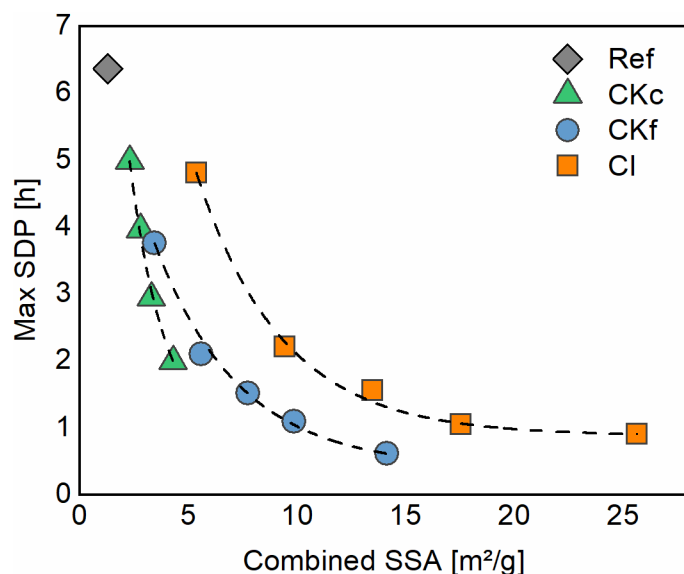


Figure 19 Correlation between combined SSA of C₃A model systems Ref, CKc, CKf and CI and the maximum of sulfate depletion peak (SDP) (modified after [144]). Variation of SSA was realized by using different replacement levels between 5 and 30 wt% Further details are given in chapter 8.2.

These findings are corroborated by results obtained in the PLC system blended with 30 wt% of calcined clays or μ LS, respectively (chapter 8.3). Even though the μ LS induces a significant acceleration of the aluminate peak as well, which can be well explained by the theory elaborated in [121], the effects of the metakaolin-rich calcined clays exceed this mechanism. This becomes most evident from Figure 20, which was compiled based on the results obtained by quantitative XRD (chapter 8.3, Fig. A1). This figure considers the amount of sulfate that is bound by ettringite at the onset point of the aluminate reaction. The remaining sulfate needs to be assigned to other solid sulfate hosts or the pore solution. Based on the amount of C₃S reacted until aluminate onset, a S/Ca ratio of 0.04-0.06 [146] and a C-S-H composition of C_{1.7}SH_{2.6-4.0}, a grey area that represents the amount of sulfate possibly adsorbed onto C-S-H was calculated. The intercept of this area with the x-axis considers a theoretical amount of 0.1-0.2 wt% SO₃ dissolved in the pore solution, which matches with the intercept of the extrapolated lines that connect the differently sulfated systems (PLC_ μ LS and PLC_CC69/CC82). This approach indicates that there exists at least one other significant sulfate host in the metakaolin-rich systems (PLC_CC69/CC82). This can however not be assigned to additionally formed ettringite as the difference between the blended systems is minor and this amount is already considered in the calculation. As elaborated in chapter 8.2, most evidence can be gathered for an adsorption of sulfate onto the metakaolin surface (or the surface of other dehydroxylated clay minerals, respectively). Calcined clay minerals reveal a negative surface charge, which is reflected by their strongly negative zeta potential. It was proven by other authors before (e.g. in [48]) and also in the present work, that Ca²⁺ is strongly attracted by this surface. The positively charged calcium layer then provides the ability to adsorb SO₄²⁻. The adsorption capacity increases with surface area and charge. Other than C-S-H, which only starts to form significantly during acceleration period, this surface is available right from the start of C₃A hydration.

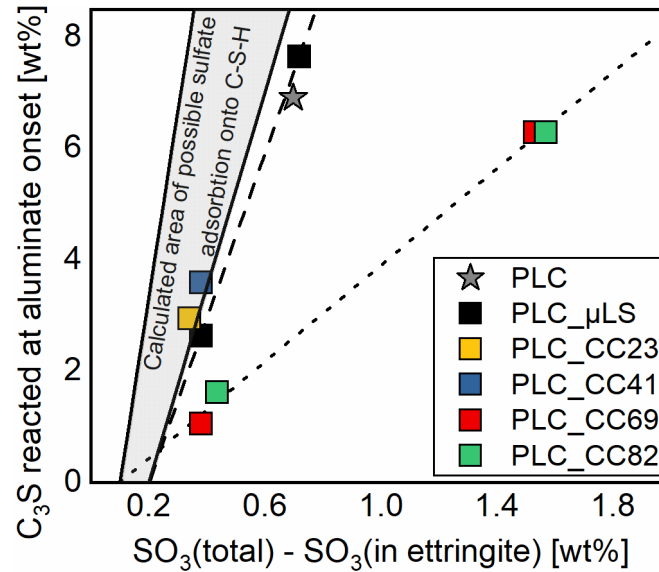


Figure 20 Correlation of SO_3 content (taking into account the SO_3 bound by ettringite) and amount of reacted C_3S at the aluminate onset [143].

Another observation indicating a different reaction mechanism in the PLC_CC systems and the PLC_μLS is the difference in the shape of the aluminate heat flow peak. This peak usually becomes narrower when appearing earlier and broader when it is retarded by additional sulfate (Figure 14). When comparing PLC_CC with PLC_μLS, the latter always reveals a broader aluminate peak even when occurring at the same position in time (chapter 8.3, Fig. 9). This indicates a faster ettringite precipitation in the calcined clay blended systems when the solid sulfate is depleted. Three possible reasons were found for these observations, namely a preferred nucleation site for ettringite on the MK surface, a slightly increased amount of aluminum in the pore solution through the beginning dissolution of MK and a faster release of adsorbed sulfate by the MK compared to C-S-H.

4.3 Mechanisms behind the increased sulfate demand of calcined clay blended cements

A comparison of results obtained in chapter 8.2 and 8.3 reveals an adsorption of sulfate or, more likely, Ca-SO_4 complexes onto the surface of the calcined clay minerals as the most evident mechanism explaining the discrepancy in the acceleration of sulfate depletion between limestone (or other fillers respectively) and calcined clays. This is illustrated in Figure 21, where the reference system from chapter 8.2 (a) is compared with the corresponding system containing MK (b). The weaker surface charge and the significantly lower SSA of quartz (or possibly other fillers) only yields a marginal adsorption of Ca and SO_4 ions. The surface of the MK on the other hand competes strongly for sulfate ions with the C_3A surface and thereby inhibits its retardation. Consequently, C_3A dissolves faster and supplies more aluminum to the pore solution. This in turn leads to a faster consumption of sulfate by ettringite, which accelerates C_3A dissolution on top.

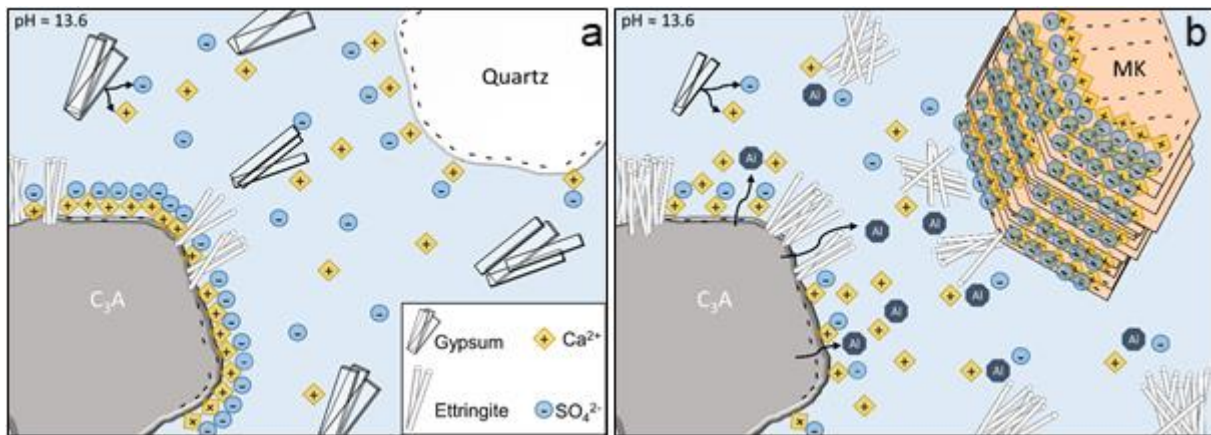


Figure 21 Model of adsorption mechanisms inhibiting the retardation of C_3A hydration in the C_3A -Quartz-Gypsum system (a) and the C_3A -Quartz-Gypsum-MK system (b).

The findings from the sulfate adjustment experiments in chapter 8.2 however cannot be explained solely by the adsorption mechanisms. While a further dissolution of C_3A can be inhibited by sulfate addition in the system with CI, the system with CKf allows no retardation at all. This is evident from Figure 22a,b, where in the system with CKf an addition of sulfate just leads to increased heat development due to more precipitation of ettringite, while in the presence of CI the C_3A hydration is inhibited above 10 wt% of $C\bar{S}$. This indicates, that at this point, a chemical contribution from the MK may be assumed. The incongruent dissolution of C_3A [93], which leads to the formation of the Al-rich leached layer [52], causes a deficit of Al compared to Ca with respect to ettringite formation. This deficit is eliminated, when the MK acts as a secondary Al source. As this Al reacts with Ca leached from or adsorbed onto the Al-rich layer at the C_3A surface, the inhibiting mechanism is overcome and C_3A dissolution continues on a high level until its depletion (chapter 8.2, Fig.11B). This is further supported by Figure 22c, where the development of ettringite content in the C_3A model system with 20 wt% $C\bar{S}$ and 20 wt% CKf or 20 wt% CI is depicted. Based on the C_3A (10 wt%) and the $C\bar{S}$ content, a theoretical ettringite content of 28.5 wt% can be calculated, which is reached in the CKf system, but by far not in the CI system. Even though, both types of calcined clay lead to a similar acceleration of the aluminat reaction in the systems with 5 wt% $C\bar{S}$, the system with CI allows a retardation through sulfate addition, while the one with CKf does not.

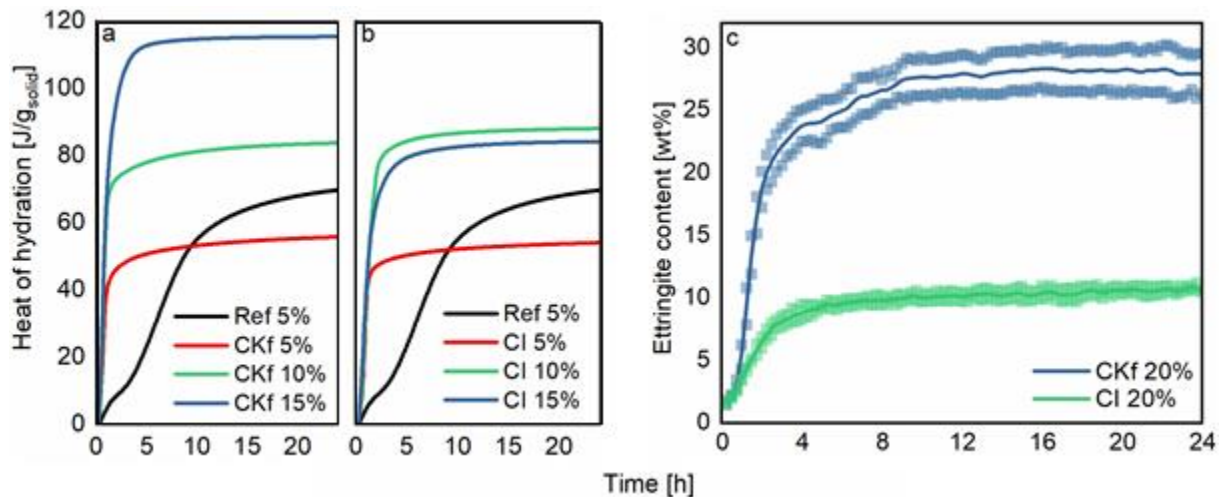


Figure 22 Evolved heat of the C₃A model systems with a) 20 wt% calcined fine kaolinitic clay (CKf) and b) 20 wt% of calcined illitic clay (CI) and different amounts of C \bar{S} . (c) provides the ettringite formation in the C₃A model systems with 20 wt% C \bar{S} and 20 wt% CKf or 20 wt% CI.

The findings from the model systems can also hold as one reason for the increased amount of sulfate required for an optimum sulfation in the calcined clay blended PLC systems compared to the PLC_ μ LS. Even though the sulfate depletion peak in the systems PLC_ μ LS and PLC_CC69/82 without sulfate adjustment occur almost simultaneously, the latter two systems require between 4 and 5 wt% of C \bar{S} for a proper sulfation, while PLC_ μ LS only demands 3 wt%. It is already known that if sufficient sulfate is available, the aluminum provided by the metakaolin can contribute to ettringite formation [125]. The calcined clay's reactivity depends on the amount of metakaolin (or to a lower extend other calcined clay minerals) on the one hand but also on the degree of disorder and SSA on the other (see Figure 12, Figure 13 and Figure 15). A possible additional ettringite formation through consumption of aluminum from the metakaolin was found not to be the main driving force for the acceleration of the aluminate reaction in undersulfated systems in the presented thesis. However, it may well be considered as a factor explaining the higher sulfate demand for proper sulfation in the calcined kaolinite-rich systems, since the effect becomes more significant when the sulfate depletion peak is shifted to later points in time.

5 Conclusion

The findings presented in this thesis contribute to an improved understanding of the relation between mineralogical composition of clays and their pozzolanic reactivity after calcination. They further provide a significant extension of the so far known reaction mechanisms of calcined clays during early hydration and their impact on clinker reaction and sulfate demand.

An extensive mineralogical characterization of 13 different clay-rich raw materials laid the groundwork for a correlation of raw clay properties and pozzolanic reactivity after calcination. A separate XRD analysis of the $< 2 \mu\text{m}$ fraction in air-dried and glycolated condition and the implementation of structure models for strongly disordered clay minerals during Rietveld refinement of the bulk samples, supported by FTIR and TG/DTG measurements, allowed a reliable discrimination and quantification of the clay minerals contained. This is crucial in order to assess their particular influence on the reactivity after thermal activation. Especially for clays with a kaolinite content below 30 wt%, the influence of 2:1 clay minerals like smectites or Illite-smectite interstratifications becomes significant. These kinds of clays exhibit reactivity in the range between established SCMs like fly ash or slag. Solubility of aluminum and silicon ions in alkaline solution and R^3 calorimetry test yielded consistent results, while the latter was shown to allow conclusions on the reaction kinetics as well, based on the rate of heat development. The degree of kaolinite disorder, which was shown to be characterized most reliably based on the AGFI derived from XRD, was identified as the most significant parameter determining the reaction rate of calcined kaolinitic clays.

The impact of calcined clays on the aluminate clinker reaction was initially examined in a model system containing cubic C_3A and calcium sulfate in an alkaline model solution. Calcined kaolinitic as well as illitic clay strongly accelerates the hydration rate of cubic C_3A and the associated ettringite formation, while limestone does not. The most likely mechanism for this acceleration was found to be the adsorption of calcium and sulfate ions or ion pair complexes onto the surface of the clay minerals, disabling the retardation mechanisms on the surface of C_3A . Thus, this mechanism, which was previously attributed to C-S-H only, can also take place in absence of a silicate reaction. The calcined kaolinitic clays revealed a stronger acceleration compared to the illitic clay normalized with respect to the surface area. An adjustment of the sulfate content reveals a diverse impact depending on the respective calcined clay, demonstrating that a retardation of a highly reactive calcined kaolinitic clay is not possible in the investigated model system. This can be attributed to the supply of aluminum by the metakaolin, consuming further calcium and sulfate. A chemical contribution of the metakaolin in this system was further proved by the formation of strätlingite, already after 6 h.

The findings obtained from the synthetic C_3A systems are supported by investigations in a blended Portland limestone cement. The ratio of acceleration of aluminate reaction to the acceleration of silicate reaction is significantly higher in calcined clay blended cements compared to cements with a fine limestone filler, which confirmed another significant sulfate host in calcined clay blended cements that was assigned to adsorption mechanisms onto the calcined clay minerals. Sulfate consumption by ettringite including aluminum from the metakaolin only plays a role at later times but can increase the sulfate demand needed for a proper retardation. It was shown that the systems blended with the calcined kaolinite-rich clays need an overall amount of up to 5 wt% calcium sulfate to reach proper sulfation, which is a further argument for using clays with kaolinite contents below 50 wt%.

6 Perspectives

The first part of this thesis revealed a broad range of suitable clays for the production of SCMs and methods to characterize them and assess their reactivity. Especially for the economically interesting and in Central Europe widely available 2:1 clay mineral resources, an elaboration of classification criteria and exploration guidelines needs to be provided in order to promote their application. Even though the applied reactivity tests were shown to work and correlate well, accelerated test methods would be desirable, especially regarding production control.

The results obtained in the second part of this thesis have shown that calcined clays can behave significantly different than established SCMs during early hydration, to a large extent due to their complex surface properties and the resulting interaction with ions from the pore solution. The surface chemistry of dehydroxylated clay minerals is not yet adequately studied and requires further fundamental research. This is not only an important requisite for an improved understanding of the interaction between calcined clay minerals and ionic species provided by the dissolution of cement phases but also regarding the interaction with superplasticizer.

A quantification of the dissolving cement phases and precipitating hydrates could be partly used for a differentiation between chemical and physical effects. However, a clear delimitation is not possible based on the obtained data. In order to assess the impact of ions – especially aluminum – provided by the dissolution of calcined clay minerals before the onset of the aluminate reaction, their quantification during the first hours by the PONKCS method is mandatory. This is however challenging due to the complex phase assemblage in calcined clay blended or LC³-cements and needs to be established using simplified model cements.

In the investigations, cements blended with highly kaolinitic clay were required up to 5 wt% of C \bar{S} to reach an optimal sulfation based on the calorimetry curves. In the light of normative limits, other options to adjust the time of the aluminate reaction should be explored. In case of calcined kaolinite-rich clays, it might be favorable to dilute them with fillers that could enhance the early alite reactivity without accelerating the aluminate reactivity to such an extent as metakaolin.

The lower acceleration of the silicate reaction by the calcined clays compared to limestone was partly attributed to the strong agglomeration of the calcined clay platelets. An optimum dispersion of the mixtures, for instance through additives or high shear mixing, might further accelerate the silicate reaction and thereby improve early age properties.

Mechanisms explaining the sharper peak shape of the aluminate heat flow peak in the presence of calcined clays have been discussed, however, they need to be further examined in future studies. The adsorption of calcium and sulfate onto the surface of calcined clay minerals requires further exploration and quantitative assessment. A quantitative comparison between sulfate uptake by C-S-H and metakaolin could further clarify the acceleration mechanisms of the aluminate reaction in calcined clay blended cement.

7 References

1. IEA, *Technology Roadmap - Low-Carbon Transition in the Cement Industry*. 2018.
2. Habert, G., et al., *Environmental impacts and decarbonization strategies in the cement and concrete industries*. *Nature Reviews Earth & Environment*, 2020. **1**(11): p. 559-573.
3. Scrivener, K.L., V.M. John, and E.M. Gartner, *Eco-efficient cements: Potential economically viable solutions for a low-CO₂ cement-based materials industry*. *Cement and Concrete Research*, 2018. **114**: p. 2-26.
4. Schneider, M., *The cement industry on the way to a low-carbon future*. *Cement and Concrete Research*, 2019. **124**: p. 105792.
5. Snellings, R., G. Mertens, and J. Elsen, *Supplementary Cementitious Materials*. *Reviews in Mineralogy and Geochemistry*, 2012. **74**(1): p. 211-278.
6. Beuntner, N., R. Sposito, and K.-C. Thienel, *Potential of Calcined Mixed-Layer Clays as Pozzolans in Concrete*. *ACI Materials Journal*, 2019. **116**(4): p. 19-29.
7. Zunino, F., F. Martirena Hernández, and K. Scrivener, *Limestone Calcined Clay Cements (LC3)*. *ACI Materials Journal*, 2021. **118**(3): p. 49-60.
8. Sharma, M., et al., *Limestone calcined clay cement and concrete: A state-of-the-art review*. *Cement and Concrete Research*, 2021. **149**: p. 106564.
9. Schulze, S.E. and J. Rickert, *Suitability of natural calcined clays as supplementary cementitious material*. *Cement and Concrete Composites*, 2019. **95**: p. 92-97.
10. Antoni, M., et al., *Cement substitution by a combination of metakaolin and limestone*. *Cement and Concrete Research*, 2012. **42**(12): p. 1579-1589.
11. Beuntner, N., *Zur Eignung und Wirkungsweise calcinierter Tone als reaktive Bindemittelkomponente in Zement (On the suitability and mode of action of calcined clays as reactive binder components in cement)*, in *Fakultät für Bauingenieurwesen und Umweltwissenschaften*. 2017, Universität der Bundeswehr München: Neubiberg. p. 207.
12. Guggenheim, S. and R.T. Martin, *Definition of Clay and Clay Mineral: Joint Report of the Aipea and CMS Nomenclature Committees*. *Clay Minerals*, 1995. **30**(3): p. 257-259.
13. 14688-1:2017, I., *Geotechnical investigation and testing — Identification and classification of soil — Part 1: Identification and description*. 2017. p. 23.
14. Wentworth, C.K., *A Scale of Grade and Class Terms for Clastic Sediments*. *The Journal of Geology*, 1922. **30**(5): p. 377 - 392.
15. Bergaya, F., et al., *Handbook of Clay Science*. First ed. *Developments in Clay Science*. 2006, Oxford, UK: Elsevier. 1225.
16. Bergaya, F. and G. Lagaly, *Chapter 1 General Introduction: Clays, Clay Minerals, and Clay Science*, in *Developments in Clay Science*, F. Bergaya, B.K.G. Theng, and G. Lagaly, Editors. 2006, Elsevier. p. 1-18.
17. Hanein, T., et al., *Clay calcination technology: state-of-the-art review by the RILEM TC 282-CCL*. *Materials and Structures*, 2021. **55**(1): p. 3.
18. Alujas Diaz, A., et al., *Properties and occurrence of clay resources for use as supplementary cementitious materials. A paper of RILEM TC 282-CCL*. *Materials and Structures*, 2022. **Accepted for publication**.
19. Jasmund, K., et al., *Tonminerale und Tone: Struktur, Eigenschaften, Anwendungen und Einsatz in Industrie und Umwelt*. 1993, Darmstadt: Dr. Dietrich Steinkopff Verlag. XIV, 490.
20. Galán, E., *Chapter 14 Genesis of Clay Minerals*, in *Developments in Clay Science*, F. Bergaya, B.K.G. Theng, and G. Lagaly, Editors. 2006, Elsevier. p. 1129-1162.
21. Stein, V., *The raw materials for brick and tile making*, in *Brick and tile making*, W.F. Bender and F. Händle, Editors. 1982, Bauverlag: Bauverlag. p. 73-94.
22. Strakhov, N.M., *Principles of Lithogenesis*. 1 ed. Vol. 1-3. 1967, New York, NY, USA: Springer, Boston, MA. XXXI, 1453.
23. Ito, A. and R. Wagai, *Global distribution of clay-size minerals on land surface for biogeochemical and climatological studies*. *Scientific Data*, 2017. **4**(1): p. 170103.

24. Dill, H.G. and S. Röhling, *Map of Mineral Resources of Germany 1: 1 000 000 (BSK1000)*, BGR, Editor. 2007: Hannover.
25. Toloczyki, M., et al., *Geological Map of Germany 1:1,000,000 (GK1000)*, BGR, Editor. 2006: Hannover.
26. Maier, M., N. Beuntner, and K.-C. Thienel, *An approach for the evaluation of local raw material potential for calcined clay as SCM, based on geological and mineralogical data: Examples from German clay deposits*, in *Calcined Clays for Sustainable Concrete - Proceedings of the 3rd International Conference on Calcined Clays for Sustainable Concrete*, S. Bishnoi, Editor. 2020, Springer: Singapore. p. 37-47.
27. Moore, D.M. and R.C.J. Reynolds, *X-Ray Diffraction and the Identification and Analysis of Clay Minerals*. 2 ed. Geological Magazine. 1997, Oxford, New York: Cambridge University Press. 322, XVI.
28. Gräfe, M., A. McFarlane, and C. Klauber, *Clays and the Minerals Processing Value Chain (MPVC)*, in *Clays in the Minerals Processing Value Chain*, A.J. McFarlane, et al., Editors. 2017, Cambridge University Press: Cambridge, UK. p. 1-80.
29. Brigatti, M., E. Galán, and B. Theng, *Structures and Mineralogy of Clay Minerals*, in *Developments in Clay Science*, F. Bergaya, B.K.G. Theng, and G. Lagaly, Editors. 2013, Elsevier: Amsterdam. p. 21-81.
30. Bish, D.L. and R.B. Von Dreele, *Rietveld Refinement of Non-Hydrogen Atomic Positions in Kaolinite*. *Clays and Clay Minerals*, 1989. **37**(4): p. 289-296.
31. Aparicio, P., et al., *Interstratified Clay Minerals: Origin, Characterization and Geochemical Significance*. AIPEA Educational Series. Vol. 1. 2013, Bari: Digilabs.
32. Garg, N. and J. Skibsted, *Dissolution kinetics of calcined kaolinite and montmorillonite in alkaline conditions: Evidence for reactive Al(V) sites*. *Journal of the American Ceramic Society*, 2019. **102**(12): p. 7720-7734.
33. Skibsted, J. and R. Snellings, *Reactivity of supplementary cementitious materials (SCMs) in cement blends*. *Cement and Concrete Research*, 2019. **124**: p. 105799.
34. Tatarin, A. and R. Vogt, *Test methods for heavy clay ceramic raw materials: Raw material composition (primary properties) - Part 1*. *Brick and Tile Industry International*, 2013: p. 20-34.
35. Fernandez, R., F. Martirena, and K.L. Scrivener, *The origin of the pozzolanic activity of calcined clay minerals: a comparison between kaolinite, illite and montmorillonite*. *Cement and Concrete Research*, 2011. **41**(1): p. 113-122.
36. Tironi, A., et al., *Kaolinitic calcined clays: Factors affecting its performance as pozzolans*. *Construction and Building Materials*, 2012. **28**(1): p. 276-281.
37. Dietel, J., et al., *The importance of specific surface area in the geopolymerization of heated illitic clay*. *Applied Clay Science*, 2017. **139**: p. 99-107.
38. Hollanders, S., et al., *Pozzolanic reactivity of pure calcined clays*. *Applied Clay Science*, 2016. **132–133**: p. 552-560.
39. Hanein, T., et al., *Clay calcination technology: state-of-the-art review by the RILEM TC 282-CCL*. *Materials and Structures*, 2022. **55**(3): p. 29.
40. Bellotto, M., et al., *Kinetic study of the kaolinite-mullite reaction sequence. Part I: Kaolinite dehydroxylation*. *Physics and Chemistry of Minerals*, 1995. **22**(4): p. 207-217.
41. Drits, V.A., G. Besson, and F. Muller, *An Improved Model for Structural Transformations of Heat-Treated Aluminous Dioctahedral 2:1 Layer Silicates*. *Clays and Clay Minerals*, 1995. **43**(6): p. 718-731.
42. Steudel, A. and K. Emmerich, *Strategies for the successful preparation of homoionic smectites*. *Applied Clay Science*, 2013. **75-76**: p. 13-21.
43. Salmang, H. and H. Scholze, *Keramik*. 7. ed. 2007: Springer-Verlag Berlin/Heidelberg, Germany. 1165.
44. Schoonheydt, R.A. and C.T. Johnston, *Chapter 3 Surface and Interface Chemistry of Clay Minerals*, in *Developments in Clay Science*, F. Bergaya, B.K.G. Theng, and G. Lagaly, Editors. 2006, Elsevier: Oxford, UK. p. 87-113.

45. Kumar, N., et al., *Probing the Surface Charge on the Basal Planes of Kaolinite Particles with High-Resolution Atomic Force Microscopy*. Langmuir, 2017. **33**(50): p. 14226-14237.
46. Forbes, E. and A. Chryss, *Fundamentals of Clays Surface and Colloid Science, and Rheology*, in *Clays in the Minerals Processing Value Chain*, A.J. McFarlane, et al., Editors. 2017, Cambridge University Press: Cambridge, UK. p. 81-110.
47. Lei, L. and J. Plank, *A study on the impact of different clay minerals on the dispersing force of conventional and modified vinyl ether based polycarboxylate superplasticizers*. Cement and Concrete Research, 2014. **60**: p. 1-10.
48. Li, R., et al., *Effectiveness of PCE superplasticizers in calcined clay blended cements*. Cement and Concrete Research, 2021. **141**: p. 106334.
49. Schmid, M. and J. Plank, *Interaction of individual meta clays with polycarboxylate (PCE) superplasticizers in cement investigated via dispersion, zeta potential and sorption measurements*. Applied Clay Science, 2021. **207**: p. 106092.
50. Pardo, P., et al. *Surface properties of calcined clays and their dispersion in blended Portland cement pastes*. in *13th International Congress on the Chemistry of Cement*. 2011. Madrid, Spain.
51. Jansen, D., et al., *The early hydration of OPC investigated by in-situ XRD, heat flow calorimetry, pore water analysis and 1H NMR: Learning about adsorbed ions from a complete mass balance approach*. Cement and Concrete Research, 2018. **109**: p. 230-242.
52. Myers, R.J., et al., *Role of Adsorption Phenomena in Cubic Tricalcium Aluminate Dissolution*. Langmuir, 2017. **33**(1): p. 45-55.
53. Artioli, G. and J.W. Bullard, *Cement hydration: the role of adsorption and crystal growth*. Crystal Research and Technology, 2013. **48**(10): p. 903-918.
54. Johnston, C.T., *Probing the nanoscale architecture of clay minerals*. Clay Minerals, 2010. **45**(3): p. 245-279.
55. Rutherford, D.W., C. Chiou, and D. Eberl, *Effects of Exchanged Cation on the Microporosity of Montmorillonite*. Clays and Clay Minerals - CLAYS CLAY MINER, 1997. **45**(4): p. 534-543.
56. Lagaly, G. and I. Dékány, *Colloid Clay Science*, in *Developments in Clay Science*, F. Bergaya and G. Lagaly, Editors. 2013, Elsevier. p. 243-345.
57. Celia Magno, M., et al., *A comparison between Laser Granulometer and Sedigraph in grain size analysis of marine sediments*. Measurement, 2018. **128**: p. 231-236.
58. Czurda, K., *Chapter 11.3 Clay Liners and Waste Disposal*, in *Developments in Clay Science*, F. Bergaya, B.K.G. Theng, and G. Lagaly, Editors. 2006, Elsevier. p. 693-701.
59. Snellings, R., et al., *Paper of RILEM TC 282-CCL: Mineralogical characterization methods for clay resources intended for use as supplementary cementitious material*. Materials and Structures, 2022. **Accepted for publication**.
60. Ufer, K. and M.D. Raven, *Application of the Rietveld Method in the Reynolds Cup Contest*. Clays and Clay Minerals, 2017. **65**(4): p. 286-297.
61. Kleeberg, R., T. Monecke, and S. Hillier, *Preferred orientation of mineral grains in sample mounts for quantitative XRD measurements: How random are powder samples?* Clays and Clay Minerals, 2008. **56**(4): p. 404-415.
62. Dollase, W.A., *Correction of intensities for preferred orientation in powder diffractometry: application of the March model*. Journal of Applied Crystallography, 1986. **19**: p. 267-272.
63. Bergmann, J., T. Monecke, and R. Kleeberg, *Alternative algorithm for the correction of preferred orientation in Rietveld analysis*. Journal of Applied Crystallography, 2001. **34**(1): p. 16-19.
64. M. Butler, B. and S. Hillier, *Automated Full-Pattern Summation of X-Ray Powder Diffraction Data for High-Throughput Quantification of Clay-Bearing Mixtures*. Clays and Clay Minerals, 2021. **69**(1): p. 38-51.
65. Cheary, R.W. and A. Coelho, *A fundamental parameters approach to X-ray line-profile fitting*. Journal of Applied Crystallography, 1992. **25**(2): p. 109-121.

66. Rietveld, H.M., *A profile refinement method for nuclear and magnetic structures*. Journal of applied Crystallography, 1969. **2**(2): p. 65-71.
67. Ufer, K., et al., *QUANTITATIVE PHASE ANALYSIS OF BENTONITES BY THE RIETVELD METHOD*. Clays and Clay Minerals, 2008. **56**(2): p. 272-282.
68. Ufer, K., et al., *Rietveld Refinement of Disordered Illite-Smectite Mixed-Layer Structures by a Recursive Algorithm. II: Powder-Pattern Refinement and Quantitative Phase Analysis*. Clays and Clay Minerals, 2012. **60**(5): p. 535-552.
69. Ufer, K., R. Kleeberg, and T. Monecke, *Quantification of stacking disordered Si–Al layer silicates by the Rietveld method: application to exploration for high-sulphidation epithermal gold deposits*. Powder Diffraction, 2015. **30**(S1): p. S111-S118.
70. Coelho, A.A., J.S.O. Evans, and J.W. Lewis, *Averaging the intensity of many-layered structures for accurate stacking-fault analysis using Rietveld refinement*. Journal of Applied Crystallography, 2016. **49**(5): p. 1740-1749.
71. Doebelin, N. and R. Kleeberg, *Profex: a graphical user interface for the Rietveld refinement program BGMN*. Journal of Applied Crystallography, 2015. **48**(5): p. 1573-1580.
72. Bergmann, J., P. Friedel, and R. Kleeberg, *BGMN – a new fundamental parameter based Rietveld program for laboratory X-ray sources, its use in quantitative analysis and structure investigations*. Commission on Powder Diffraction Newsletter, 1998. **20**: p. 5-8.
73. Coelho, A., *TOPAS and TOPAS-Academic: an optimization program integrating computer algebra and crystallographic objects written in C++*. Journal of Applied Crystallography, 2018. **51**(1): p. 210-218.
74. Scarlett, N.V.Y. and I.C. Madsen, *Quantification of phases with partial or no known crystal structures*. Powder Diffraction, 2006. **21**(04): p. 278-284.
75. Taylor, J.C. and C.E. Matulis, *A new method for Rietveld clay analysis. Part I. Use of a universal measured standard profile for Rietveld quantification of montmorillonites*. Powder Diffraction, 1994. **9**(2): p. 119-123.
76. Lorentz, B., et al., *Characterization of Florida kaolin clays using multiple-technique approach*. Applied Clay Science, 2018. **161**: p. 326-333.
77. Hinckley, D.N., *Variability in "crystallinity" values among the kaolin deposits of the coastal plain of Georgia and South Carolina*. Clays and Clay Minerals, 1963. **11**: p. 229-235.
78. Aparicio, P., E. Galán, and R. Ferrell, *A new kaolinite order index based on XRD profile fitting*. Clay Minerals, 2006. **41**: p. 811-817.
79. Bullard, J.W., et al., *Mechanisms of cement hydration*. Cement and Concrete Research, 2011. **41**(12): p. 1208-1223.
80. Hesse, C., F. Goetz-Neunhoffer, and J. Neubauer, *A new approach in quantitative in-situ XRD of cement pastes: Correlation of heat flow curves with early hydration reactions*. Cement and Concrete Research, 2011. **41**(1): p. 123-128.
81. Scrivener, K.L. and A. Nonat, *Hydration of cementitious materials, present and future*. Cement and Concrete Research, 2011. **41**(7): p. 651-665.
82. Scrivener, K., P. Juilland, and P.J.M. Monteiro, *Advances in understanding hydration of Portland cement*. Cement and Concrete Research, 2015.
83. Scrivener, K., et al., *Advances in understanding cement hydration mechanisms*. Cement and Concrete Research, 2019. **124**: p. 105823.
84. Juilland, P., et al., *Dissolution theory applied to the induction period in alite hydration*. Cement and Concrete Research, 2010. **40**(6): p. 831-844.
85. Juilland, P., et al., *Advances in dissolution understanding and their implications for cement hydration*. RILEM Technical Letters, 2017. **2**(0): p. 90-98.
86. Bergold, S.T., F. Goetz-Neunhoffer, and J. Neubauer, *Interaction of silicate and aluminate reaction in a synthetic cement system: Implications for the process of alite hydration*. Cement and Concrete Research, 2017. **93**: p. 32-44.
87. Bergold, S.T., F. Goetz-Neunhoffer, and J. Neubauer, *Quantitative analysis of C–S–H in hydrating alite pastes by in-situ XRD*. Cement and Concrete Research, 2013. **53**: p. 119-126.

88. Hesse, C., *Der Reaktionsverlauf der frühen Hydratation von Portlandzement in Relation zur Temperatur*, in *Naturwissenschaftliche Fakultät*. 2009, Friedrich-Alexander-Universität Erlangen-Nürnberg.
89. Jansen, D., et al., *The early hydration of Ordinary Portland Cement (OPC): An approach comparing measured heat flow with calculated heat flow from QXRD*. Cement and Concrete Research, 2012. **42**(1): p. 134-138.
90. Andrade Neto, J.d.S., A.G. De la Torre, and A.P. Kirchheim, *Effects of sulfates on the hydration of Portland cement – A review*. Construction and Building Materials, 2021. **279**: p. 122428.
91. Taylor, H.F.W., *Cement Chemistry*. 2. ed. 1997, London: Thomas Telford Ltd. 459.
92. Kirchheim, A.P., et al., *Analysis of cubic and orthorhombic C3A hydration in presence of gypsum and lime*. Journal of Materials Science, 2009. **44**(8): p. 2038-2045.
93. Myers, R.J., et al., *Solution chemistry of cubic and orthorhombic tricalcium aluminate hydration*. Cement and Concrete Research, 2017. **100**: p. 176-185.
94. Black, L., et al., *Hydration of tricalcium aluminate (C3A) in the presence and absence of gypsum—studied by Raman spectroscopy and X-ray diffraction*. Journal of Materials Chemistry, 2006. **16**(13): p. 1263-1272.
95. Collepardi, M., et al., *Retardation of Tricalcium Aluminate Hydration by Calcium Sulfate*. Journal of the American Ceramic Society, 1979. **62**(1-2): p. 33-35.
96. Geng, G., et al., *Synchrotron X-ray nanotomographic and spectromicroscopic study of the tricalcium aluminate hydration in the presence of gypsum*. Cement and Concrete Research, 2018. **111**: p. 130-137.
97. Minard, H., et al., *Mechanisms and parameters controlling the tricalcium aluminate reactivity in the presence of gypsum*. Cement and Concrete Research, 2007. **37**(10): p. 1418-1426.
98. Liu, X., et al., *The role of sulfate ions in tricalcium aluminate hydration: New insights*. Cement and Concrete Research, 2020. **130**: p. 105973.
99. Matschei, T., B. Lothenbach, and F.P. Glasser, *The role of calcium carbonate in cement hydration*. Cement and Concrete Research, 2007. **37**(4): p. 551-558.
100. Suraneni, P., et al., *New insights from reactivity testing of supplementary cementitious materials*. Cement and Concrete Composites, 2019. **103**: p. 331-338.
101. Snellings, R. and K.L. Scrivener, *Rapid screening tests for supplementary cementitious materials: past and future*. Materials and Structures, 2016. **49**: p. 3265–3279.
102. DIN EN 196-5, *Prüfverfahren für Zement - Teil 5: Prüfung der Puzzolanität von Puzzolanementen (Methods of testing cement – Part 5: Pozzolanicity test for pozzolanic cement)*. 2011, Beuth-Verlag: Berlin. p. 14.
103. Li, X., et al., *Reactivity tests for supplementary cementitious materials: RILEM TC 267-TRM phase 1*. Materials and Structures, 2018. **51**(6): p. 151.
104. Avet, F., et al., *Development of a new rapid, relevant and reliable (R^3) test method to evaluate the pozzolanic reactivity of calcined kaolinitic clays*. Cement and Concrete Research, 2016. **85**: p. 1-11.
105. Snellings, R., et al., *Rapid, Robust, and Relevant (R^3) Reactivity Test for Supplementary Cementitious Materials*. ACI Materials Journal, 2019. **116**(4): p. 155-162.
106. Suraneni, P. and J. Weiss, *Examining the pozzolanicity of supplementary cementitious materials using isothermal calorimetry and thermogravimetric analysis*. Cement and Concrete Composites, 2017. **83**: p. 273-278.
107. DIN EN 197-1, *Zement - Teil 1: Zusammensetzung, Anforderungen und Konformitätskriterien von Normalzement (Cement - Part 1: Composition, specifications and conformity criteria for common cements)*. 2011, Beuth-Verlag: Berlin, Germany. p. 8.
108. Schulze, S.E. and J. Rickert, *Pozzolanic Activity of Calcined Clays*, in *ACI SP 289 - 12th International Conference on Recent Advances in Concrete Technology and Sustainability Issues*, T.C. Holland, P.R. Gupta, and V.M. Malhotra, Editors. 2012, Sheridan Books: Prag. p. 277-288.

109. Buchwald, A., et al. *Untersuchung zur Reaktivität von Metakaolinen für die Verwendung in Bindemittelsystemen*. in *Gesellschaft Deutscher Chemiker e.V. - Jahrestagung*. 2003. Munich, Germany.
110. Zhang, Z., et al., *A new hydration kinetics model of composite cementitious materials, Part 2: Physical effect of SCMs*. *Journal of the American Ceramic Society*, 2020. **103**(6): p. 3880-3895.
111. Machner, A., et al., *Portland metakaolin cement containing dolomite or limestone – Similarities and differences in phase assemblage and compressive strength*. *Construction and Building Materials*, 2017. **157**(Supplement C): p. 214-225.
112. Lothenbach, B., K. Scrivener, and R.D. Hooton, *Supplementary cementitious materials*. *Cement and Concrete Research*, 2011. **41**(12): p. 1244-1256.
113. Oey, T., et al., *The Filler Effect: The Influence of Filler Content and Surface Area on Cementitious Reaction Rates*. *Journal of the American Ceramic Society*, 2013. **96**(6): p. 1978-1990.
114. Berodier, E. and K. Scrivener, *Understanding the Filler Effect on the Nucleation and Growth of C-S-H*. *Journal of the American Ceramic Society*, 2014. **97**(12): p. 3764-3773.
115. Bentz, D.P., et al., *Limestone and silica powder replacements for cement: Early-age performance*. *Cement and Concrete Composites*, 2017. **78**: p. 43-56.
116. Kumar, A., et al., *The filler effect: The influence of filler content and type on the hydration rate of tricalcium silicate*. *Journal of the American Ceramic Society*, 2017. **100**(7): p. 3316-3328.
117. Naber, C., et al., *The PONKCS method applied for time resolved XRD quantification of supplementary cementitious material reactivity in hydrating mixtures with ordinary Portland cement*. *Construction and Building Materials*, 2019. **214**: p. 449-457.
118. Beuntner, N. and K.-C. Thienel, *Pozzolan efficiency of calcined clays in blended cements with focus on the early hydration*. *Advances in Cement Research*, Ahead of print: p. 1-32.
119. Boháč, M., et al., *Investigation on early hydration of ternary Portland cement-blast-furnace slag–metakaolin blends*. *Construction and Building Materials*, 2014. **64**: p. 333-341.
120. Avet, F. and K. Scrivener, *Investigation of the calcined kaolinite content on the hydration of Limestone Calcined Clay Cement (LC³)*. *Cement and Concrete Research*, 2018. **107**: p. 124-135.
121. Zunino, F. and K. Scrivener, *The influence of the filler effect on the sulfate requirement of blended cements*. *Cement and Concrete Research*, 2019. **126**: p. 105918.
122. Quennoz, A. and K.L. Scrivener, *Interactions between alite and C₃A-gypsum hydrations in model cements*. *Cement and Concrete Research*, 2013. **44**: p. 46-54.
123. Bérodier, E.M.J., A.C.A. Muller, and K.L. Scrivener, *Effect of sulfate on C-S-H at early age*. *Cement and Concrete Research*, 2020. **138**: p. 106248.
124. Scherb, S., et al., *Reaction kinetics during early hydration of calcined phyllosilicates in clinker-free model systems*. *Cement and Concrete Research*, 2021. **143**: p. 106382.
125. Zunino, F. and K. Scrivener, *The reaction between metakaolin and limestone and its effect in porosity refinement and mechanical properties*. *Cement and Concrete Research*, 2021. **140**: p. 106307.
126. Poppe, L.J., et al., *A laboratory manual for X-ray powder diffraction*, in *Open-File Report*. 2001.
127. Scherb, S., et al., *Quantitative X-ray diffraction of free, not chemically bound water with the PONKCS method*. *Journal of Applied Crystallography*, 2018. **51**(6): p. 1535-1543.
128. Rietveld, H.M., *Line profiles of neutron powder-diffraction peaks for structure refinement*. *Acta Crystallographica*, 1967. **22**(1): p. 151-152.
129. O'Connor, B.H. and M.D. Raven, *Application of the Rietveld refinement procedure in assaying powdered mixtures*. *Powder Diffraction*, 1988. **3**: p. 2-6.

130. Jansen, D., et al., *A remastered external standard method applied to the quantification of early OPC hydration*. Cement and Concrete Research, 2011. **41**(6): p. 602-608.
131. Lothenbach, B., P. Durdziński, and K. De Weerd, *Thermogravimetric analysis*, in *A Practical Guide to Microstructural Analysis of Cementitious Materials*, K. Scrivener, R. Snellings, and B. Lothenbach, Editors. 2016, CRC Press. p. 177-212.
132. ASTM C1897 - 20, *Standard Test Methods for Measuring the Reactivity of Supplementary Cementitious Materials by Isothermal Calorimetry and Bound Water Measurements*. 2020, ASTM International: West Conshohocken, PA. p. 10.
133. DIN EN ISO 11885, *Water quality - Determination of selected elements by inductively coupled plasma optical emission spectrometry (ICP-OES)*. 2009, Beuth-Verlag: Berlin, Germany. p. 37.
134. ISO 13099-3, *Colloidal systems - Methods for zeta-potential determination - Part 3: Acoustic methods*. 2014, International Organization for Standardization: Geneva, Switzerland. p. 21.
135. Kulik, D.A., et al., *GEM-Selektor geochemical modeling package: revised algorithm and GEMS3K numerical kernel for coupled simulation codes*. Computational Geosciences, 2013. **17**(1): p. 1-24.
136. Lothenbach, B., et al., *Cemdata18: A chemical thermodynamic database for hydrated Portland cements and alkali-activated materials*. Cement and Concrete Research, 2019. **115**: p. 472-506.
137. Bich, C., J. Ambroise, and J. Péra, *Influence of degree of dehydroxylation on the pozzolanic activity of metakaolin*. Applied Clay Science, 2009. **44**(3-4): p. 194-200.
138. Tironi, A., et al., *Potential use of Argentine kaolinitic clays as pozzolanic material*. Applied Clay Science, 2014. **101**: p. 468-476.
139. Wojdyr, M., *Fityk: a general-purpose peak fitting program*. Journal of Applied Crystallography, 2010. **43**(5 Part 1): p. 1126-1128.
140. Ufer, K., et al., *Rietveld Refinement Of Disordered Illite-Smectite Mixed-Layer Structures By A Recursive Algorithm. I: One-Dimensional Patterns*. Clays and Clay Minerals, 2012. **60**(5): p. 507-534.
141. Maier, M., N. Beuntner, and K.-C. Thienel, *Mineralogical characterization and reactivity test of common clays suitable as supplementary cementitious material*. Applied Clay Science, 2021. **202**: p. 105990.
142. Avet, F., et al., *Report of RILEM TC 267-TRM phase 2: optimization and testing of the robustness of the R3 reactivity tests for supplementary cementitious materials*. Materials and Structures, 2022. **55**(3): p. 92.
143. Maier, M., et al., *Particle characteristics of calcined clays and limestone and their impact on the early hydration and sulfate demand of blended cement*. Cement and Concrete Research, 2022. **154**(106736): p. 15.
144. Maier, M., et al., *Hydration of cubic tricalcium aluminate in the presence of calcined clays*. Journal of the American Ceramic Society, 2021. **104**(7): p. 3619-3631.
145. Neißer-Deiters, A., et al., *Influence of the calcination temperature on the properties of a mica mineral as a suitability study for the use as SCM*. Applied Clay Science, 2019. **179**(105168).
146. Zunino, F. and K. Scrivener, *Factors influencing the sulfate balance in pure phase C₃S/C₃A systems*. Cement and Concrete Research, 2020. **133**: p. 106085.

8 Publications

8.1 Mineralogical characterization and reactivity test of common clays suitable as supplementary cementitious material

Reprint

Published in the Journal “Applied Clay Science”

Vol. 202, March 2021, p. 105990; doi: 10.1016/j.clay.2021.105990

Authors: M. Maier, N. Beuntner and K.-Ch. Thienel

Applied Clay Science 202 (2021) 105990



Contents lists available at ScienceDirect

Applied Clay Science

journal homepage: www.elsevier.com/locate/clay

Research Paper

Mineralogical characterization and reactivity test of common clays suitable as supplementary cementitious material

Matthias Maier^{*}, Nancy Beuntner, Karl-Christian Thienel

Institute for Construction Materials, University of the Bundeswehr Munich, Werner-Heisenberg-Weg 39, Neubiberg, 85579, Germany



ARTICLE INFO

Keywords:

Calcined clay
Common clays
Supplementary cementitious material
Pozzolanic reactivity
Rietveld refinement

ABSTRACT

The most abundant clays in the northern hemisphere are dominated by 2:1 clay minerals. However, compared to kaolinite-rich clays, these common clays have been less addressed by recent research on calcined clays. This study investigated 13 different clay-rich raw materials, focussing on available common clays from German deposits, with respect to their mineralogical composition and pozzolanic reactivity after calcination. It has been shown, that besides kaolinite content, for which X-ray diffraction (XRD) and thermogravimetry (TGA) yielded similar results, other parameters as type and quantity of 2:1 clay minerals and degree of kaolinite disorder must be considered in order to assess the potential of the raw materials. Therefore, structure models incorporating mixed layering and disorder were applied during raw clay quantification. Regarding the assessment of pozzolanic reactivity, the R^3 calorimetry test and solubility of silicon and aluminum ions in alkaline solution provided comparable results. In the range of kaolinite contents below 30 wt%, the influence of 2:1 clay minerals on the reactivity becomes significant, which makes a reliable quantification of illite, smectite or mixed layer minerals mandatory for the classification of common clays as raw materials for supplementary cementitious material (SCM).

1. Introduction

Unprocessed common clays (Murray, 2007) form the most promising raw material for the production of calcined clay as supplementary cementitious material (SCM) due to their widespread availability and economic benefit. Since kaolinite is proven to be the most reactive clay mineral after calcination (Fernandez et al., 2011; Hollanders et al., 2016), most of the recent studies investigated the influence of the amount and properties of kaolinite on the reactivity. Calcined kaolinite content was identified as the main factor for pozzolanic reactivity in calcined clays (Avet and Scrivener, 2018; Avet et al., 2016; Tironi et al., 2012). The relative order of reactivity of muscovite < illite < smectite < kaolinite is commonly stated in literature (Fernandez et al., 2011; Hollanders et al., 2016; Scherb et al., 2018; Schulze and Rickert, 2019). However, further authors have proven a significant influence provided by 2:1 clay minerals present as main components in clays on the reactivity and the type of hydration products (Alujas et al., 2015; Beuntner, 2019; Danner et al., 2019; Scherb et al., 2018). Especially in the northern hemisphere, the most abundant clay-sized mineral groups in the topsoil and subsoil belong to the illite/mica or smectite group,

whereas kaolinite group minerals are dominant south of the equator (Ito and Wagai, 2017). Bergaya and Lagaly (2013) classified the group of 'common clays' as one amongst four types of industrially applied clays, which "often contain illite-smectite mixed-layer minerals and are largely used for ceramics". In recent literature, these types of clays have also been referred to as 'illitic clay' or 'brick clay' (Dietel et al., 2017; Irassar et al., 2019; Msinjili et al., 2019). They make up about 90% of industrially used clay mineral-rich raw materials (Galán and Ferrell, 2013). Another promising group of materials in this context are secondary clay-bearing raw materials, as they accrue during industrial washing processes of sand (Maier et al., 2020), gravel or other mineral raw materials. In the light of a declining availability of traditional SCM (Schwarzkoopp et al., 2019) and the increasing substitution of cement clinker as a main approach to lower the ecological impact of the cement industry (Favier et al., 2019; Schneider, 2019; Scrivener et al., 2018), it would be negligent to disregard these groups of materials.

Common clays usually contain 2:1 and 1:1 clay minerals in varying proportions, as well as inplastic components. The most common 1:1 clay mineral, kaolinite, is built up by a tetrahedral and a octahedral sheet, which share a common plane of oxygen atoms and hydroxyls (Bookin

^{*} Corresponding author.

E-mail address: matthias.maier@unibw.de (M. Maier).

<https://doi.org/10.1016/j.clay.2021.105990>

Received 6 August 2020; Received in revised form 14 January 2021; Accepted 16 January 2021

Available online 27 January 2021

0169-1317/© 2021 Elsevier B.V. All rights reserved.

et al., 1989). Raw kaolinites usually possess a certain degree of disorder, due to faults in layer stacking (Brigatti et al., 2013; Ufer et al., 2015). There are different methodical approaches to characterize the degree of disorder in kaolinite using FTIR (Bich et al., 2009; Vaculíková et al., 2011) or XRD (Aparicio and Galan, 1999; Aparicio et al., 2006; Hinckley, 1963). These approaches become less reliable for clays with low kaolinite content due to overlapping of IR-bands and Bragg-reflections. There are however approaches, that consider stacking disorder during Rietveld refinement (Lorentz et al., 2018; Ufer et al., 2015). It is essential to include the degree of disorder into the characterization of the raw material, as this parameter influences the dehydroxylation behavior (Bich et al., 2009; Meinhold et al., 1992) as well as the pozzolanic reactivity after calcination (Hollanders et al., 2016; Tironi et al., 2014). Apart from this, regular structure models do not allow an adequate fit of the broad and asymmetric reflections resulting from the high degree of disorder (Lorentz et al., 2018) and thus may lead to incorrect quantifications.

The basic structures of the group of 2:1 phyllosilicates are extensively described e.g. by Brigatti et al. (2013) or Moore and Reynolds (1997). 2:1 clay minerals exist in different structures, with different chemical compositions, layer charges and degrees and types of disorder. They can be differentiated in swellable and non-swellable clay minerals and exist as alternating layers of two or more phyllosilicate endmembers (mixed-layer structures). While 1:1 clay minerals like kaolinite have one distinctive dehydroxylation temperature, the dehydroxylation process of 2:1 clay minerals is more complex and depends on the type of inter-layer cations as well as the octahedrally coordinated cations, which can cause differences in calcination temperature up to 200 K (Drits et al., 1995; Emmerich et al., 2009; Wolters and Emmerich, 2007). The reactivity of dehydroxylated 2:1 clay minerals results, similar as for 1:1 clay minerals, from a reduction in Al coordination from 6- to 5- and 4-fold (Danner et al., 2018; Garg and Skibsted, 2015), which was also observed for a common clay including kaolinite and 2:1 clay minerals (Dietel et al., 2017).

Especially strongly disordered 2:1 mixed layer clay minerals are difficult to quantify, thus their character and amount is often neglected or underestimated in studies of calcined clays. Nonetheless, pozzolanic reactivity of different 2:1 clay minerals has been proven by investigations on the pure minerals (He et al., 1995; Hollanders et al., 2016). Since minor components of common clays, especially carbonates, can significantly affect the reactivity (Danner et al., 2020; Zunino et al., 2020), further studies are needed to transfer these results to unprocessed common clays. Furthermore, there is a lack of data on the reactivity of clay mineral interstratifications present in common clays and their behavior in cementitious systems after calcination. Development of models for disordered mixed-layer structures (Ufer et al., 2012b) or description of highly disordered structures by the PONKCS method (Scarlett and Madsen, 2006; Taylor and Matulis, 1994) nowadays allow accurate determination of the content of disordered clay mineral interstratifications present in common clays using the Rietveld method (Ufer and Raven, 2017).

Most of aforementioned studies used one of the standardized methods for pozzolanic reactivity of SCM (Frattini test, Chapelle and modified Chapelle test), which however showed poor reproducibility in an interlaboratory round robin (Li et al., 2018) and neglect the contribution of reactive aluminum. A method, which considers aluminate and silicate reaction in clinker-free systems and allows isolating the SCM reaction from the clinker reaction with good interlaboratory reproducibility, is the R³-method (Avet et al., 2016; Li et al., 2018; Snellings et al., 2019). Avet et al. (2016) could prove a very good correlation between cumulative heat released at one day at 40 °C and relative strength after 28 and 90 days ($R^2 = 0.99$) in mortar, where 30% of cement was replaced by calcined clay. In order to evaluate the suitability of calcined clays or other aluminosilicates as precursor for geopolymer binders, several authors used the solubility of aluminum and silicon ions in alkaline solution as indicator for reactivity (Buchwald et al., 2009;

Dietel et al., 2017; Xu and Van Deventer, 2000). It turned out, that this parameter can also be used as sound criterion regarding the pozzolanic reactivity of calcined clays (Beuntner and Thienel, 2015).

As common clays will need to play a major role in the supply of alternative SCM in the near future, there is still lack of data, which links the mineralogy of the raw clays to their pozzolanic reactivity after calcination. The aim of the present study is a comparison of different methodical approaches for the characterization of raw material parameters of common clays, which affect pozzolanic reactivity on the one hand and for the evaluation of pozzolanic reactivity after calcination on the other. These data are important to evaluate the large deposits of common clays available for the production of eco-efficient SCM.

2. Materials and Methods

2.1. Selection of materials

Nine different common clays, two clay-rich industrial washing sludges and two processed high-grade kaolinitic clays were investigated in this study. The deposits are charted on the geological map of Germany (Toloczyki et al., 2006), which is supplemented by the layer “clay or claystone” from the maps of mineral resources of Germany (Dill and Röhling, 2007), in Fig. S1. All samples originate from German deposits. In order to transfer the results to similar deposits located elsewhere, information about the conditions of formation is given in Table 1. All samples were provided in quantities between 3 and 10 kg. The common clays were received as mined. The washing sludges were sampled after the filter presses and supplied in humid conditions. The processed kaolinitic clays were provided as dried granules.

The great variety of the selected clays is reflected in their chemical compositions, which are presented in Table 2. Except for KBZ and KK, where the data provided by the supplier were used, the composition was determined by ICP-OES (Varian ICP-OES 720 ES) on solutions of lithium metaborate flux fusions as described by Scherb et al. (2020).

2.1.1. Clay mineral analysis

Disaggregation of the clays was performed by agitation of the clay suspension for 10 min using an overhead stirrer in an ultrasonic bath. Sodium pyrophosphate served as dispersing agent. Particle-size separation of the <2 µm fraction was carried out subsequently by sedimentation in beakers according to Stoke's law. Oriented mounts of these

Table 1
Designation and short geological description of the investigated clays.

	Short name	Geological description
1	AC	Early Jurassic marine sediments (Kleeberg and Börner 2012)
2	OC	Mid-Jurassic (Dogger) shale formation formed as marine sediment (Thury 2002)
3	SCW	Tertiary weathering products of Devonian rocks deposited in Eo-until Miocene (Kleeberg and Börner 2012)
4	CCW	Secondary component of Upper Carboniferous coal beds (Meschede and Warr 2019)
5	KT	Primary kaolin deposit accrued by Eocene and Oligocene weathering of Devonian chlorite-rich shale (Elsner 2017)
6	KUP	Primary kaolin deposit formed from Eocene until Miocene by weathering of Carboniferous granite (Elsner 2017)
7	FUP	Miocene fireclays (Radczewski 1968)
8	RKUP	Secondary component of a Jurassic sandstone, enriched by technical wet-processing (Elsner 2017)
9	SW	Devonian slate which outcrops in Westerwald clay deposits (Meschede and Warr 2019)
10	SLS	Cretaceous shale (Kleeberg and Börner 2012)
11	MOSM	Upper Eocene to Upper Miocene sediments of the foreland basin (Meschede and Warr 2019)
12	KBZ	Tertiary kaolinization of a Permian quartz-porphyrity purified by wet-processing (Radczewski 1968)
13	KK	Weathering product of Triassic quartz and feldspar-rich sand (Elsner 2017)

Table 2
Chemical composition of the investigated raw clays in wt% (*provided by supplier).

	SiO ₂	Al ₂ O ₃	Fe ₂ O ₃	CaO	MgO	Na ₂ O	K ₂ O	TiO ₂	SO ₃	LOI
AC	51.1	17.6	6.4	5.4	2.3	0.3	2.1	0.9	1.9	12.1
OC	48.1	20.6	6.5	3.6	2.3	0.1	5.2	1.0	1.2	11.5
SCW	55.5	25.3	5.1	0.2	0.5	0.1	2.6	1.3	0.0	9.4
CCW	40.7	13.7	3.3	1.2	1.2	0.4	1.9	0.6	0.5	36.6
KT	66.0	18.1	6.2	0.1	0.4	0.3	2.7	1.0	0.0	5.2
KUP	67.1	17.8	3.9	0.0	1.0	0.1	3.4	1.0	0.0	5.8
FUP	55.7	26.4	3.9	0.2	0.3	0.1	0.6	1.1	0.0	11.8
RKUP	67.1	19.8	5.4	0.1	0.1	0.0	0.3	0.9	0.0	6.3
SW	64.3	16.9	7.2	0.1	2.1	0.2	2.7	0.9	0.0	5.6
SLS	65.3	16.9	6.2	0.2	0.6	0.1	4.1	0.9	0.0	5.7
MOSM	48.8	13.1	5.2	8.9	4.6	0.3	2.0	0.7	0.2	16.2
KBZ*	54.4	32.5	0.4	0.2	0.3	< 0.1	0.3	0.2	0.0	11.7
KK*	49.0	35.0	0.7	0.1	0.2	< 0.1	2.2	0.5	0.0	11.8

fractions were prepared by the glass slide method (Moore and Reynolds, 1997) and dried afterwards at 40 °C. The obtained texture specimens were analyzed both under air-dried condition and after ethylene glycol solvation. The latter was performed for at least 8 h at 60 °C in a desiccator. X-ray diffraction was performed in a PANalytical Empyrean diffractometer using Cu-K α -radiation (1.5406 Å) at 40 kV and 40 mA. The oriented mounts were measured on a spinning stage from 3 to 70°2 θ using a variable divergence slit, which kept the irradiated length at 15 mm, a nickel filter and a PIXcel^{1D} linear detector. Random powder mounts were prepared from the ground sample (5 min in a Retsch RS200 rotary disc mill) using a side-loading preparation tool. The measurements were carried out analogously to the oriented mounts but with fixed divergence slits (0.5°) and a Bragg-Brentano^{HD} monochromator instead of the nickel filter. Identification of the clay minerals on the one-dimensional diffractograms was carried out following Moore and Reynolds (1997). Further characterization of the illite-smectite (I–Sm) interstratifications was performed by one-dimensional fits of the air-dried (AD) and glycolated (EG) oriented mounts according to Ufer et al. (2012a) using Profex-BGMN (Bergmann et al., 1998; Doebelin and Kleeberg, 2015). The bulk mineralogy was calculated by Rietveld refinement of the patterns obtained from the random powder mounts of the bulk ground sample using I–Sm structure models from Ufer et al. (2012b). Models for stacking disordered kaolinite were applied according to Ufer et al. (2015). Amorphous content was calculated using the external standard approach (Jansen et al., 2012; O'Connor and Raven 1988). Zincite was used as standard material. The mass attenuation coefficients (MAC) of the clays were calculated based on their chemical composition using the MACs of the single elements provided in Arndt et al. (2006). The authors are aware that accuracy of the determination of amorphous content in complex mixtures with multiple phases can be strongly affected by microabsorption (Scarlett and Madsen 2018). Therefore, evidence for amorphous phase was carefully checked by all applied methods. When no significant amounts of amorphous content was identified (< 10 wt%), the phases were normalized to the sum of crystalline phases, as in traditional Rietveld quantification (Hill and Howard 1987). For a more detailed analysis of kaolinite state of order in the kaolinite-rich clays, the Aparicio-Galán-Ferrell index (AGFI) was calculated following the procedure of Aparicio et al. (2006). Peak deconvolution was performed between 19 and 26°2 θ by a least-squares fitting routine in the program Fityk (Wojdyr 2010), using symmetrical Pearson VII functions. Peak position, height, shape and half width at half maximum (HWHM) were refined after subtracting the background of the whole pattern. Qualitative phase analysis by interpretation of FTIR spectra was applied on the ground bulk samples in

order to verify the XRD results. FTIR-spectra were recorded at room temperature in attenuated total reflection (ATR) on a Nicolet iS10 FTIR spectrometer (ThermoFisher Scientific) equipped with a mid-infrared KBr beamsplitter, an EverGlo TM MIR radiation source (ν : = 15,798 cm⁻¹), a diamond ATR crystal and a dTGS detector. 16 scans at a resolution of 4 cm⁻¹ were collected between 400 and 4000 cm⁻¹. Degree of kaolinite disorder was determined for the kaolinite-rich clays based on the index P₀ according to Bich et al. (2009). The dehydroxylation properties were analyzed using TGA (Netzsch STA 449 F3 Jupiter) from room temperature to 900 °C, with a heating rate of 2 K/min. Data was processed with Origin 2018G. The kaolinite content in wt% (m_{Kao}) was determined according to Eq. 1 using the tangent method (Lothenbach et al. 2016; Taylor 1997):

$$m_{Kao} = m_{H_2O} \frac{M_{Kao}}{2M_{H_2O}} \quad (1)$$

where m_{H_2O} is the weight loss linked to the dehydroxylation of kaolinite determined by the tangent method, M_{Kao} is the molar mass of kaolinite (258.16 g/mol) and M_{H_2O} the molar mass of water (18.02 g/mol). The tangent method is supposed to minimize the influence of illite or muscovite on the quantification of kaolinite (Avet and Scrivener 2018), which should be validated in the course of this study by correlating it with the results obtained by Rietveld refinement.

2.1.2. Thermal treatment

Before thermal treatment, the raw clays were dried for at least 12 h at 105 °C, subsequently crushed in a laboratory jaw crusher and finally ground for 5 min in a rotary disc mill. Calcination was performed for 30 min in a preheated laboratory muffle furnace using 50 g of raw material in a platinum crucible. The calcination temperature was defined at 100 K above the endset temperature of the main dehydroxylation reaction determined by TGA, in order to ensure dehydroxylation of all clay minerals instead of solely kaolinite. The assessment of the pozzolanic reactivity afterwards should reveal, if this is a practical way to determine calcination temperature of clays dominated by 2:1 clay minerals. Mass loss during calcination was determined by weighing the sample before and after thermal treatment. After calcination, the materials were ground again for 10 min to disaggregate possibly sintered particles. The specific surface area (SSA) was measured with the BET method (DIN ISO 9277 2003) in a Horiba S-9601 MP using nitrogen as adsorption gas. Efficiency of calcination was checked by FTIR and considered as complete when no more OH-bands were detectable. Calcined kaolinite content (m_{CK}) was calculated according to Eq. 2.

$$m_{CK} = \frac{m_{Kao} - \frac{M_{Kao} \cdot m_{Kao}}{2M_{H_2O}}}{100 - LOC} \cdot 100 \quad (2)$$

where LOC is the mass loss during calcination and m_{Kao} the kaolinite content quantified by TGA (Eq. 1) and by Rietveld refinement, in order to compare both methods.

2.1.3. Reactivity tests

The release of aluminum (Al) and silicon (Si) ions in alkaline solution was determined by elution of the calcined material in 10% NaOH solution according to Buchwald et al. (2003). 1 g of sample was dispersed in 400 mL solution and shaken for 20 h in an interval agitator. After filtration the eluate was acidified to a pH of 1.0 using concentrated HCl and diluted with distilled water. Al and Si concentrations were measured using ICP-OES (Scherb et al. 2020). Heat release was investigated in the clinker-free R³ system at 40 °C following the procedure of Avet et al. (2016). This method was found to show very good correlation to strength development for a broad range of pozzolanic and hydraulic SCMs (Li et al. 2018; Snellings et al. 2019). 1.0 g of calcined clay was weighed together with 3.0 g of portlandite and 0.5 g of calcite, homogenized manually with a spatula and sealed in a plastic vial. 5.53 g of solution containing 4 g/L KOH and 20 g/L K₂SO₄ was weighed and sealed in a syringe. The materials were conditioned for at least 12 h in a drying cabinet at 40 °C. Powder and solution were mixed manually for 60 s using a spatula. About 3 g of paste was filled in HDPE ampoules and placed in a TAM Air isothermal calorimeter (TA instruments). 2 g of quartz sand mixed with 1 g of distilled water served as reference. The heat flow was recorded for 72 h and normalized to 1 g of calcined clay. The data was analyzed in Origin 2018G. Cumulative heat was determined by integrating the heat flow over time from 1.2 to 72 h and multiplying by 3.6 to receive the unit J/g. The first 1.2 h were not taken into account, as they are influenced by the difference between room and measuring temperature.

3. Results and discussion

3.1. Raw clay mineralogy

3.1.1. XRD

The basal reflections of the XRD patterns of the oriented mounts (Fig. 1) are used to identify the clay minerals. The shift of the (001)-reflections in the glycolated state allows the differentiation between swellable and non-swellable 2:1 clay minerals. This information is mandatory regarding the correct quantification of the samples.

OC and AC show a broad, asymmetric reflex with maximum intensity at a d-value of 9.9 Å in air-dried condition. The ethylene glycol intercalation causes a shift in the pattern of the illite-smectite interstratification. CCW only shows a marginal sharpening of the 10 Å reflection, which could indicate an illite with a small smectite component. The oriented patterns of KT, KUP and SW are nearly identical before and after glycol treatment, showing very sharp 10 Å reflections, which indicate highly crystalline mica with little or no illitic fraction. No shift but a small change in intensity and sharpness can be observed for SLS. The high width of the peak and the change of its shape after glycolation suggest an illite with minor amounts of expandable layers. MOSM yields the typical shift of the diffuse smectite (001)-reflections to higher d-values due to EG-intercalation together with a sharpening.

I—Sm interstratifications were identified in the clays OC, AC, SCW, CCW and SLS by one-dimensional fits of the preferred oriented

specimens. The selected models are used for Rietveld refinement of the random powder patterns, as it is shown exemplary for the clay “AC” in Fig. 2a. The kaolinite-rich clays showed kaolinite with different degree of stacking disorder. While the kaolinite pattern of sample “KK” can be fitted adequately with the ideal structure of Bish and Von Dreele (1989), disorder models of Ufer et al. (2015) or a combination of the ideal and disordered model has to be applied to model stacking faults in the other kaolinitic clays as shown in Fig. 2b. It is not clear if this coexistence of ordered and disordered kaolinite represents differently ordered domains or a physical mixture (Ufer et al. 2015). The quantitative composition of the raw clays derived by Rietveld refinement is given in Table 3.

3.1.2. FTIR

The IR spectra of clays can be subdivided into five regions (Kaufhold et al. 2012): the OH stretching region (3450–3750 cm⁻¹), the carbonate region (1360–1580 cm⁻¹), the SiO stretching region (975–1300 cm⁻¹), the OH deformation region (815–950 cm⁻¹) and the MeO deformation region (450–580 cm⁻¹). The absorption bands of the investigated raw clays in the OH stretching area are shown in Fig. 3a. Kaolinitic clays usually exhibit four more or less distinctive bands in this area, whose relative intensities are influenced by the degree of stacking disorder. While the band at 3620 cm⁻¹ represents the OH groups within the gibbsite layer, the bands at 3695, 3670 and 3650 cm⁻¹ characterize those at the boundary of the gibbsite layer, which connect to the silica layer via hydrogen bonds (Worrall 1986). The latter fact explains that those three bands are influenced by disturbance of the stacking order. The bands at 3650 cm⁻¹ and 3670 cm⁻¹ decrease or even disappear with increasing disorder, which is the case for SCW and FUP. The ratio of intensities between the 3620 cm⁻¹ and the 3695 cm⁻¹ band was used to calculate a disorder index, which is referred to as P₀ by Bich et al. (2009) for the clays with a kaolinite content of more than 40 wt%. Regarding the 2:1 clay minerals, smectite shows only one absorption band as there are only inner OH groups. In the case of MOSM, this band is located at 3620 cm⁻¹. This position is typical for smectites with a high aluminum substitution on the octahedral position (Farmer 1974) and not affected by the interlayer cations (Madejová 2003). According to Worrall (1986), the absorption band of trioctahedral mica is located at 3700 cm⁻¹ while dioctahedral micas exhibit OH stretching frequencies at 3620 cm⁻¹ which move to 3640 cm⁻¹ for interlayer deficient micas (illites). The kaolinite-bearing clays exhibit the typical Si—O stretching vibrations of kaolinite (Madejová 2003) in the grey-marked area at about 990, 1025 and 1113 cm⁻¹ (see Fig. 3b). These occur recognizably for the investigated clays with a kaolinite content determined by XRD of 20 wt% and more (see Table 3) but are only pronounced for the clays KK, KBZ, FUP and RKUP. The clays rich in 2:1 clay minerals in contrast reveal one broad band attributed to Si—O stretching vibrations in the range around 1000 cm⁻¹. The Al—OH bending band at 910 cm⁻¹ is distinctive for all kaolinite-bearing clays, however, it could also represent OH deformation vibrations in smectite as it is present in SW, MOSM and SLS. The band at around 930 cm⁻¹ is therefore more representative for kaolinite but only pronounced in the kaolinite-rich clays (KK, KBZ, FUP, RKUP). The band at 830 cm⁻¹ represents Al—O stretching attributed to the tetrahedral Al (Janek et al. 2009) and is therefore only present in the clays that contain muscovite or illite. The presence of carbonates in MOSM, AC and to a small extend in OC can be verified by the band at 875 cm⁻¹, which represents the out-of-plane bending mode of the CO₃ anion (Madejová et al. 2010). The observed bands are consistent with the results obtained by Rietveld refinement (Table 3).

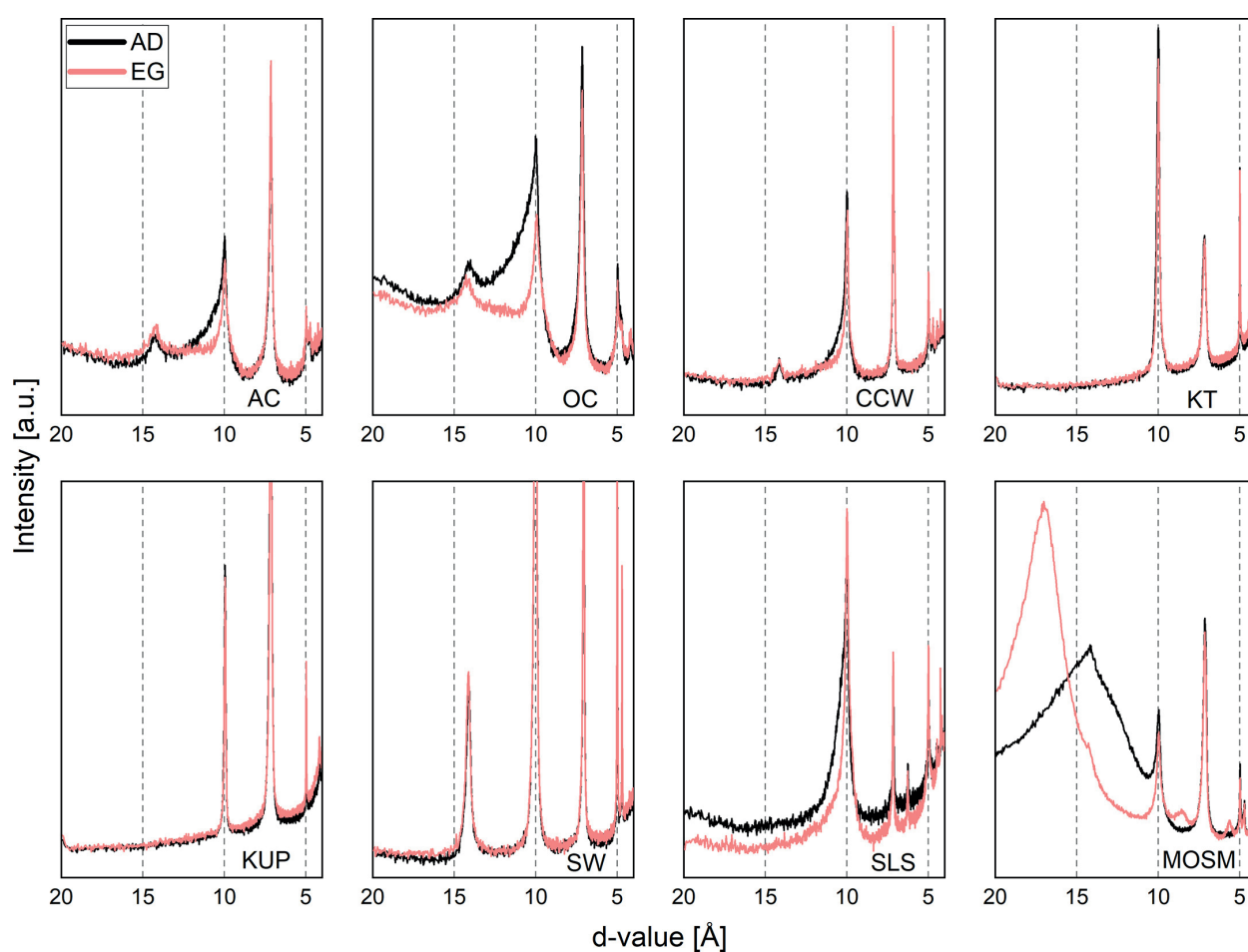


Fig. 1. Diffractograms from 4 to 20°2 θ of air dried (AD) and glycolated (EG) oriented mounts of the clays with low kaolinite content.

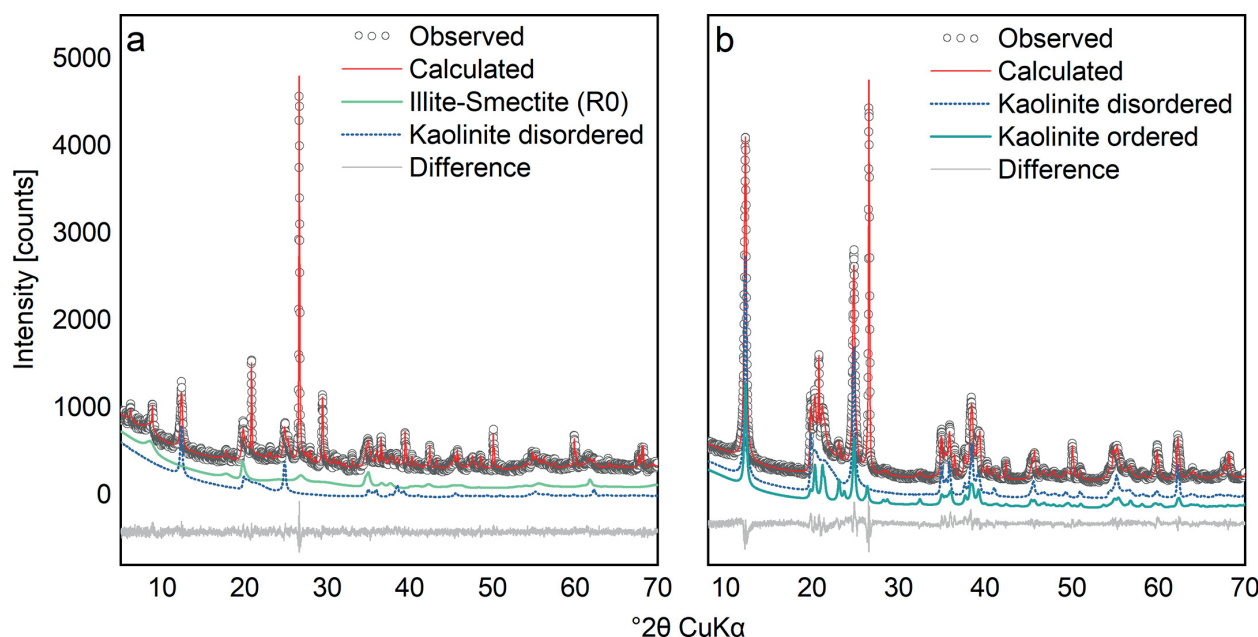


Fig. 2. Rietveld refinement of a) “AC” with calculated patterns for illite-smectite (R0) and disordered kaolinite ($R_{wp} = 5.45\%$; $R_{exp} = 4.68\%$) and b) “KBZ” with calculated patterns of ordered and disordered kaolinite ($R_{wp} = 8.71\%$; $R_{exp} = 5.95\%$).

3.2. Determination of (calcined) kaolinite content

Completeness of dehydroxylation was verified using FTIR spectroscopy once more on the samples after calcination. The spectra in the OH-stretching region after calcination (Fig. 4a) shows, that all clays are dehydroxylated completely as no more OH bands are visible. Beyond that, the distinct Si—O stretching bands merge to one single band due to loss of long range order. Therefore, in the following considerations, a complete conversion of the kaolinite in the samples can be assumed.

The kaolinite content in the raw clay and the calcined kaolinite content in the calcined clay was determined by TGA using the tangent method and XRD using Rietveld refinement. Both methods provide similar results for the most part (see Table 4). There is no systematic deviation between the observed and theoretical data. Comparable consistency was obtained by Lorentz et al. (2018), who however used a different approach during Rietveld refinement. Scrivener et al. (2019) observed significant differences between the two methods and led it back to errors in XRD attributed to preferred orientation and disorder. While results of Rietveld refinement are sensitive to the correct identification of all components, use of adequate structure models and appropriate sample preparation (Ufer and Raven 2017), TGA-results can be strongly distorted by accompanying clay minerals which dehydroxylate in the same temperature range, e.g. smectites, or organic components. They can further be user- or software-dependent regarding the definition of on- and endset points of the reaction and the determination of the tangent. In the case of one clay with high organic content (CCW), the determination of kaolinite content using TGA was not possible,

which is why this clay is not considered in Table 4. Therefore, the values determined using XRD were chosen for the presentation of the correlations in 3.4.

3.3. Comparison of methods for reactivity testing

The reactivity of the calcined clays was assessed by two different methods as described in 2.2.3. There is a very good linear correlation between the solubility of Si and Al ions and the evolved heat after 72 h during R^3 calorimetry test (see Fig. 5 and Table 5). Beuntner et al. (2019) reported high correlations between soluble Si and Al ions and the 28 days strength activity index and made use of the method to evaluate the optimum calcination temperature. Avet et al. (2016) proved a linear correlation between released heat during R^3 calorimetry test and compressive strengths for all ages. The results obtained here are therefore not surprising but confirm once more the important role of soluble Si as well as Al ions in the reactivity of calcined clays and emphasize their chemical contribution during hydration. It can furthermore be concluded that similar criteria can be used to assess calcined clays regarding the use as SCM or as precursor for alkali activated binders.

3.4. Mineralogical parameters influencing reactivity

Table 5 summarizes the determined parameters, which are used for the correlations hereafter.

Avet et al. (2016) identified the calcined kaolinite content as the decisive factor determining pozzolanic reactivity for clays. The results

Table 3

Mineralogical composition of the investigated clays in wt% (Qtz = quartz, Kaol = kaolinite, I-Sm = illite-smectite interstratification, Sm = smectite, Ms/I = muscovite/illite, Chl = chlorite, Cc = calcite, Dol = dolomite, Fsp = feldspar, Rt/An = rutile/anatase, Py = pyrite, He = hematite, Goe = goethite, Gy = gypsum, Am = amorphous).

	AC	OC	SCW	CCW	KT	KUP	FUP	RKUP	SW	SLS	MOSM	KBZ	KK
Qtz	20.0	21.5	18.4	15.8	37.9	33.2	12.6	47.7	22.8	37.3	18.2	15.5	4.0
Kaol	22.6	19.7	40.0	10.4	20.0	25.7	70.6	45.0	–	6.8	8.0	83.9	78.2
I-Sm	31.8	37.8	19.8	23.5	–	–	–	–	–	40.0	–	–	–
Sm	–	–	–	–	–	–	–	–	–	–	24.8	–	–
Ms/I	4.7	5.7	17.7	11.3	36.1	36.1	12.9	3.1	55.3	15.2	18.9	–	8.0
Chl	5.6	2.4	–	1.4	–	–	–	–	20.4	–	4.9	–	–
Cc	7.4	2.4	–	0.4	–	–	–	–	–	–	6.8	–	–
Dol/Ank	1.1	2.1	–	0.7	–	–	–	–	–	–	10.3	–	–
Fsp	3.8	4.7	–	–	–	–	1.2	–	–	–	7.2	–	8.9
Rt/An	2.2	2.1	1.5	0.3	1.3	0.7	2.7	0.4	1.6	0.7	0.8	0.7	0.8
Py	0.9	–	–	–	–	–	–	–	–	–	–	–	–
He	–	–	1.7	0.3	–	–	–	0.4	–	–	–	–	–
Sid	–	–	–	0.8	–	–	–	–	–	–	–	–	–
Goe	–	–	1.0	–	4.8	4.3	–	3.3	–	–	–	–	–
Gy	–	1.7	–	–	–	–	–	–	–	–	–	–	–
Am	*	*	*	35.0	*	*	*	*	*	*	*	*	*

* Clays with no significant amorphous content were normalized to their crystalline compounds.

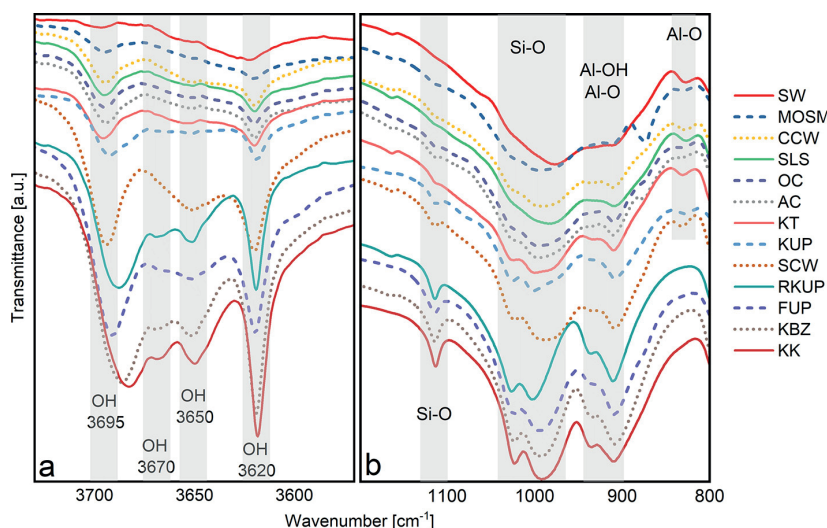


Fig. 3. FTIR spectra of the raw clays in the OH (a) and SiO/Al-OH stretching region (b).

obtained here can largely support these findings as shown in Fig. 6.

There is, however, a difference between the influence of the overall reactivity defined by the evolved heat after a specific time and the reaction kinetics, reflected by the time of the maximum heat flow. Regarding the five investigated clays with a minimum kaolinite content of 40 wt% in the raw clay (SCW, RKUP, FUP, KBZ & KK), the evolved heat after 72 h is dominantly defined by the kaolinite content whereas the heat flow maximum is shifted significantly to later times with increasing degree of order. This is displayed in Table 6, where the relation between the degree of kaolinite disorder and the maximum heat flow during R^3 calorimetry test is presented. The indexes were not determined for the clays with a kaolinite content below 40 wt%, as in these cases strong overlapping of OH bands (FTIR) and Bragg reflections (XRD) occur. Furthermore, the influence of disorder phenomena in kaolinite on the reaction behavior decreases with lower kaolinite contents.

As already described by Galan et al. (1998), strongly disordered kaolinites tend to have a higher SSA than well-ordered kaolinites, which is still true for the SSA after calcination, as confirmed in Table 6. The

data presented here do not allow to draw conclusions on which of the two linked parameters - the high SSA or the structural defects - is the driving force for the faster reactivity. While the weight fraction of ordered kaolinite determined by Rietveld refinement and the AGFI give a good linear correlation with the heat flow maximum, the P_0 -index yields poorer correlation. The poor correlation of P_0 is mainly due to the value calculated for RKUP. It would need an additional number of kaolinitic clays to be investigated with the used methods in order to evaluate the parameters, which influence the correct determination of P_0 . Lorentz et al. (2018) neither found any good agreement between crystallinity indexes based on FTIR and XRD. The peak deconvolution for the calculation of the AGFI, which is illustrated in Fig. 7, allows a more precise analysis than the FTIR method, where overlapping of OH-bands can also occur. Aparicio et al. (2006) already stated that the AGFI index is less sensitive to the presence of other phases.

The fact that the degree of disorder determined by XRD as well as the SSA correlate well with the reaction rate (see Table 6) therefore suggests using XRD over FTIR for the determination of this parameter. The influence of the degree of kaolinite disorder derived by FTIR on the

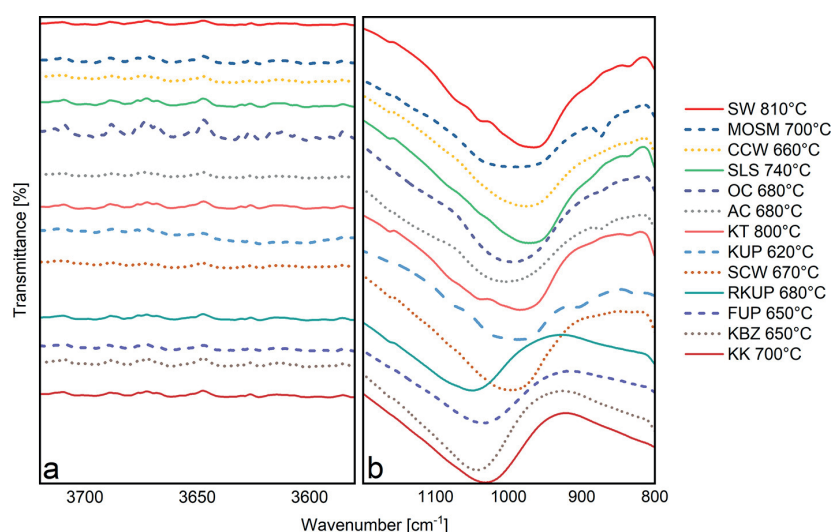


Fig. 4. FTIR spectra of the calcined clays in the OH (a) and SiO/Al-OH stretching region (b).

Table 4

Comparison of (calcined) kaolinite content in wt% determined by TGA (tangent method) and XRD (Rietveld refinement).

	Kaolinite Rietveld	Kaolinite TGA	Calcined kaolinite Rietveld	Calcined kaolinite TGA
SW (810 °C)	–	–	–	–
SLS (800 °C)	6.8	11.1	6.2	10.1
MOSM (700 °C)	8.0	8.1	7.5	7.6
CCW (660 °C)	10.4	n.d.	13.9	n.d.
OC (800 °C)	19.7	19.5	18.8	18.6
KT (800 °C)	20.0	20.1	18.1	18.2
AC (680 °C)	22.6	23.7	21.4	22.5
KUP (800 °C)	25.7	18.2	23.2	16.4
SCW (800 °C)	40.0	43.3	37.8	40.9
RKUP (680 °C)	45.0	38.0	41.3	34.8
FUP (650 °C)	70.6	60.8	68.6	59.1
KK (700 °C)	78.4	79.0	76.3	76.9
KBZ (650 °C)	83.9	79.0	81.5	76.7

pozzolanic reactivity of kaolinitic clays has already been verified by Tironi et al. (2012). The data provided here suggest, that the degree of disorder mainly affects the reaction kinetics but not the overall evolved heat. This is most evident for the samples KK (AGFI = 1.35) and KBZ (AGFI = 0.85), which have a comparable kaolinite content (≈ 80 wt%) and overall heat development (750–780 J/g) but significantly different reaction kinetics (Heat flow maximum KK after 15.6 h and KBZ after 7.9 h). These findings are in line with Hollanders et al. (2016), who observed a more rapid portlandite consumption of low ordered kaolinite than of high ordered kaolinite. Looking at the bottom left corner of the diagram in Fig. 6, there are, despite the good correlation over the whole diagram, significant differences for clays with similar kaolinite content.

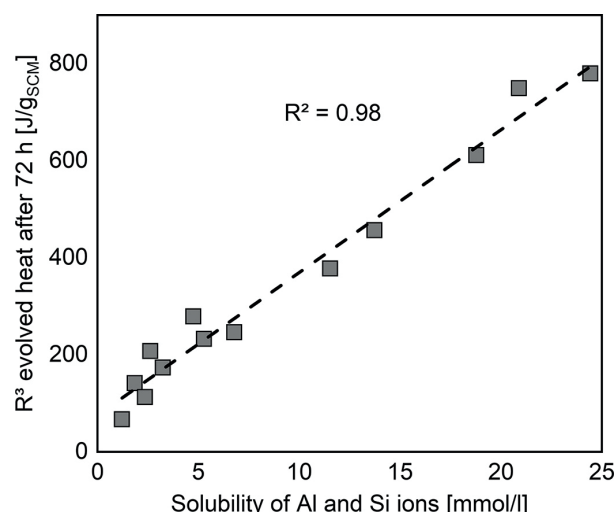


Fig. 5. Correlation between solubility of Al and Si ions and evolved heat during R³ calorimetry test after 72 h.

This becomes more obvious in Table 7, where the reactivity based on the R³ test is presented for the clays with a kaolinite content below 30 wt%. The samples KT and KUP, which only have muscovite and quartz as other main constituents, show significantly lower reactivity than the samples with similar calcined kaolinite content but reactive 2:1 clay minerals (I–Sm, Sm) as main constituents. This fact confirms that for the evaluation of many common clays a determination of the kaolinite content is not sufficient regarding the assessment of reactivity. Furthermore, it proves that the applied method for defining the calcination temperature was suitable to ensure at least partly activation of the 2:1 clay minerals. Even though, the major part of the investigated common clays provides lower reactivity than the typical low grade kaolinitic clays investigated in LC³ blends, the 3 days evolved heat is still located within the range of established SCM between fly ash and slag (Li et al. 2018). Furthermore, recent research has shown, that these types of clays can show benefits in comparison to kaolinite-rich clays regarding rheological behavior (Sposito et al. 2020) and durability issues like

Table 5

Calcined kaolinite content based on XRD, SSA, amount of Si and Al ions dissolved in 10% NaOH-solution, evolved heat during R³ calorimetry test (72 h) for all calcined clays and kaolinite disorder indexes for the kaolinite-rich raw clays.

	AC	OC	SCW	CCW	KT	KUP	FUP	RKUP	SW	SLS	MOSM	KBZ	KK
m _{CK} [wt%]	21.4	18.8	37.8	13.9	18.1	23.2	68.6	41.3	0.0	6.2	7.5	81.5	76.3
Al sol. [mmol/L]	2.0	2.1	4.7	1.1	1.4	2.8	7.8	6.9	0.5	0.9	0.5	11.3	9.6
Si sol. [mmol/L]	2.8	3.2	6.9	1.6	1.9	4.0	11.0	6.9	0.8	1.4	1.3	13.2	11.3
R ³ [J/g]	279	233	399	208	174	246	611	457	67	113	141	780	749

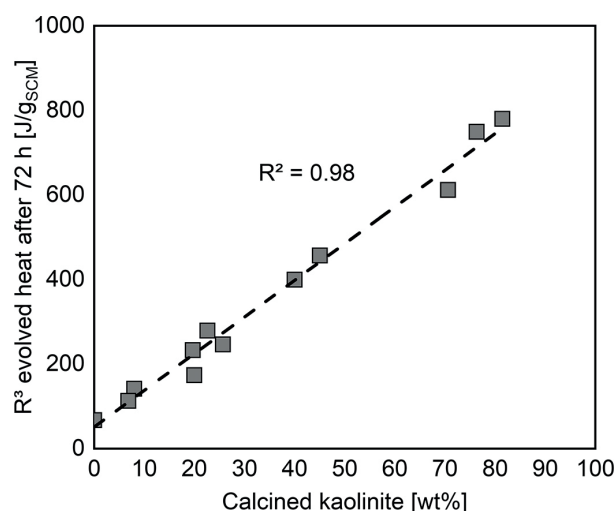


Fig. 6. Correlation between calcined kaolinite content and R³ evolved heat after 72 h.

Table 6

Relation between kaolinite disorder determined by different methods or respectively SSA and heat flow maximum during R³ calorimetry test for the clays with a kaolinite content of more than 40 wt% in the raw clay.

	wt. fraction ordered [–]	AGFI [–]	P ₀ [–]	SSA [m ² /g]	Heat flow maximum [h]
FUP	0.00	0.54	0.92	44.1	5.9
SCW	0.00	0.39	0.97	32.2	6.1
KBZ	0.30	0.85	1.14	20.4	7.9
RKUP	0.38	1.24	0.96	8.4	13.6
KK	1.00	1.35	1.29	11.3	15.6

carbonation (Beuntner et al. 2019; Trümer et al. 2019).

4. Conclusion

This study investigated 13 different clay-rich raw materials from German deposits regarding their mineralogical composition and pozzolanic reactivity after calcination. Even though there is an overall good correlation between calcined kaolinite content and reactivity based on the R³ calorimetry test, the influence of illite-smectite interstratifications and smectites becomes significant for common clays with a kaolinite content below 30 wt%, when calcined 100 K above the endset temperature of their main dehydroxylation peak. A qualitative assessment of the contribution of 2:1 clay minerals to the reactivity of calcined common clays can be made without separating the single phases, if an elaborate mineralogical analysis is conducted. Unprocessed common clays - dependent on their mineralogical composition - provide reactivity comparable to established supplementary cementitious material (SCM) like fly ash or slag. For the assessment of pozzolanic reactivity, the R³ calorimetry test and the solubility of Al and Si ions exhibit

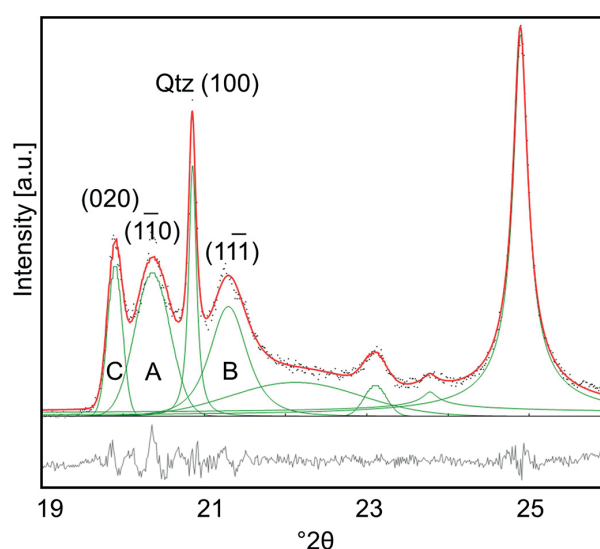


Fig. 7. Peak deconvolution for the calculation of AGFI (example of KBZ)

Table 7

R³ evolved heat of calcined clays with low calcined kaolinite content.

	SW	SLS	MOSM	CCW	OC	KT	AC	KUP
Calcined kaolinite [wt%]	0	6.8	8.0	16.0	19.7	20.0	22.6	25.7
R ³ evolved heat after 72 h [J/gSCM]	67	113	141	208	233	174	279	246

very good consistency. Five of the nine investigated raw clays contain significant amounts of illite-smectite interstratifications, as it is typical for common clays. Regarding their widespread availability, these clays should move further into the focus of research in the search for alternative SCM. Especially regarding clays with low kaolinite content, a comprehensive mineralogical characterization is mandatory in order to assess their potential as SCM. Rietveld refinement and thermal analysis yield similar results with regard to kaolinite content. The former, however, provides additional important information as degree of kaolinite disorder. Latter parameter correlates with the specific surface area (SSA) and significantly influences the reaction kinetics of kaolinite dominated clays.

Declaration of Competing Interest

None.

Acknowledgements

This research did not receive any specific grant from funding

agencies in the public, commercial, or not-for-profit sectors. The authors would like to thank Strobel Quarzsand GmbH, Quarzwerke GmbH, Goerg & Schneider GmbH & Co KG, Hubert Gerharz Tonbergbau GmbH, Liapor GmbH & Co. KG and Schlagmann Poroton GmbH & Co. KG for providing the raw clays.

References

- Alujas, A., Fernández, R., Quintana, R., Scrivener, K.L., Martirena, F., 2015. Pozzolanic reactivity of low grade kaolinitic clays: influence of calcination temperature and impact of calcination products on OPC hydration. *Appl. Clay Sci.* 108, 94–101.
- Aparicio, P., Galán, E., 1999. Mineralogical interference on kaolinite crystallinity index measurements. *Clay Clay Miner.* 47, 12–27.
- Aparicio, P., Galán, E., Ferrell, R., 2006. A new kaolinite order index based on XRD profile fitting. *Clay Miner.* 41, 811–817.
- Arndt, U.W., Creagh, D.C., Deslattes, R.D., Hubbel, J.H., Indelicato, P., Kessler JR, E.G., Lindroth, E., 2006. *Production and Properties of Radiation*, Table 4.2.4.3. *Mass attenuation coefficients (cm²g⁻¹)*. Springer Verlag.
- Avet, F., Scrivener, K., 2018. Investigation of the calcined kaolinite content on the hydration of Limestone Calcined Clay Cement (LC³). *Cement Concrete Res* 107, 124–135.
- Avet, F., Snellings, R., Alujas Diaz, A., Ben Haha, M., Scrivener, K., 2016. Development of a new rapid, relevant and reliable (R³) test method to evaluate the pozzolanic reactivity of calcined kaolinitic clays. *Cement Concrete Res* 85, 1–11.
- Bergaya, F., Lagaly, G., 2013. Chapter 1 - Introduction to Clay Science: Techniques and applications. In: Lagaly, G. (Ed.), Bergaya, F. Elsevier, Developments in Clay Science, pp. 1–7.
- Bergmann, J., Friedel, P., Kleeberg, R., 1998. BGMN – a new fundamental parameter based Rietveld program for laboratory X-ray sources, its use in quantitative analysis and structure investigations. *Commission on Powder Diffraction Newsletter* 20, 5–8.
- Beuntner, N., 2019. Zur Eignung und Wirkungsweise calcinierter Tone als reaktive Bindemittelkomponente in Zement. Beuth Verlag, Berlin.
- Beuntner, N., Thienel, K.-C., 2015. Properties of Calcined Lias Delta Clay - Technological Effects, Physical Characteristics and Reactivity in Cement. In: Scrivener, K., Favier, A. (Eds.), *Calcined Clays for Sustainable Concrete - Proceedings of the 1st International Conference on Calcined Clays for Sustainable Concrete*. Springer Netherlands, Lausanne, Switzerland, pp. 43–50.
- Beuntner, N., Sposito, R., Thienel, K.-C., 2019. Potential of Calcined Mixed-Layer Clays as Pozzolans in Concrete. *ACI Mater. J.* 116, 19–29.
- Bich, C., Ambroise, J., Péra, J., 2009. Influence of degree of dehydroxylation on the pozzolanic activity of metakaolin. *Appl. Clay Sci.* 44, 194–200.
- Bish, D.L., Von Dreele, R.B., 1989. Rietveld Refinement of Non-Hydrogen Atomic Positions in Kaolinite. *Clay Clay Miner.* 37, 289–296.
- Bookin, A.S., Drits, V.A., Planchon, A., Tchoubar, C., 1989. Stacking Faults in Kaolin-Group Minerals in the Light of Real Structural Features. *Clay Clay Miner.* 37, 297–307.
- Brigatti, M., Galán, E., Theng, B., 2013. Structures and Mineralogy of Clay Minerals. In: Bergaya, F., Theng, B.K.G., Lagaly, G. (Eds.), *Developments in Clay Science*. Elsevier, Amsterdam, pp. 21–81.
- Buchwald, A., Kriegel, R., Kaps, C., Zellmann, H.-D., 2003. Untersuchung zur Reaktivität von Metakaolinen für die Verwendung in Bindemittelsystemen. Gesellschaft Deutscher Chemiker e.V. Jahrestagung, Munich, Germany.
- Buchwald, A., Hohmann, M., Posern, K., Brendler, E., 2009. The suitability of thermally activated illite/smectite clay as raw material for geopolymer binders. *Appl. Clay Sci.* 46, 300–304.
- Danner, T., Norden, G., Justnes, H., 2018. Characterisation of calcined raw clays suitable as supplementary cementitious materials. *Appl. Clay Sci.* 162, 391–402.
- Danner, T., Norden, G., Justnes, H., 2019. Calcareous smectite clay as a pozzolanic alternative to kaolin. *Eur. J. Environ. Civ. Eng.* 1–18.
- Danner, T., Norden, G., Justnes, H., 2020. The effect of Calcite in the Raw Clay on the Pozzolanic activity of Calcined Illite and Smectite. In: Bishnoi, S. (Ed.), *Calcined Clays for Sustainable Concrete*. Springer, Singapore, pp. 131–138.
- Dietel, J., Warr, L.N., Bertmer, M., Steudel, A., Grathoff, G.H., Emmerich, K., 2017. The importance of specific surface area in the geopolymerization of heated illitic clay. *Appl. Clay Sci.* 139, 99–107.
- Dill, H.G., Röhling, S., 2007. *Map of Mineral Resources of Germany 1: 1 000 000 (BSK1000)*, in: BGR (Ed.), Hannover.
- DIN ISO 9277, 2003. Determination of the Specific Surface Area of Solids by Gas Adsorption - BET Method. Beuth-Verlag, Berlin, p. 19.
- Doebelin, N., Kleeberg, R., 2015. Profex: a graphical user interface for the Rietveld refinement program BGMN. *J. Appl. Crystallogr.* 48, 1573–1580.
- Drits, V.A., Besson, G., Muller, F., 1995. An improved Model for Structural Transformations of Heat-Treated Aluminous Dioctahedral 2:1 Layer Silicates. *Clay Clay Miner.* 43, 718–731.
- Elsner, H., 2017. *Kaolin in Deutschland*, in: Rohstoffe, B.-B.f.G.u. (Ed.), Hannover.
- Emmerich, K., Wolters, F., Kahr, G., Lagaly, G., 2009. Clay profiling: the classification of montmorillonites. *Clay Clay Miner.* 57, 104–114.
- Farmer, V.C., 1974. *The Layer Silicates*, in: Farmer, V.C. (Ed.), *The Infrared Spectra of Minerals*. Mineralogical Society of Great Britain and Ireland, p. 0.
- Favier, A., Scrivener, K., Habert, G., 2019. Decarbonizing the Cement and Concrete Sector: Integration of the Full Value Chain to Reach Net Zero Emissions in Europe, SBE19 Brussels - BAMB-CIRCPATH "Buildings as Material Banks - a Pathway for a Circular Future". IOP Publishing, Brussels, Belgium, p. 012009.
- Fernandez, R., Martirena, F., Scrivener, K.L., 2011. The origin of the pozzolanic activity of calcined clay minerals: a comparison between kaolinite, illite and montmorillonite. *Cement Concrete Res* 41, 113–122.
- Galán, E., Ferrell, R.E., 2013. Chapter 3 - Genesis of Clay Minerals. In: Lagaly, G. (Ed.), Bergaya, F. Elsevier, *Developments in Clay Science*, pp. 83–126.
- Galan, E., Aparicio, P., Gonzalez, I., Miras, A., 1998. Contribution of multivariate analysis to the correlation of some properties of kaolin with its mineralogical and chemical composition. *Clay Miner.* 33, 65–75.
- Garg, N., Skibsted, J., 2015. Heated Montmorillonite: Structure, Reactivity, and Dissolution. In: Scrivener, K., Favier, A. (Eds.), *1st International Conference on Calcined Clays for Sustainable Concrete*. Springer Netherlands, Lausanne, pp. 117–124.
- He, C., Osbaeck, B., Makovsky, E., 1995. Pozzolanic reactions of six principal clay minerals: activation, reactivity assessments and technological effects. *Cement Concrete Res* 25, 1691–1702.
- Hill, R.J., Howard, C.J., 1987. Quantitative phase analysis from neutron powder diffraction data using the Rietveld method. *J. Appl. Crystallogr.* 20, 467–474.
- Hinckley, D.N., 1963. Variability in "crystallinity" values among the kaolin deposits of the coastal plain of Georgia and South Carolina. *Clay Clay Miner.* 11, 229–235.
- Hollanders, S., Adriaens, R., Skibsted, J., Cizer, Ö., Elsen, J., 2016. Pozzolanic reactivity of pure calcined clays. *Appl. Clay Sci.* 132–133, 552–560.
- Irassar, E.F., Cordoba, G., Zito, S.V., Rossetti, A., Rahhal, V.F., Dario, F., 2019. Durability of blended cements containing illitic calcined clays. In: Gemrich, J. (Ed.), *15th International Congress on the Chemistry of Cement*. Prague, Czech Republic, Research Institute of Binding Materials Prague, p. 11.
- Ito, A., Wagai, R., 2017. Global distribution of clay-size minerals on land surface for biogeochemical and climatological studies. *Scientific Data* 4, 170103.
- Janek, M., Bugár, I., Lorenc, D., Szöcs, V., Velić, D., Chorvát, D., 2009. Terahertz time-domain spectroscopy of selected layered silicates. *Clay Clay Miner.* 57, 416–424.
- Jansen, D., Stabler, C., Goetz-Neunhoeffer, F., Dittich, S., Neubauer, J., 2012. Does ordinary Portland Cement contain amorphous phase? A quantitative study using an external standard method. *Powder Diffract.* 26, 31–38.
- Kaufhold, S., Hein, M., Dohrmann, R., Ufer, K., 2012. Quantification of the mineralogical composition of clays using FTIR spectroscopy. *Vib. Spectrosc.* 59, 29–39.
- Kleeberg, K., Börner, A., 2012. *Tone und tonige Gesteine, Steine- und Erden-Rohstoffe in der Bundesrepublik Deutschland*, Heft SD 10 ed. Schweizerbart, Stuttgart, pp. 51–84.
- Li, X., Snellings, R., Antoni, M., Alderete, N.M., Ben Haha, M., Bishnoi, S., Cizer, Ö., Cyr, M., De Weerd, K., Dhandapani, Y., Duchesne, J., Haufe, J., Hooton, D., Juenger, M., Kamali-Bernard, S., Kramar, S., Marroccoli, M., Joseph, A.M., Parashar, A., Patapy, C., Provis, J.L., Sabio, S., Santhanam, M., Steger, L., Sui, T., Telesca, A., Vollpracht, A., Vargas, F., Walkley, B., Winnefeld, F., Ye, G., Zajac, M., Zhang, S., Scrivener, K.L., 2018. Reactivity tests for supplementary cementitious materials: RILEM TC 267-TRM phase 1. *Mater. Struct.* 51, 151.
- Lorentz, B., Shanahan, N., Stetsko, Y.P., Zayed, A., 2018. Characterization of Florida kaolin clays using multiple-technique approach. *Appl. Clay Sci.* 161, 326–333.
- Lothenbach, B., Durdziński, P., De Weerd, K., 2016. Thermogravimetric analysis. In: Snellings, R., Lothenbach, B. (Eds.), *Scrivener, K. CRC Press, A Practical Guide to Microstructural Analysis of Cementitious Materials*, pp. 177–212.
- Madejová, J., 2003. FTIR techniques in clay mineral studies. *Vib. Spectrosc.* 31, 1–10.
- Madejová, J., Balan, E., Petit, S., 2010. Application of Vibrational Spectroscopy to the Characterization of Phyllosilicates and other Industrial Minerals. *Advances in the characterization of industrial minerals*, pp. 171–226.
- Maier, M., Forster, B., Beuntner, N., Thienel, K.-C., 2020. Potential of a calcined recycling kaolin from silica sand processing as supplementary cementitious material. In: Bishnoi, S. (Ed.), *Calcined Clays for Sustainable Concrete*. Springer, Singapore, pp. 75–83.
- Meinhold, R.H., Atakul, H., Davies, T.W., Slade, R.C.T., 1992. Flash calcination of kaolinite studied by DSC, TG and MAS NMR. *J. Therm. Anal.* 38, 2053–2065.
- Meschede, M., Warr, L.N., 2019. *The Geology of Germany*. Springer Nature, Switzerland.
- Moore, D.M., Reynolds, R.C.J., 1997. *X-Ray Diffraction and the Identification and Analysis of Clay Minerals*, 2 ed. Cambridge University Press, Oxford, New York.
- Msinjili, N.S., Gluth, G.J.G., Sturm, P., Vogler, N., Kühne, H.-C., 2019. Comparison of calcined illitic clays (brick clays) and low-grade kaolinitic clays as supplementary cementitious materials. *Mater. Struct.* 52, 94.
- Murray, H.H., 2007. *Common Clays*. In: Murray, H.H. (Ed.), *Developments in Clay Science*. Elsevier, Amsterdam, pp. 141–145.
- O'Connor, B.H., Raven, M.D., 1988. Application of the Rietveld refinement procedure in assaying powdered mixtures. *Powder Diffract.* 3, 2–6.
- Radczewski, O.E., 1968. *Die Rohstoffe der Keramik*. Springer, Berlin/Heidelberg.
- Scarlett, N.V.Y., Madsen, I.C., 2006. Quantification of phases with partial or no known crystal structures. *Powder Diffract.* 21, 278–284.
- Scarlett, N.V.Y., Madsen, I.C., 2018. Effect of microabsorption on the determination of amorphous content via powder X-ray diffraction. *Powder Diffract.* 33, 26–37.
- Scherb, S., Beuntner, N., Thienel, K.-C., 2018. Reaction kinetics of the basic clays present in natural mixed clays. In: Martirena, F., Favier, A., Scrivener, K. (Eds.), *Calcined Clays for Sustainable Concrete - Proceedings of the 2nd International Conference on Calcined Clays for Sustainable Concrete*. Springer Nature, La Havanna, Cuba, pp. 427–433.
- Scherb, S., Köberl, M., Beuntner, N., Thienel, K.-C., Neubauer, J., 2020. Reactivity of Metakaolin in Alkaline Environment: Correlation of results from Dissolution experiments with XRD Quantifications. *Materials* 13, 18.
- Schneider, M., 2019. The cement industry on the way to a low-carbon future. *Cement Concrete Res* 124, 105792.
- Schulze, S.E., Rickert, J., 2019. Suitability of natural calcined clays as supplementary cementitious material. *Cem. Concr. Compos.* 95, 92–97.

M. Maier et al.

Applied Clay Science 202 (2021) 105990

- Schwarzgopp, F., Drescher, J., Gornig, M., Blazejczak, J., 2019. The demand for primary and secondary Raw Materials in the Mineral and Building Materials Industry in Germany up to 2035. Bundesverband Baustoffe - Steine und Erden e. V. (German Building Materials Association), Berlin, p. 6.
- Scrivener, K.L., John, V.M., Gartner, E.M., 2018. Eco-efficient cements: potential economically viable solutions for a low-CO₂ cement-based materials industry. *Cement Concrete Res* 114, 2–26.
- Scrivener, K., Avet, F., Maraghechi, H., Zunino, F., Ston, J., Hanpongpan, W., Favier, A., 2019. Impacting factors and properties of limestone calcined clay cements (LC³). *Green Materials* 7, 3–14.
- Snellings, R., Li, X., Avet, F., Scrivener, K., 2019. Rapid, Robust, and Relevant (R3) Reactivity Test for Supplementary Cementitious Materials. *ACI Mater. J.* 116, 155–162.
- Sposito, R., Beuntner, N., Thienel, K.-C., 2020. Characteristics of components in calcined clays and their influence on the efficiency of superplasticizers. *Cement and Concrete Composites* 110.
- Taylor, H.F.W., 1997. *Cement Chemistry*, 2. ed. Thomas Telford Ltd, London.
- Taylor, J.C., Matulis, C.E., 1994. A new method for Rietveld clay analysis. Part I. use of a universal measured standard profile for Rietveld quantification of montmorillonites. *Powder Diffract.* 9, 119–123.
- Thury, M., 2002. The characteristics of the Opalinus Clay investigated in the Mont Terri underground rock laboratory in Switzerland. *Comptes Rendus Physique* 3, 923–933.
- Tironi, A., Trezza, M.A., Scian, A.N., Irassar, E.F., 2012. Kaolinitic calcined clays: Factors affecting its performance as pozzolans. *Constr. Build. Mater.* 28, 276–281.
- Tironi, A., Trezza, M.A., Scian, A.N., Irassar, E.F., 2014. Potential use of argentine kaolinitic clays as pozzolanic material. *Appl. Clay Sci.* 101, 468–476.
- Toloczyki, M., Trurnit, P., Voges, A., Wittekindt, H., Zitzmann, A., 2006. Geological Map of Germany 1:1,000,000 (GK1000), in: BGR (Ed.). Hannover.
- Trümer, A., Ludwig, H.M., Schellhorn, M., Diedel, R., 2019. Effect of a calcined Westerwald bentonite as supplementary cementitious material on the long-term performance of concrete. *Appl. Clay Sci.* 168, 36–42.
- Ufer, K., Raven, M.D., 2017. Application of the Rietveld Method in the Reynolds Cup Contest. *Clay Clay Miner.* 65, 286–297.
- Ufer, K., Kleeberg, R., Bergmann, J., Dohrmann, R., 2012a. Rietveld Refinement of Disordered Illite-Smectite Mixed-Layer Structures by a Recursive Algorithm. I: One-Dimensional patterns. *Clay Clay Miner.* 60, 507–534.
- Ufer, K., Kleeberg, R., Bergmann, J., Dohrmann, R., 2012b. Rietveld Refinement of Disordered Illite-Smectite Mixed-Layer Structures by a Recursive Algorithm. II: Powder-Pattern Refinement and Quantitative phase Analysis. *Clay Clay Miner.* 60, 535–552.
- Ufer, K., Kleeberg, R., Monecke, T., 2015. Quantification of stacking disordered Si–Al layer silicates by the Rietveld method: application to exploration for high-sulphidation epithermal gold deposits. *Powder Diffract.* 30, S111–S118.
- Vaculíková, L., Plevová, E., Vallová, S., Koutník, I., 2011. Characterization and differentiation of kaolinites from selected Czech deposits using infrared spectroscopy and differential thermal analysis. *Acta Geodyn. Geomater.* 8, 59–67.
- Wojdyr, M., 2010. Fityk: a general-purpose peak fitting program. *J. Appl. Crystallogr.* 43, 1126–1128.
- Wolters, F., Emmerich, K., 2007. Thermal reactions of smectites—Relation of dehydroxylation temperature to octahedral structure. *Thermochim. Acta* 462, 80–88.
- Worrall, W.E., 1986. *Clays and Ceramic Raw Materials*, 2 ed. Elsevier Applied Science Publishers LTD, Essex.
- Xu, H., Van Deventer, J.S.J., 2000. The geopolymerisation of alumino-silicate minerals. *Int. J. Miner. Process.* 59, 247–266.
- Zunino, F., Boehm-Courjault, E., Scrivener, K., 2020. The impact of calcite impurities in clays containing kaolinite on their reactivity in cement after calcination. *Mater. Struct.* 53, 44.

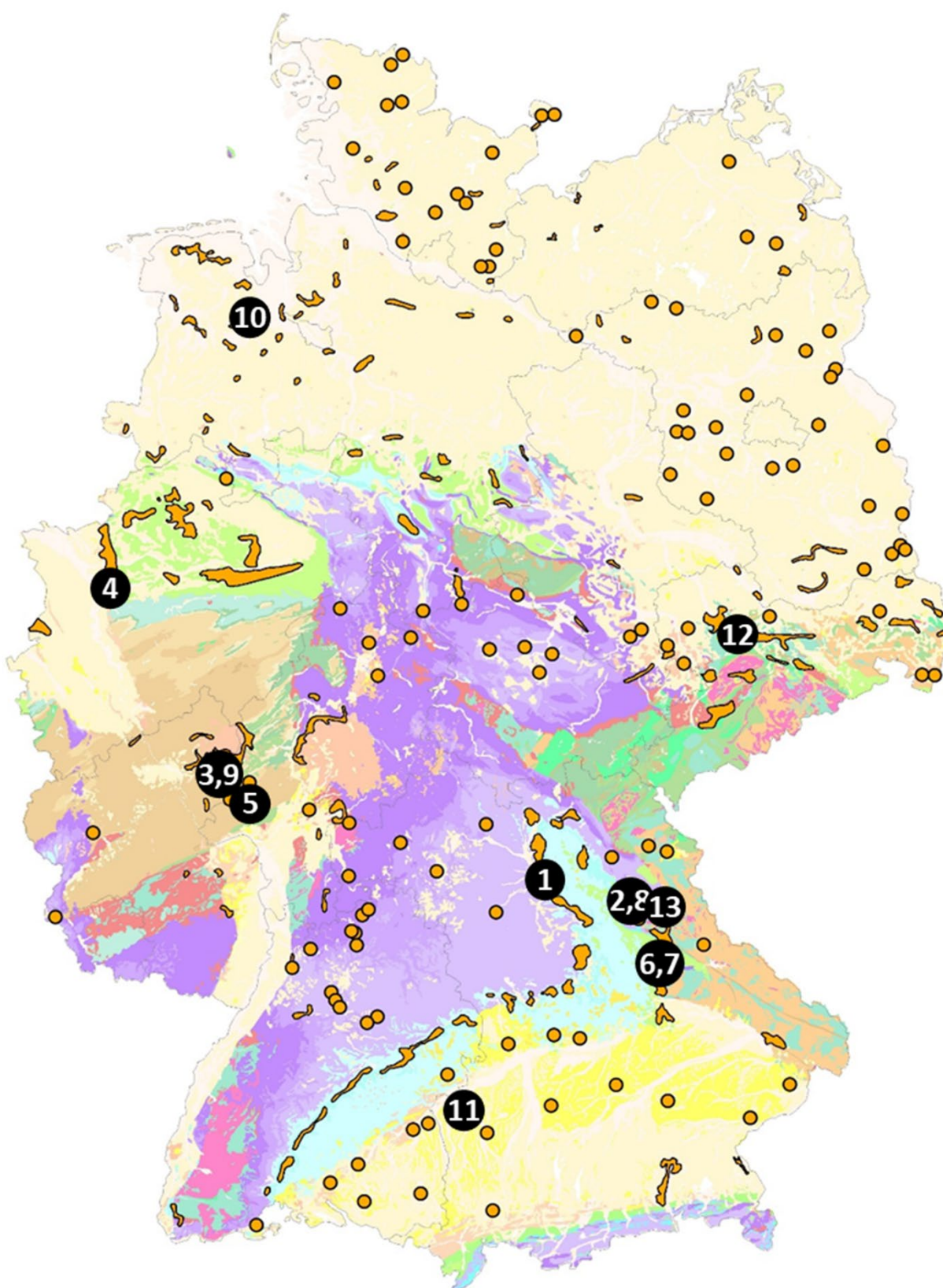


Fig. S1. Location of the sampled deposits marked on the geological map of Germany (Toloczyki et al., 2006). The colors follow the International Stratigraphic Chart (Cohen et al., 2013). Orange dots and areas mark the layer “clay or claystone” taken from the map of mineral resources of Germany (Dill and Röhling, 2007).

8.2 Hydration of cubic tricalcium aluminate in the presence of calcined clays

Reprint

Published in “Journal of the American Ceramic Society”

Volume 104, July 2021, p. 3619–3631; doi: 10.1111/jace.17745

Authors: M. Maier, S. Scherb, A. Neißer-Deiters, N. Beuntner, K.-Ch. Thienel



Received: 16 October 2020 | Revised: 11 February 2021 | Accepted: 11 February 2021

DOI: 10.1111/jace.17745

ORIGINAL ARTICLE

Journal
of the American Ceramic Society

Hydration of cubic tricalcium aluminate in the presence of calcined clays

Matthias Maier | Sebastian Scherb | Axel Neißer-Deiters | Nancy Beuntner | Karl-Christian Thienel

Institute for Construction Materials,
University of the Bundeswehr Munich,
Neubiberg, Germany

Correspondence

Matthias Maier, Institute for Construction
Materials, University of the Bundeswehr
Munich, 85579 Neubiberg, Germany.
Email: matthias.maier@unibw.de

Abstract

Calcined clay blended cements play a major role in cement industry's strategy to reduce CO₂ emissions. During their hydration, an accelerated aluminate reaction is often observed to affect the sulfate balance. The objective of this study was to provide insights into the influence of different calcined clays on the hydration of cubic tricalcium aluminate (C₃A). A cementitious model system consisting of cubic C₃A, quartz powder, calcium sulfate and a model pore solution was investigated. The influence of three different calcined clays and one nanolimestone was examined by a successive replacement of the quartz powder and variation of the calcium sulfate. Heat flow and hydrate phase development were followed by isothermal calorimetry and quantitative in-situ X-ray diffraction. Accelerated ettringite formation and sulfate depletion were observed for all calcined clays, while the nanolimestone exhibited the opposite effect. It was found that adsorption of SO₄ ions and/or Ca-SO₄-complexes at the surface of calcined clay particles is the main factor inhibiting retardation of the C₃A hydration in absence of a silicate reaction. In the Al-rich systems a retardation through sulfate adjustment seems to be impeded by additional Al ions, which react with Ca adsorbed onto and leached from the C₃A surface.

KEYWORDS

calcined clay, metakaolin, sulfate, supplementary cementitious material, tricalcium aluminate, X-ray diffraction

1 | INTRODUCTION

Calcium sulfates take an important role in the reaction of pozzolanic materials by forming ettringite with aluminum ions from the pozzolan.¹ Sulfate carriers like gypsum, bassanite, or anhydrite are used to retard the tricalcium aluminate (C₃A) reaction in ordinary portland cement (OPC).² The latter mechanism is used to avoid flash set and to optimize strength development by

preventing a superposition of the silicate and aluminate clinker reaction.³ As calcined clay blended cements⁴ or limestone calcined clay cements (LC³)⁵ are currently among the most promising solutions to address CO₂ emissions in cement industry⁶, their influence on cement hydration in general and on the aluminate reaction in particular is gaining attention. In calcined clay blended cements, where additional aluminum sources are present, awareness has been raised for extra sulfate demand, as the

This is an open access article under the terms of the Creative Commons Attribution License, which permits use, distribution and reproduction in any medium, provided the original work is properly cited.

© 2021 The Authors. *Journal of the American Ceramic Society* published by Wiley Periodicals LLC on behalf of American Ceramic Society (ACERS).

C₃A and alumina-rich calcined clay minerals might compete for the sulfate at the solid-liquid interface.⁷ Several studies have proven that alumina from metakaolin can contribute to ettringite formation.^{4,8} Hence, in blends of cement and calcined clay there is a risk of undersulfation. An enhanced ettringite formation during the dormant period⁹ as well as an acceleration of the sulfate depletion⁷ is often observed. While some studies refer to the additional aluminum ions^{10,11} to explain aforementioned effects, a recent work suggests the high specific surface area (SSA) of calcined clays as the driving force.¹² The faster aluminate reaction was correlated to the acceleration of the silicate reaction, which is driven by the filler effect. As SO₄²⁻ ions adsorb on the newly formed calcium silicate hydrate phase (C-S-H),¹³⁻¹⁵ an accelerated C-S-H formation speeds up the adsorption of sulfate and thus the sulfate depletion peak. The role of ion adsorption during early cement hydration has gained increasing significance in recent research, especially regarding the aluminate reaction.¹⁶ While the retardation of the C₃A reaction has been traditionally attributed to a diffusion barrier formed by ettringite on the C₃A surface,^{2,17} more recent studies suggest adsorption of calcium and sulfate ions on C₃A, where they hinder dissolution.¹⁸ The fact that the C₃A reaction rate increases before the ettringite consumption by AFm phases begins,¹⁹ as well as the morphology of ettringite, which seems to be unsuitable as a diffusion barrier,²⁰ support this theory. Geng et al.²¹ proved the high porosity of the ettringite needle network at the C₃A reaction front using X-ray ptychography and transmission X-ray microscopy, which rules out any effect as a physical barrier. Myers et al.²² identified adsorbed Ca-sulfur ion pair complexes onto an “Al-rich leached layer,”²³ formed at the C₃A surface, as the key inhibitors of its dissolution. Liu et al.²⁴ demonstrated that it requires a coexistence of calcium as well as sulfate ions to retard the aluminate reaction. Joseph et al.²⁵ combined both theories by suggesting that not only calcium and sulfate ions block the active surface but also ettringite—explicitly *not* as a diffusion barrier. Even though the described theories are still under debate and the mechanisms not fully understood, there is a consensus regarding adsorbed ions as the key inhibitor of the C₃A reaction.²⁶

Raw clays and soils are well known for their adsorption capacity of organic and inorganic solutes.²⁷ The sulfate adsorption capacity of soils is depending, inter alia, on clay content, nature of clay minerals, and pH.²⁸ Lei & Plank²⁹ could prove the adsorption of large amounts of Ca²⁺ onto the surface of clay particles by measuring a strong increase of the initially negative Zeta-potential of muscovite, kaolinite and montmorillonite in Ca²⁺ titrated suspensions. Similar observations were made with a calcined kaolinitic clay.³⁰ There is however lack of data, which could prove adsorption

of SO₄²⁻ or Ca-SO₄ ion pair complexes onto the surface of (calcined) clay particles.

The objective of this study on reduced cementitious model systems was to investigate the influence of calcined clays on the early hydration of C₃A in the presence of calcium sulfate. The effects of sulfate content as well as type and amount of calcined clay, which affects SSA and amount of dissolved aluminum, are studied. A quantitative inspection of phase development in combination with isothermal calorimetry should point out if supplementary cementitious materials (SCM) with high SSA and additional aluminum ions have the potential to accelerate the aluminate reaction independent of C-S-H formation. The work intends to discuss the role of ion release and ion adsorption of calcined clay minerals and their influence on the hydration of C₃A.

2 | EXPERIMENTAL PROCEDURE

2.1 | Cementitious model System

A reduced cementitious model system based on synthetic C₃A was developed. Therefore, cubic C₃A was synthesized by sintering of CaCO₃ (Sigma Aldrich, 99.95%) and Al₂O₃ (Acros, 99.99%) in stoichiometric balanced ratio. The homogenized educts were calcined for 16 h at 1000°C and sintered twice for 6 h at 1400°C in a laboratory muffle furnace with intermediate grinding and homogenization. The final product was ground two times for 5 min in a rotary disc mill (Retsch RS200) using a tungsten carbide grinding tool and sieved through a 63 µm sieve. The purity of the C₃A was verified by XRD (Figure 1) and found in a quantity of 98.5 wt% C₃A together with 1.5 wt% mayenite.

Three calcined clays were chosen for investigation: A fine kaolinitic clay (70.6 wt% kaolinite, high disorder) calcined at 650°C, referred to as CKf, a coarse kaolinitic clay (78.2 wt% kaolinite, low disorder) calcined at 700°C, referred to as CKc and an illitic clay calcined at 770°C, referred to as CI. Calcination was performed in a preheated laboratory muffle furnace for 30 min. The calcination temperatures were chosen following previous studies on pozzolanic reactivity.^{31,32} The calcined clays were ground for 10 min in a rotary disc mill using an agate grinding tool. Additionally, a nanolimestone (Skyspring Nanomaterials, Inc.), referred to as nLS, which provides high SSA but neither reactive silicon nor aluminum ions, was investigated solely by isothermal calorimetry to examine the pure effect of surface area. The mineralogical composition of the calcined clays and the nLS was determined by Rietveld refinement and is given in Table 1. Amorphous content was calculated following the external standard method.^{33,34} Gypsum from Merck with a purity of >99% was used as provided by the producer. A verification of the phase composition by XRD gave a mass proportion

FIGURE 1 Rietveld refinement of a powder pattern of the synthesized C_3A (ICSD 1841) with a minor impurity (1.5 wt%) of mayenite (ICSD 62040) [Color figure can be viewed at wileyonlinelibrary.com]

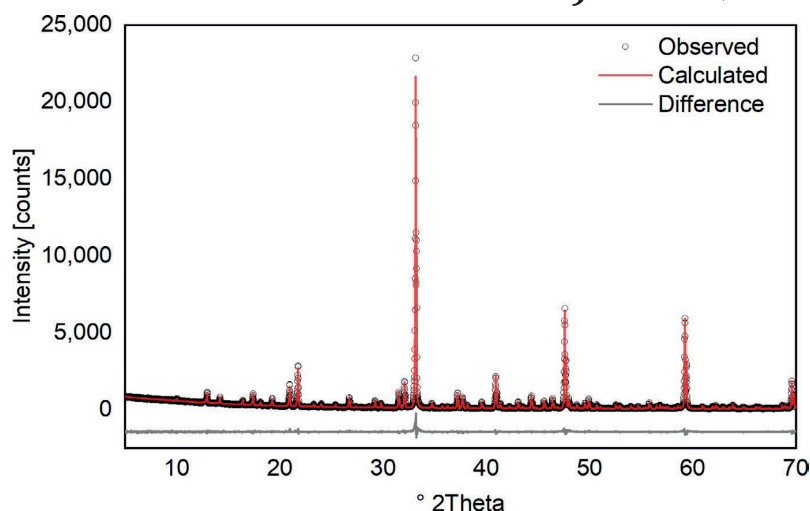


TABLE 1 Mineralogical composition of the SCM [wt.-%]

	nLS	CKf	CKc	CI
Quartz	—	14.	3.3	2.4
Illite/muscovite	—	8.	11.2	53.0
Feldspar	—	—	—	6.9
Hematite	—	0.	—	—
Anatase	—	1.	0.2	—
Calcite	98.0	—	—	—
Dolomite	2.0	—	—	—
Amorphous	—	76.	79.2	32.1

of 25.0 wt% bassanite. Since this amount is considered sufficient as early available sulfate source, no further bassanite was added. Hereafter, the sulfate carrier in the given ratio will be referred to as CS . Table 2 provides the chemical composition, loss on ignition (LOI), mass attenuation coefficient (MAC), SSA and median particle diameter (d_{50}) of all used materials. The MACs were calculated from the chemical composition using the MACs of the single elements provided in International Tables for Crystallography for Cu $K\alpha$ radiation.³⁵ Furthermore, zeta potential is given determined by electroacoustic measurement in a mixed hydroxide solution (MOH)³⁶ at a solid content of 25 wt%. MOH solution was used during all experiments in order to imitate a cementitious pore solution on one hand and to generate a reactive environment for the calcined clays by providing a sufficiently high pH on the other. The solution is composed of 50 mmol/l NaOH and 300 mmol/l KOH and possesses a pH of 13.57. A lime solution was intentionally not used, in order to impede C-S-H formation, which might affect the results. With the aims of reducing heat release and simulating the surface of OPC, the C_3A content was kept constant at 10 wt% in all mixtures by filling it up with quartz powder, which provides

a surface area and particle size distribution comparable to OPC. A basic test series with varying CS content was examined in order to establish a reference system (C_3A_xCS ; $x = 2, 3$) whose test series were examined successively for each calcined clay. The first one investigates the influence of the replacement level of the calcined clays and the nanolimestone. The second one considers the variation of the sulfate carrier at a constant calcined clay content. The notation $C_3A_5CS_{20}CKc$ e.g. refers to a sample consisting of 10 wt% C_3A , 5 wt% sulfate carrier, 20 wt% CKc and 65 wt% quartz powder. All experiments were conducted at a liquid to solid ratio of 0.6. A summary of all investigated systems is provided in Table S1.

2.2 | Evaluation of chemical reactivity

To evaluate the chemical reactivity of the single calcined clays, the soluble silicon and aluminum ions in MOH were determined after 6 and 24 h according to Beuntner and Thienel.³⁶ 1 g of the sample was eluted in 400 ml MOH on an interval agitator. The eluate was filtered and acidified to a pH of 1.0 after the corresponding time. The concentration of silicon and aluminum ions was measured using ICP-OES (Varian ICP-OES 720 ES) as described by Scherb et al.³⁷ A multi-point calibration with an external standard was carried out beforehand. Assessment of chemical reactivity according to current state of the art was performed by determining the evolved heat during the first 72 h using the R^3 calorimetry test.^{38,39}

2.3 | Heat flow calorimetry

Heat flow measurements were conducted in the model system (see Section 2.1) at 25°C in a TAM Air isothermal

Oxides [wt%]	C ₃ A	Gypsum	Quartz powder	nLS	CKc	CKf	CI
SiO ₂	—	—	98.0	—	55.8	62.9	49.5
Al ₂ O ₃	37.7	—	1.	—	39.8	29.8	21.3
Fe ₂ O ₃	—	—	<0.1	—	0.7	4.4	6.6
CaO	62.3	34.1	<0.1	55.5	0.1	0.3	6.9
MgO	—	—	<0.1	0.4	0.2	0.3	2.9
SO ₃	—	48.	—	—	<0.1	<0.1	<0.1
Na ₂ O	—	—	<0.1	—	0.1	0.1	0.3
K ₂ O	—	—	0.5	—	2.5	0.6	6.3
TiO ₂	—	—	<0.1	—	0.6	1.2	0.7
LOI	—	17.	0.3	44.1	0.3	0.4	5.4
MAC [cm ² /g]	52.6	65.5	36.0	73.1	35.8	44.4	57.2
SSA [m ² /g]	0.8	0.7	1.3	10.8	11.3	44.1	82.4
d ₅₀ [μm]	10.8	19.3	15.7	4.5	9.8	29.9	15.2
Zeta potential in MOH [mV]	—	—	−10.8	−11.6	−14.6	−39.4	−20.3

TABLE 2 Chemical composition and physical parameters of the investigated materials

calorimeter from TA instruments. Pastes were prepared manually by external stirring for 60 s and approx. Two gram of homogenized paste was transferred into a flask. The flasks were inserted into the calorimeter within 2 min after water addition. Quartz powder and deionized water were used in a ratio of 2:1 as reference substance.

2.4 | X-ray diffraction

In situ XRD experiments of selected systems were performed with a PANalytical Empyrean diffractometer (CuK α , Bragg–BrentanoHD monochromator, PIXcel1D linear detector) in order to quantify the phase development during hydration. For this purpose, the samples were mixed manually and transferred into a sample holder, which was placed onto a temperature controlled sample stage at 25°C and covered with a 7.5 μm Kapton film. Measurements were carried out at 40 kV and 40 mA for 24 h with a time resolution of 15 min per scan. Rietveld refinement was employed for each scan using Profex-BGMN.⁴⁰ The scattering contribution of the Kapton film was modeled using the measurement of a silicon single-crystal sample carrier covered with a Kapton film.⁴¹ The scale factors of the single phases were extracted to calculate the absolute amounts of the crystalline phases by applying the external standard approach.^{33,34} Recrystallized zircon was used as external standard.⁴² The crystal structures, which were applied for Rietveld refinement are given in Table 3. Monosulfate (C₄A \bar{S} \times H₁₄) was refined using the crystal structure of kuzelite,⁴³ modified with lattice parameters for C₄A \bar{S} \times H₁₄.⁴⁴ The problems regarding quantification of AFm phases are reported elsewhere.¹⁶ The gypsum used in

TABLE 3 Crystal structures used for Rietveld refinement

Structure	ICSD code	References
Zircon	—	[45]
Quartz	34636	[46]
C ₃ A	1841	[47]
Gypsum	—	[48]
Ettringite	155395	[49]
Monosulfate (Kuzelite)	100138	[43]
Strätlingite	69413	[50]

the experiments showed strong preferred orientation during the in-situ measurements, which led to a slight overestimation in Rietveld refinement. This was taken into account by normalizing the retrieved quantities to the maximum theoretical gypsum content. Samples for XRD measurements after 7 days of hydration were prepared analogously to in-situ measurements. The samples were covered and sealed with a Mylar film, placed in a drying cabinet at 25°C for exactly 168 h and measured under the same conditions as the in situ measurements.

2.5 | Scanning electron microscopy

Samples for scanning electron microscopy (SEM) were prepared analogously to Section 2.3 and stored in a sealed plastic container in a drying chamber at 25°C. After 24 h, a fraction of the sample was glued on a sample holder and coated with gold. Secondary electron images were taken in a Zeiss Evo LS 15 at 20 kV and a working distance of 8.5 mm.

2.6 | Thermodynamic modelling

Phase assemblage at thermodynamic equilibrium was calculated using the Gibbs free energy minimization software GEMS⁵¹ in combination with the databases PSI-GEMS⁵² and Cemdata18⁵³. Input recipes were created using the mass proportions of the respective XRD and calorimetry experiments. The conditions for the simulations were set analogous to the experiments at ambient pressure and 25°C. Phase assemblage of the reference system was calculated depending on C \bar{S} content. For the system substituted with 20 wt% calcined kaolinitic clay, the reaction degree of metakaolin was varied in a range which is consistent with data from literature.^{37,54}

3 | RESULTS AND DISCUSSION

3.1 | Chemical reactivity of the calcined clays

The investigated calcined clays exhibit different chemical reactivity during the first 24 h (Figure 2). CKf reveals the fastest release of Si and Al ions in MOH as well as the fastest heat release in the R³-test during the first 22 h. CI exhibits the overall lowest chemical reactivity, even though the amount of released Si ions after 6 h is slightly higher as for CKc. CKc shows a slow reactivity in the R³-test during the first 6 h, which then accelerates and exceeds the evolved heat of CKf after approximately 22 h. However, after 24 h only half the amount of Al and Si ions are released as compared to CKf. The lower chemical reactivity of calcined illite as well as the higher ratio of Si to Al ions in comparison to calcined kaolinite is in line with previous publications.^{32,55,56} The slower reaction rate of CKc compared to CKf can be explained by

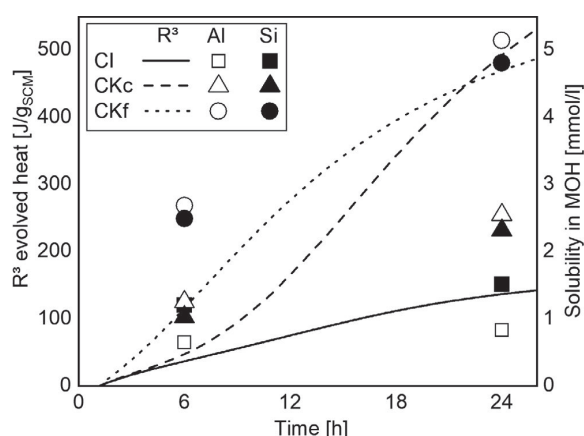


FIGURE 2 Evolved heat during R³ calorimetry test and solubility of Al (relative standard deviation (RSD) = 11%) and Si (RSD = 10%) ions in alkaline solution during the first 24 h

lower specific surface area and degree of disorder in the kaolinite structure.^{31,55,57} The fact that the evolved heat of CKc exceeds CKf after 22 h results from the higher calcined kaolinite content of CKc. The still lower solubility of CKc compared to CKf after 24 h can be attributed to the lower pH of the MOH solution compared to the R³ system and to the fact, that the one represents a reacting system and the other a straight dissolution process.

3.2 | C₃A-systems without calcined clays

The reference system was chosen considering the following conditions: The amount of sulfate should be sufficient for a complete transformation of C₃A into monosulfate without significant formation of CAH phases at thermodynamic equilibrium. This holds for a minimum C \bar{S} content of 5 wt% (Figure 3). Beyond that, a distinct and reproducible heat flow maximum should be present. Figure 4 exhibits the course of the heat flow of the C₃A hydration reaction in absence of calcined clays depending on the C \bar{S} content. The first exothermic peak is not completely recorded due to the external sample preparation. The smaller initial maximum of the systems with lower sulfate content can therefore be explained by an already higher heat release during sample preparation. Pourchet et al.⁵⁸ have shown, that the intensity of this peak is independent of the amount of sulfate added but certainly depends on the type of sulfate carrier. The second heat flow maximum, which can be attributed to the sulfate depletion, shifts to later times with increasing sulfate content together with a significant decrease in peak height and increase in peak width. This effect was observed already by other authors^{25,59,60} and

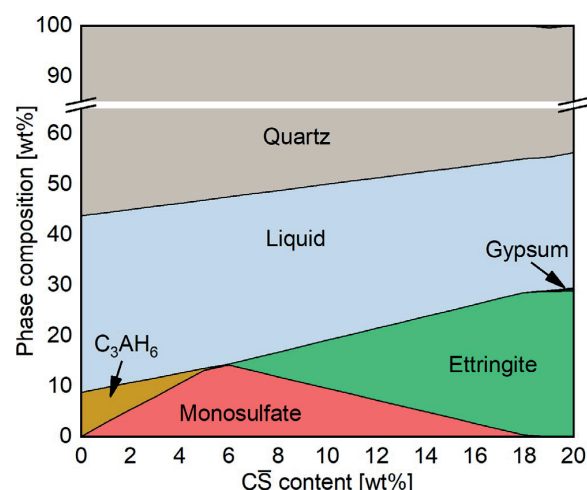


FIGURE 3 Thermodynamic stability in the reference system depending on the C \bar{S} content calculated in GEMS [Color figure can be viewed at wileyonlinelibrary.com]

can be explained by an extended time for the removal of calcium, sulfate and possibly ettringite from the C_3A surface.²⁵ The system C_3A_5CS was chosen for the further investigations. The phase development and the heat flow during the first 24 h of hydration are presented in Figure 5A. The in-situ XRD measurements (Figure S1) reveal that bassanite is not detectable anymore during the first scan of the measurement, as it immediately dissolves.⁶¹ Taking into account, that the theoretical C_3A content before the start of the reaction is 6.25 wt%, a significant initial dissolution of about 2.5 wt% takes place, which is not surprising, regarding the high liquid-to- C_3A ratio. In comparison, in an ordinary Portland cement system with a w/b of 0.5, an

immediate dissolution of 1.8 wt% of initially 6.9 wt% was observed.⁶² The amount of dissolved C_3A is higher at every point of time than the amount that is needed for the precipitation of the corresponding hydrate phases. The difference could partly be dissolved in the pore solution or bound in AFm gel as described by Geng et al.²¹ They observed 'gel-like' areas intermixed with ettringite needles at an early age of hydration. Jansen et al.¹⁶ could not detect significant amounts of amorphous phase and therefore attributed the difference to Al adsorbed on the surface. After the initial dissolution, the C_3A content stays almost constant until the depletion of the gypsum. At this point of time, the maximum ettringite content (6 wt%) is reached, which is significantly lower than the theoretical value (8 wt%) based on the $CaSO_4$ content. As the gypsum depletes, ettringite is consumed and monosulfate ($C_4A\bar{S} \times H_{14}$) forms. The major part of the monosulfate formation still falls into the stadium, where the reaction kinetic is defined by the C_3A dissolution. The heat flow maximum correlates with the maximum C_3A dissolution rate, which is in line with the well-known fact that the accelerated C_3A dissolution after sulfate depletion is the primary reason for the enhanced heat development.⁶¹ After 24 h, approximately 0.8 wt% C_3A are left while 2.8 wt% ettringite and 3.3 wt% monosulfate have formed. For these reactions 2.0 wt% C_3A are needed, which are already provided by the initial dissolution. The dissolution of almost 3.5 wt% of C_3A cannot be explained at this stage, even though if part of it could be caused by an underestimation of AFm phases in Rietveld analysis, due to their low crystallinity, which has already been reported elsewhere.¹⁶

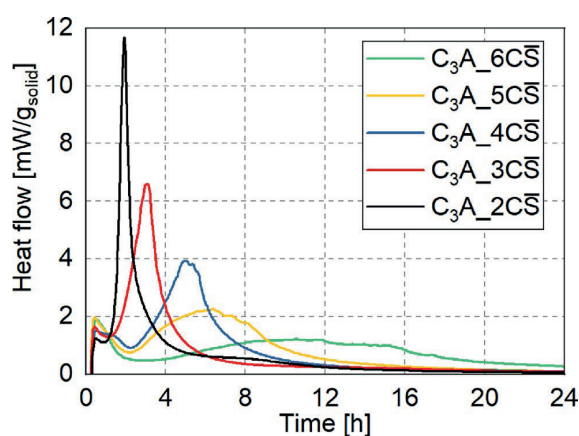


FIGURE 4 Course of heat flow for different sulfate contents in the C_3A_xCS -system [Color figure can be viewed at wileyonlinelibrary.com]

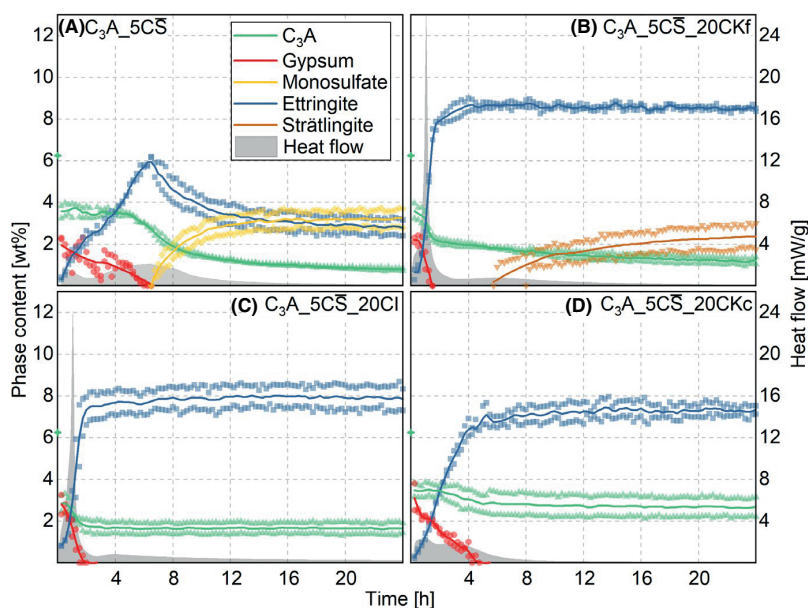


FIGURE 5 Heat flow curves and phase development for the systems with 5 wt% CS ; A) without and B-D) with 20 wt% calcined clay (initial C_3A contents are marked by the green crosses; the symbols correspond to results of two individual measurements, the lines represent the average) [Color figure can be viewed at wileyonlinelibrary.com]

3.3 | C₃A-systems in presence of calcined clays

3.3.1 | Acceleration of the hydration

The addition of 20 wt% calcined clay (CI, CKf, CKc) has a massive impact on the reaction kinetics as sulfate depletion and ettringite formation are accelerated significantly (Figure 5, Figure S2). While the formation of ettringite until its maximum content evolves in two steps in the system C₃A_5C \bar{S} , it forms continuously in the systems with calcined clay. C₃A_5C \bar{S} _20CKf and C₃A_5C \bar{S} _20CI exhibit an acceleration of the sulfate depletion from 6 h down to approximately 2 h. In the course of the heat flow, the first and the second maximum coincide, leaving only a small second heat maximum, which appears after 4 h for CI and after 6 h for CKf. CKc causes a less pronounced acceleration, leaving the two reaction maxima still visible. The systems with calcined clay reach—or in the case of CKc almost reach—the theoretical maximum ettringite content of about 8 wt% (based on the CaSO₄ content). However, there is a significant difference in the consumed C₃A between the different systems. After sulfate depletion, no further decline in C₃A content takes place in the systems C₃A_5C \bar{S} _20CKc and C₃A_5C \bar{S} _20CI. In the system with CKf the C₃A dissolves continuously and strätlingite (C₂ASH₈) begins to form after 6 h. This correlates well with the solubility (Figure 2), which is still lower for CI and CKc after 24 h as for CKf after 6 h.

The acceleration phenomenon could be explained in the first instance by three arguments:

1. The calcined clays provide extra aluminum ions. Therefore, the tricalcium aluminate and the calcined clay minerals compete for the sulfate, which leads to an undersulfation of the system and accelerated ettringite formation.⁷ If this was the case, CI would show the lowest acceleration, since it provides the lowest amount of soluble aluminum ions.
2. The acceleration is mainly driven by the filler effect.⁶³ The high specific surface area of the dehydroxylated clay minerals provides additional nucleation sites for ettringite and/or monosulfate formation. Figure 6 shows an exponential correlation between specific surface area of the systems containing calcined clays, which was varied by using different replacement levels, and the heat flow maximum during isothermal calorimetry (sulfate depletion peak (SDP)). The higher the SSA the earlier the sulfate is depleted. The curves for the systems with different calcined clays however differ clearly between each other. This fact could be interpreted as a coupled influence of SSA and aluminum solubility. In order to verify this theory, the effect of a simple increase of surface area was investigated by substituting the calcined clays by nLS. Surprisingly on

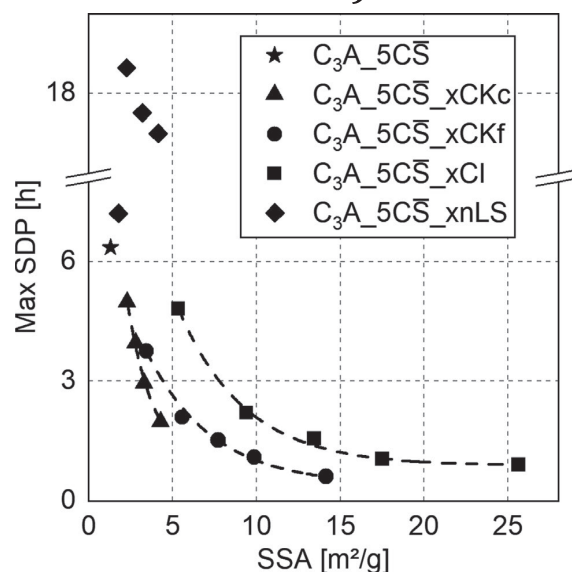


FIGURE 6 Correlation between specific surface area (SSA) of the systems and the time of the maximum of sulfate depletion peak (max SDP) for the three different calcined clays and nLS; Replacement level $x = 5$ (except CKc), 10, 15 (except nLS), 20, 30 wt%

a first glimpse, the addition of nLS leads to a retardation of the reaction (Figure 6). The SSA of nLS is comparable to that of CKc. If physical effects were dominant, nLS and CKc would show a similar acceleration.

3. The Ca^{2+} and SO_4^{2-} ions adsorb on the surface of the clay minerals. The decisive factor therefore, besides the specific surface area, is the surface charge. In the case of C₃A, ion pair complexes adsorb on a negatively charged aluminum-rich leached layer and inhibit the hydration.²² Clay minerals could fulfill these conditions as well. Regarding 2:1 clay minerals, oxygen atoms of the tetrahedral sheet build up the basal surface. Isomorphous substitutions of Al for Si create a negative surface charge,⁶⁴ which also applies for the tetrahedral sheet in kaolinite.⁶⁵ Based on the average structural formula for illite, Al substitutes 20% of tetrahedral Si.⁶⁶ This means, that the basal surface of 2:1 clay minerals provides Al-rich sites with negative charge, where complexes of Ca and SO₄ might adsorb comparable to C₃A. This accounts as well for kaolinite, where the silica facet is charged negatively at pH ≥ 4 and the gibbsite facet at pH > 7 .⁶⁷ Even though, the gibbsite layer gets distorted during dehydroxylation together with a change of Al-coordination from 6-fold to 5- and 4-fold, we still assume a negative charge of this sheet. These hypotheses are supported by the zeta potentials provided in Table 2. CKf shows the highest negative value, followed by CI and CKc. Regarding the high SSA of the calcined clays in comparison to C₃A, the assumption of a much higher adsorption capacity of the former compared

to the latter seems reasonable which would explain the massive acceleration of the C_3A hydration. Consequently, no, or at least significantly lower adsorption occurs on the surface of calcite particles. The Zeta potential of limestone in the presence of $CaSO_4$ and different alkali-sulfates and -hydroxides was found to be notably higher in comparison to ground quartz⁶⁸, which could explain the retarding effect observed when substituting quartz with nLS. However, the measured value in MOH (in absence of $CaSO_4$) is comparable to that of quartz, so there might be further effects that lead to the retardation, for example, change of thermodynamics due to partial calcite dissolution or adsorption of nanoparticles on the C_3A as already observed for nanosilica.⁶⁹

The authors promote the third option. As Figure 6 demonstrates, the influence of SSA is clearly present. However, there are strong differences between the single calcined clays and the nLS. The systems with CKc and CKf exhibit a significantly faster sulfate depletion compared to CI at identical SSA (Figure 6). This cannot be drawn back to additional supply of Al ions, as CKc only provides slightly more Al ions than CI after 6 h (Figure 2).

We therefore assume that the used calcined kaolinite provides a higher negative surface charge than the calcined illite and thus a higher adsorption capacity for Ca^{2+} and SO_4^{2-} . This is however just partly reflected in the zeta potentials as only CKf exhibits a stronger negative value than CI. Lei & Plank²⁹ proved the adsorption of a large amount of Ca^{2+} onto initially negative charged surfaces of muscovite, kaolinite and montmorillonite. They could further point up, that this charge reversal of clay particles also appears in synthetic cement pore solution. In cementitious systems, the zeta potential increases with the Ca/SO_4 ratio.⁶⁸ Liu et al.²⁴ emphasize the availability of both Ca and SO_4 for inhibiting the C_3A dissolution. In the present work, C_3A and $CaSO_4$ are the only soluble Ca-sources, resulting in a lack of Ca ions in the pore solution compared to true cementitious pore solutions. Consequently, no conclusion can be made whether it is the lack of Ca^{2+} , SO_4^{2-} or both, which impedes an inhibition of C_3A dissolution during the first hours in the calcined clay

substituted systems. Nevertheless, it can be concluded that adsorption mechanisms on the surface of the calcined clay particles are the driving force for the accelerated C_3A hydration. The described mechanism is in line with the theory, that adsorption mechanisms play the essential role in the retardation of C_3A hydration.^{16,18,22}

3.3.2 | Phase assemblage

Both SEM images in Figure 7 show intergrown prismatic ettringite crystals. In the left area of Figure 7A, the quartz surface is visible, indicating it does not serve as nucleation area for ettringite. In the depicted area of sample $C_3A_5CS_20CKf$ (B) a denser structure with prismatic and platy crystals is shown of which the latter crystals might represent strätlingite. These crystals seem to nucleate and grow on the surface of the calcined clays. If Al and Si ions are added with calcined clay, the thermodynamic stability shifts from monosulfate to ettringite and strätlingite (Figure 8). Formation of strätlingite is known from metakaolin blended systems, when the metakaolin/portlandite ratio is above 1 and the C-S-H can no longer incorporate aluminum.⁷⁰ Figure 8 shows the thermodynamic stable phase assemblage for a system with 5 wt% $C\bar{S}$ and 20 wt% calcined clay depending on the degree of metakaolin reaction. At a reaction degree of 22 g reacted metakaolin per 100 g calcined clay, monosulfate is not stable anymore. Based on the solubility experiments in the MOH solution, the reaction rate after 24 h is 16.0 g reacted metakaolin per 100 g of calcined clay for CKc and 32.5 g reacted metakaolin per 100 g of calcined clay for CKf. The degrees of reaction in the hydrating systems might differ significantly from the values obtained in the dissolution experiments, however, the range presented in Figure 8 covers degrees of metakaolin reaction obtained from studies in real cementitious systems.⁵⁴ In the CKf-system, the ions released from the calcined kaolinite intervene in the hydration not later than after 6 h, as at this point of time the strätlingite appears for the first time. Strätlingite precipitation is often kinetically delayed in cementitious systems⁷¹, which

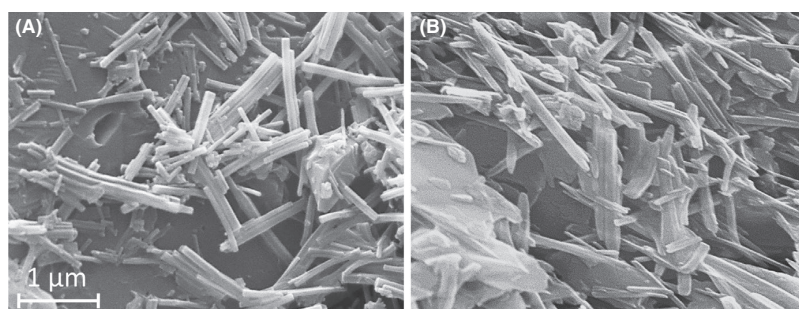


FIGURE 7 SEM images of C_3A_5CS (A) and $C_3A_5CS_20CKf$ (B)

explains the retarded formation in the systems examined here. In the systems $C_3A_5C\bar{S}_20CKc$ and $20CI$, the hydration of C_3A seems to break down once the maximum ettringite content is reached and no formation of strätlingite is visible. To verify this, the samples were investigated by XRD after 7 days of hydration (Figure 9). While in the Ref 5% system ettringite and $C_4A\bar{S} \times H_{14}$ have further reacted to $C_4A\bar{S} \times H_{12}$, ettringite stays stable in all substituted systems and strätlingite has formed. The calcite content in CI leads to the formation of hemicarboaluminate. As CKf provides the fastest release of silicon ions (Figure 2), the strätlingite formation takes place earlier and more rapidly than in the other systems.

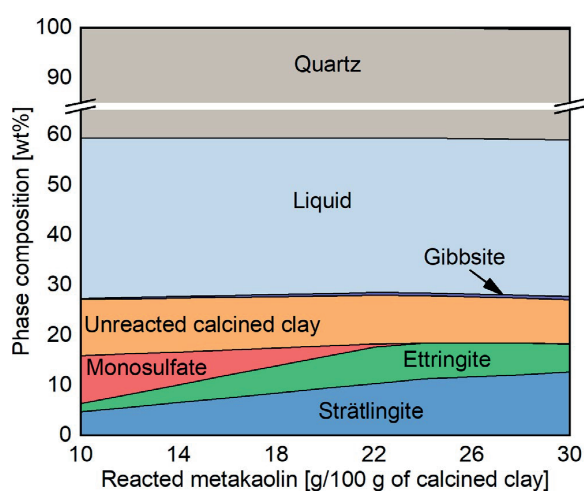


FIGURE 8 Computed phase assemblage in the investigated model system with 5 wt% $C\bar{S}$ and 20 wt% calcined kaolinitic clay depending on the amount of reacted metakaolin [Color figure can be viewed at wileyonlinelibrary.com]

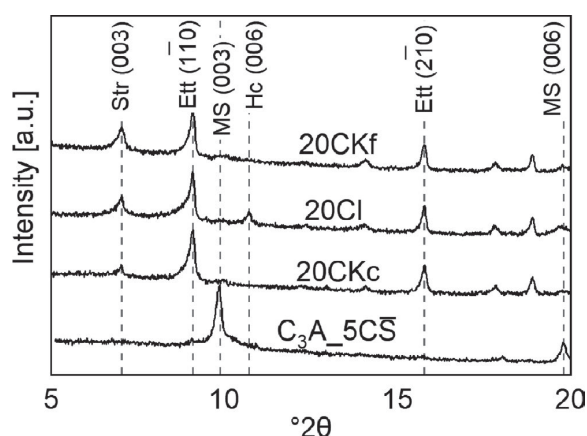


FIGURE 9 XRD patterns of $C_3A_5C\bar{S}$ and the systems with 20 wt% calcined clay after 7 days of hydration (Str = strätlingite, Ett = ettringite, MS = monosulfate, Hc = hemicarboaluminate)

3.4 | Sulfate adjustment

$C\bar{S}$ content was increased stepwise, in order to retard the C_3A hydration (Figure 10). In the systems with CKc this results in a split-up of the heat flow into three maxima. In the CI-systems, the increase in $C\bar{S}$ leads to a broadening and reduction of intensity of the heat flow maximum. With an addition of 20 wt% $C\bar{S}$, the initially sharp heat flow peak begins to form a shoulder. The CKf system allows no retardation at all. The only effect is an increase of intensity and a small

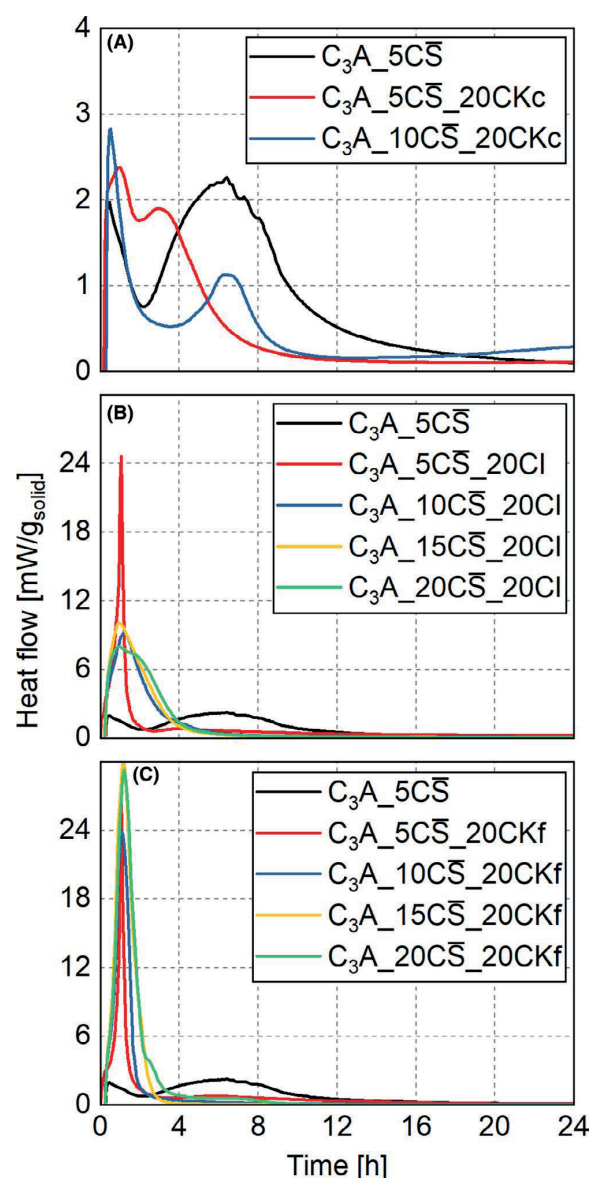


FIGURE 10 Heat flow depending on $C\bar{S}$ content in the systems (A) with CKc, (B) with CI and (C) with CKf (note the different scale of the ordinates) [Color figure can be viewed at wileyonlinelibrary.com]

broadening due to the higher amount of ettringite formation. At an addition of 20 wt% CS , a small shoulder begins to appear.

In the systems with the maximum CS content ($\text{C}_3\text{A}_{20}\text{CS}_{20}\text{CI}$, $\text{C}_3\text{A}_{20}\text{CS}_{20}\text{CKf}$ and $\text{C}_3\text{A}_{10}\text{CS}_{20}\text{CKc}$), in situ XRD measurement were carried out (Figure 11). In the system $\text{C}_3\text{A}_{20}\text{CS}_{20}\text{CI}$, the reaction of C_3A is inhibited after 2.8 h. The formation of ettringite proceeds at two different rates. A rapid ettringite formation

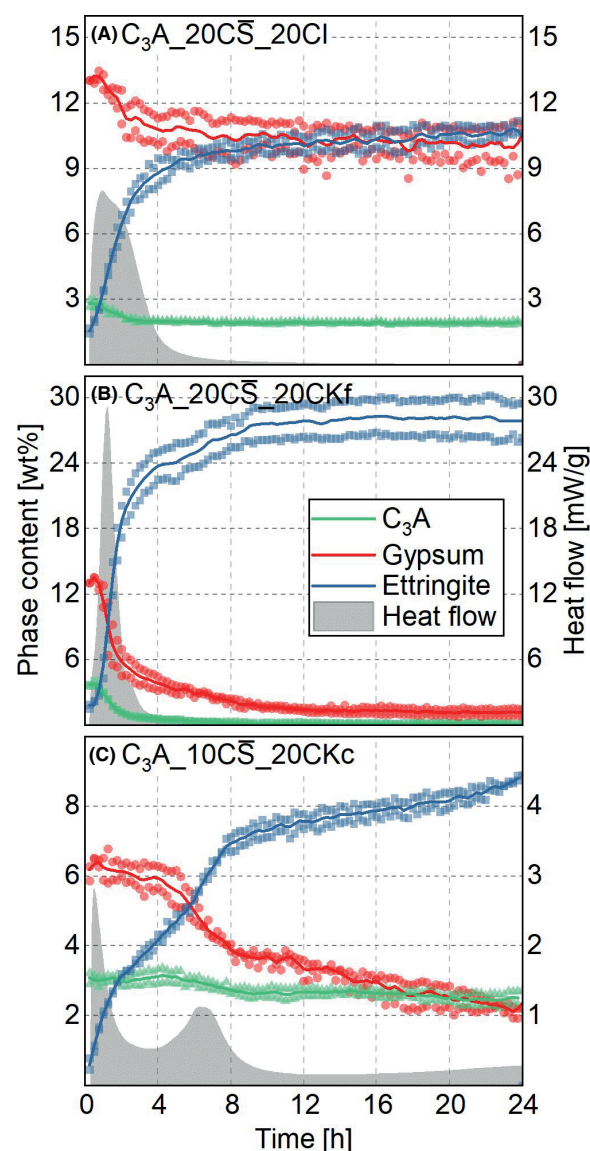


FIGURE 11 Heat flow curves and phase development for the systems with 20 wt% calcined clay and maximum sulfate dosage; the symbols correspond to results of two individual measurements, the lines represent the average (note the different scale of the ordinates) [Color figure can be viewed at wileyonlinelibrary.com]

appears parallel to a fast gypsum and C_3A dissolution until 2.8 h. Subsequently, gypsum dissolution and ettringite formation slow down, while C_3A dissolution stops. It can be deduced, that the inhibition of C_3A dissolution slows down the ettringite formation, which however continues at low level during the remaining measuring time. Since a further dissolution of C_3A during this time is not detectable, the required aluminum might origin from the calcined illite or from amorphous AFm gel as described in Section 3.2. Geng et al.²¹ described the AFm gel to be unstable and “feed the precipitation of ettringite during the low-reactivity period”. This corresponds with the described observations. In the system $\text{C}_3\text{A}_{20}\text{CS}_{20}\text{CKf}$, C_3A and gypsum dissolution as well as ettringite formation proceed significantly more rapidly. The C_3A consumption breaks down at the same time as in the CI system, even though nearly three times the amount of ettringite has precipitated in comparison at this point of time. This proves once more, that the amount of precipitated ettringite does not influence the inhibition of the C_3A hydration, which corresponds to the theory of adsorbed ion pair complexes as key inhibitor.²² Regarding the time between 4 and 12 h, 0.4 wt% of C_3A and 3.0 wt% of gypsum are consumed, while 4.2 wt% of ettringite are precipitated. Only 1.7 wt% of gypsum but 0.9 wt% of C_3A would have to be consumed for the formation of this amount of ettringite. This indicates again that another aluminum source has to be present at this point of time. The fact that during this time range more calcium sulfate is consumed than precipitated suggests that the adsorption of calcium and sulfate continues. Moreover the Ca^{2+} ions from the additionally dissolved gypsum could serve as a reaction partner for a calcium-free aluminum source such as calcined kaolinite. After 24 h, 28.1 wt% of ettringite are formed. The theoretical ettringite maximum is 28.5 wt% based on C_3A as well as gypsum consumption. This suggests in the first instance, that the aluminum ions of the calcined kaolinite are not involved at this point of time, which supports the theory of an intermediate AFm formation. Regarding the system $\text{C}_3\text{A}_{20}\text{CS}_{20}\text{CKc}$, three different phases of ettringite precipitation can be identified. The first one is fed by initially dissolved C_3A , as no more C_3A is dissolved in parallel. After 2.0 h, ettringite formation slows down, while gypsum is consumed at a low rate and C_3A stays constant. Between 5 and 8 h, a second reaction maximum appears, which goes along with accelerated sulfate consumption and ettringite precipitation. In this time range further 0.4 wt% of C_3A are dissolved. Between 8 and 20 h the reaction continues on a low level with slowed down sulfate consumption and ettringite formation. A third maximum with another accelerated ettringite precipitation rate is indicated after 20 h. Even though CI and CKf exposed a quite similar reaction behavior in the presence of 5 wt% CS , they behave remarkably different when the sulfate content is increased stepwise (Table 4). This could be drawn back to the difference in chemical reactivity of the calcined clays and the Al-rich leached layer of the C_3A . In

TABLE 4 Evolved heat of the systems with 20 wt% CKf and CI and different amounts of CS

	Evolved heat (J/g)		
Time [h]	4	12	24
C ₃ A_5CS	16.0	59.4	69.3
C ₃ A_5CS_20CKf	44.0	60.0	68.6
C ₃ A_10CS_20CKf	76.7	82.2	85.0
C ₃ A_20CS_20CKf	122.0	132.7	133.2
C ₃ A_5CS_20CI	48.3	64.0	76.6
C ₃ A_10CS_20CI	64.7	75.2	78.8
C ₃ A_20CS_20CI	74.2	83.2	85.9

consistency with the Al-rich leached layer theory, there is lack of Al at the C₃A/solution interface as compared to Ca with respect to ettringite formation. Consequently, precipitation of ettringite is slowed down. The Al ions released by the calcined clay at this point of time—which are about three times more for CKf as compared to CI—could then serve as reaction partner for the Ca, leached from the surface of the C₃A or adsorbed on the Al-rich leached layer, with the result of a restarting C₃A-dissolution.

4 | CONCLUSION

The results at hand are in the first view in line with previous publications regarding the dominating effect of surface area on the accelerated sulfate consumption in blended cementitious systems. However, they strongly indicate that SO₄ ions and/or Ca-SO₄-complexes can adsorb immediately on the surface of negatively charged calcined clays, depending on surface charge and area. This leads to an acceleration of the sulfate depletion, as the Ca and SO₄ ions are not available to retard the C₃A dissolution. This process, which has previously been exclusively attributed to C-S-H, can thus also take place in absence of C₃S hydration. The authors are aware, that the results obtained here cannot be simply transferred to real cementitious systems, as the presence of C₃S influences the C₃A hydration and vice versa. However, they indicate that the accelerated aluminate reaction in calcined clay blended cementitious systems, can neither be traced back exclusively to the accelerated silicate reaction nor to the additional aluminum ions. A nanolimestone showed the opposite effect as compared to the calcined clays. Obviously, calcined clay minerals play an active role in adsorbing ions from the pore solution and can thereby affect hydration beyond the previously known chemical and physical effects. A secondary source of early available Al seems to inhibit the retardation of the C₃A reaction by further addition of sulfate carriers. This was drawn back to a reaction of the Al provided by the calcined kaolinite with the Ca leached from or

adsorbed on the Al-rich leached layer of the C₃A, disabling the mechanisms which inhibit C₃A dissolution. The observations support the theory of adsorbed ion pair complexes as key inhibitor of the aluminate reaction, as enhanced early ettringite formation was not observed to slow down C₃A dissolution. While the thermodynamic calculations revealed valuable information about phase assemblage of the investigated systems at equilibrium, following studies might also use numerical models to simulate reaction kinetics. As the hydration studies were performed in absence of Ca(OH)₂ and silicate clinker phases, their influence needs to be addressed in future experiments.

ACKNOWLEDGEMENTS

The authors thank Quarzwerke GmbH and Tongrube Degelhof for providing the Quartz powder and the kaolinitic raw clays.

AUTHOR CONTRIBUTION

All authors have read and approved the submitted manuscript.

Author	Research design	Acquisition, analysis or interpretation of data	Drafting the paper or revising it critically
M. Maier	leader	leader	leader
S. Scherb	contributor	contributor	contributor
A. Neißer-Deiters	-	contributor	contributor
N. Beuntner	advisor	advisor	contributor
K.-Ch. Thienel	advisor	advisor	contributor

ORCID

Matthias Maier  <https://orcid.org/0000-0002-2035-4012>
 Sebastian Scherb  <https://orcid.org/0000-0002-8465-4954>
 Nancy Beuntner  <https://orcid.org/0000-0002-3724-8240>
 Karl-Christian Thienel  <https://orcid.org/0000-0002-4087-6205>

REFERENCES

1. Cyr M, Trinh M, Husson B, Casaux-Ginestet G. Effect of cement type on metakaolin efficiency. *Cement Concrete Res.* 2014;64:63–72.
2. Collepardi M, Baldini G, Pauri M, Corradi M. Retardation of tricalcium aluminate hydration by calcium sulfate. *J Am Ceram Soc.* 1979;62(1–2):33–5.
3. Lerch W. The influence of gypsum on the hydration and properties of portland cement pastes. *Proc Am Soc Testing Mater.* 1946;46:1252–91.
4. Beuntner N, Sposito R, Thienel K-C. Potential of calcined mixed-layer clays as pozzolans in concrete. *ACI Mater J.* 2019;116(4):19–29.
5. Scrivener K, Martirena F, Bishnoi S, Maity S. Calcined clay limestone cements (LC³). *Cement Concrete Res.* 2018;114:49–56.

6. Scrivener KL, John VM, Gartner EM. Eco-efficient cements: potential economically viable solutions for a low-CO₂ cement-based materials industry. *Cement Concrete Res.* 2018;114:2–26.
7. Antoni M, Rossen J, Martirena F, Scrivener K. Cement substitution by a combination of metakaolin and limestone. *Cement Concrete Res.* 2012;42(12):1579–89.
8. Zunino F, Scrivener K. The reaction between metakaolin and limestone and its effect in porosity refinement and mechanical properties. *Cement Concrete Res.* 2021;140:106307.
9. Beuntner N. Zur Eignung und Wirkungsweise calcinierter Tone als reaktive Bindemittelkomponente in Zement (On the suitability and effectiveness of calcined clays as reactive binder components in cement). Deutscher Ausschuss für Stahlbeton. Berlin: Beuth Verlag; 2019. p. 207.
10. Avet F, Scrivener K. Investigation of the calcined kaolinite content on the hydration of Limestone Calcined Clay Cement (LC³). *Cement Concrete Res.* 2018;107:124–35.
11. Boháč M, Palou M, Novotný R, Másilko J, Všianský D, Staněk T. Investigation on early hydration of ternary Portland cement-blast-furnace slag–metakaolin blends. *Constr Build Mater.* 2014;64:333–41.
12. Zunino F, Scrivener K. The influence of the filler effect on the sulfate requirement of blended cements. *Cement Concrete Res.* 2019;126:105918.
13. Quennoz A, Scrivener KL. Interactions between alite and C₃A–gypsum hydrations in model cements. *Cement Concrete Res.* 2013;44:46–54.
14. Mota B, Matschei T, Scrivener K. The influence of sodium salts and gypsum on alite hydration. *Cement Concrete Res.* 2015;75:53–65.
15. Valentini L, Dalconi M, Favero M, Artioli G, Ferrari G. In-situ XRD measurement and quantitative analysis of hydrating cement: implications for sulfate incorporation in C–S–H. *J Am Ceram Soc.* 2015;98(4):1259–64.
16. Jansen D, Naber CH, Ectors D, Lu Z, Kong X-M, Goetz-Neunhoffer F, et al. The early hydration of OPC investigated by in-situ XRD, heat flow calorimetry, pore water analysis and ¹H NMR: learning about adsorbed ions from a complete mass balance approach. *Cement Concrete Res.* 2018;109:230–42.
17. Pommersheim J, Chang J. Kinetics of hydration of tricalcium aluminate in the presence of gypsum. *Cement Concrete Res.* 1988;18(6):911–22.
18. Minard H, Garraut S, Regnaud L, Nonat A. Mechanisms and parameters controlling the tricalcium aluminate reactivity in the presence of gypsum. *Cement Concrete Res.* 2007;37(10):1418–26.
19. Bullard JW, Jennings HM, Livingston RA, Nonat A, Scherer GW, Schweitzer JS, et al. Mechanisms of cement hydration. *Cement Concrete Res.* 2011;41(12):1208–23.
20. Scrivener KL, Pratt P, editors. Microstructural studies of the hydration of C₃A and C₄AF independently and in cement paste. *Proc Br Ceram Soc*; 1984.
21. Geng G, Myers RJ, Yu Y-S, Shapiro DA, Winarski R, Levitz PE, et al. Synchrotron X-ray nanotomographic and spectromicroscopic study of the tricalcium aluminate hydration in the presence of gypsum. *Cement Concrete Res.* 2018;111:130–7.
22. Myers RJ, Geng G, Li J, Rodríguez ED, Ha J, Kidkhunthod P, et al. Role of adsorption phenomena in cubic tricalcium aluminate dissolution. *Langmuir.* 2017;33(1):45–55.
23. Skalný J, Tadros ME. Retardation of tricalcium aluminate hydration by sulfates. *J Am Ceram Soc.* 1977;60(3–4):174–5.
24. Liu X, Feng P, Lyu C, Ye S. The role of sulfate ions in tricalcium aluminate hydration: new insights. *Cement Concrete Res.* 2020;130:105973.
25. Joseph S, Skibsted J, Cizer Ö. A quantitative study of the C₃A hydration. *Cement Concrete Res.* 2019;115:145–59.
26. Myers RJ, Geng G, Rodríguez ED, da Rosa P, Kirchheim AP, Monteiro PJM. Solution chemistry of cubic and orthorhombic tricalcium aluminate hydration. *Cement Concrete Res.* 2017;100:176–85.
27. Borisover M, Davis JA. Adsorption of inorganic and organic solutes by clay minerals. In: Tournassat C, Steefel CI, Bourg IC, Bergaya F, editors. *Natural and engineered clay barriers. Developments in Clay Science.* Amsterdam: Elsevier; 2015: 33–70.
28. Tabatabai MA. Physicochemical fate of sulfate in soils. *JAPCA.* 1987;37(1):34–8.
29. Lei L, Plank J. A study on the impact of different clay minerals on the dispersing force of conventional and modified vinyl ether based polycarboxylate superplasticizers. *Cement Concrete Res.* 2014;60:1–10.
30. Li R, Lei L, Sui T, Plank J. Effectiveness of PCE superplasticizers in calcined clay blended cements. *Cement Concrete Res.* 2021;141:106334.
31. Maier M, Beuntner N, Thienel K-C. Mineralogical characterization and reactivity test of common clays suitable as supplementary cementitious material. *Appl Clay Sci.* 2021;202:105990.
32. Scherb S, Maier M, Beuntner N, Thienel K-C, Neubauer J. Reaction kinetics during early hydration of calcined phyllosilicates in clinker-free model systems. *Cement Concrete Res.* 2021;143:106382.
33. O'Connor BH, Raven MD. Application of the Rietveld refinement procedure in assaying powdered mixtures. *Powder Diff.* 1988;3:2–6.
34. Jansen D, Goetz-Neunhoffer F, Stabler C, Neubauer J. A remastered external standard method applied to the quantification of early OPC hydration. *Cement Concrete Res.* 2011;41(6):602–8.
35. Arndt UW, Deslattes RD, Hubbel JH, Indelicato P, Kessler EG, et al. Production and properties of radiation, Table 4.2.4.3. Mass attenuation coefficients (cm² g⁻¹). In: Prince E, editor. *International tables for crystallography volume C: mathematical, physical and chemical tables.* Dordrecht: Springer; 2006. p. 191–258.
36. Beuntner N, Thienel K-C. Solubility and kinetics of calcined clay: study of interaction by pore solution. In: Plank J, Lei L, Eht T, editors. *2nd International Conference on the Chemistry of Construction Materials (ICCCM 2016); 10–12. October 2016. Munich, Germany: Gesellschaft Deutscher Chemiker e.V.; 2016. p. 157–60.*
37. Scherb S, Köberl M, Beuntner N, Thienel K-C, Neubauer J. Reactivity of metakaolin in alkaline environment: correlation of results from dissolution experiments with XRD quantifications. *Materials.* 2020;13(2214):18.
38. Avet F, Snellings R, Alujas Diaz A, Ben Haha M, Scrivener K. Development of a new rapid, relevant and reliable (R₃) test method to evaluate the pozzolanic reactivity of calcined kaolinitic clays. *Cement Concrete Res.* 2016;85:1–11.
39. Snellings R, Li X, Avet F, Scrivener K. Rapid, robust, and relevant (R₃) reactivity test for supplementary cementitious Materials. *ACI Mater J.* 2019;116(4):155–62.
40. Doebelin N, Kleeberg R. Profex: a graphical user interface for the Rietveld refinement program BGMN. *J Appl Crystallogr.* 2015;48(5):1573–80.

41. Scherb S, Beuntner N, Thienel K-C, Neubauer J. Quantitative X-ray diffraction of free, not chemically bound water with the PONKCS method. *J Appl Crystallogr*. 2018;51(6):1535–43.
42. Jansen D, Stabler C, Goetz-Neunhoeffer F, Ditttrich S, Neubauer J. Does ordinary portland cement contain amorphous phase? A quantitative study using an external standard method. *Powder Diffr*. 2012;26(1):31–8.
43. Allmann R. Refinement of the hybrid layer structure $[\text{Ca}_2\text{Al}(\text{OH})_6]^{+} [1/2\text{SO}_4 \cdot 3\text{H}_2\text{O}]^{-}$. *Neues Jahrbuch für Mineralogie*. 1977;3:136–44.
44. Pöllmann H, Kuzel HJ. PDF data sheet: 42-0062, Calcium Aluminum Sulfate Hydrate. Mineralogical Institute of University Erlangen, ICDD Grant-in-Aid; 1990.
45. Krstanovic I. Redetermination of the oxygen parameters in zircon (ZrSiO_4). *Acta Crystallogr A*. 1958;11(12):896–7.
46. Young RA, Post B. Electron density and thermal effects in alpha quartz. *Acta Crystallogr A*. 1962;15(4):337–46.
47. Mondal P, Jeffery JW. The crystal structure of tricalcium aluminate, $\text{Ca}_3\text{Al}_2\text{O}_6$. *Acta Crystallographica Section B*. 1975;31(3):689–97.
48. Comodi P, Nazzareni S, Francesco P, Speziale S. High-pressure behavior of gypsum: a single-crystal X-ray study. *Am Miner*. 2008;93:1530–7.
49. Goetz-Neunhoeffer F, Neubauer J. Refined ettringite ($\text{Ca}_6\text{Al}_2(\text{SO}_4)_3(\text{OH})_{12} \cdot 26\text{H}_2\text{O}$) structure for quantitative X-ray diffraction analysis. *Powder Diffr*. 2005;21(1):4–11.
50. Rinaldi R, Sacerdoti M, Passaglia E. Strätlingite: crystal structure, chemistry, and a reexamination of its polytype vertumnite. *Eur J Mineral*. 1990;2:841–9.
51. Kulik DA, Wagner T, Dmytrieva SV, Kosakowski G, Hingerl FF, Chudnenko KV, et al. GEM-Selektor geochemical modeling package: revised algorithm and GEMS3K numerical kernel for coupled simulation codes. *Computational Geosciences*. 2013;17(1):1–24.
52. Hummel W, Berner U, Curti E, Pearson FJ, Thoenen T. Nagra/PSI chemical thermodynamic data base 01/01. *Radiochim Acta*. 2002;90(9-11):805–13.
53. Lothenbach B, Kulik DA, Matschei T, Balonis M, Baquerizo L, Dilnesa B, et al. Cemdata18: a chemical thermodynamic database for hydrated Portland cements and alkali-activated materials. *Cement Concrete Res*. 2019;115:472–506.
54. Avet F, Li X, Scrivener K. Determination of the amount of reacted metakaolin in calcined clay blends. *Cement Concrete Res*. 2018;106:40–8.
55. Hollanders S, Adriaens R, Skibsted J, Cizer Ö, Elsen J. Pozzolanic reactivity of pure calcined clays. *Appl Clay Sci*. 2016;132–133:552–60.
56. He C, Osbaeck B, Makovicky E. Pozzolanic reactions of six principal clay minerals: activation, reactivity assessments and technological effects. *Cement Concrete Res*. 1995;25(8):1691–702.
57. Tironi A, Trezza MA, Scian AN, Irassar EF. Kaolinitic calcined clays: factors affecting its performance as pozzolans. *Constr Build Mater*. 2012;28(1):276–81.
58. Pourchet S, Regnaud L, Perez JP, Nonat A. Early C_3A hydration in the presence of different kinds of calcium sulfate. *Cement Concrete Res*. 2009;39(11):989–96.
59. Quennoz A, Scrivener KL. Hydration of C_3A -gypsum systems. *Cement Concrete Res*. 2012;42(7):1032–41.
60. Bergold ST, Goetz-Neunhoeffer F, Neubauer J. Interaction of silicate and aluminate reaction in a synthetic cement system: Implications for the process of alite hydration. *Cement Concrete Res*. 2017;93:32–44.
61. Hesse C, Goetz-Neunhoeffer F, Neubauer J. A new approach in quantitative in-situ XRD of cement pastes: Correlation of heat flow curves with early hydration reactions. *Cement Concrete Res*. 2011;41(1):123–8.
62. Jansen D, Goetz-Neunhoeffer F, Lothenbach B, Neubauer J. The early hydration of Ordinary Portland Cement (OPC): An approach comparing measured heat flow with calculated heat flow from QXRD. *Cement Concrete Res*. 2012;42(1):134–8.
63. Oey T, Kumar A, Bullard JW, Neithalath N, Sant G. The filler effect: the influence of filler content and surface area on cementitious reaction rates. *J Am Ceram Soc*. 2013;96(6):1978–90.
64. Schoonheydt RA, Johnston CT. Chapter 3 surface and interface chemistry of clay minerals. In: Bergaya F, Theng BKG, Lagaly G, editors. *Developments in clay science*. Amsterdam: Elsevier; 2006. p. 87–113.
65. Zhou Z, Gunter WD. The nature of the surface charge of kaolinite. *Clays Clay Miner*. 1992;40(3):365–8.
66. Środoń J, Elsass F, McHardy WJ, Morgan DJ. Chemistry of illite-smectite inferred from TEM measurements of fundamental particles. *Clay Miner*. 1992;27(2):137–58.
67. Kumar N, Andersson MP, van den Ende D, Mugele F, Siretanu I. Probing the surface charge on the basal planes of kaolinite particles with high-resolution atomic force microscopy. *Langmuir*. 2017;33(50):14226–37.
68. Lowke D, Gehlen C. The zeta potential of cement and additions in cementitious suspensions with high solid fraction. *Cement Concrete Res*. 2017;95:195–204.
69. Hou P, Wang X, Zhao P, Wang K, Kawashima S, Li Q, et al. Physicochemical effects of nanosilica on $\text{C}_3\text{A}/\text{C}_3\text{S}$ hydration. *J Am Ceram Soc*. 2020;103(11):6505–18.
70. Murat M. Hydration reaction and hardening of calcined clays and related minerals: I. Preliminary investigation on metakaolinite. *Cement Concrete Res*. 1983;13(2):259–66.
71. Okoronkwo MU, Glasser FP. Stability of strätlingite in the CASH system. *Mater Struct*. 2016;49(10):4305–18.

SUPPORTING INFORMATION

Additional supporting information may be found online in the Supporting Information section.

How to cite this article: Maier M, Scherb S, Neißer-Deiters A, Beuntner N, Thienel K-C. Hydration of cubic tricalcium aluminate in the presence of calcined clays. *J Am Ceram Soc*. 2021;104:3619–3631. <https://doi.org/10.1111/jace.17745>

Hydration of cubic tricalcium aluminate in the presence of calcined clays

Matthias Maier^{1*}, Sebastian Scherb¹, Axel Neißer-Deiters¹, Nancy Beuntner¹, Karl-Christian Thienel¹

¹Institute for Construction Materials, University of the Bundeswehr Munich, 85579 Neubiberg, Germany

matthias.maier@unibw.de

*corresponding author

SUPPLEMENTARY MATERIAL

Table S1 Summary table of all investigated systems. The numbers represent wt% on a dry basis

	Qtz	C ₃ A	C \bar{S}	CKc	CKf	CI	nLS	liquid-solid-ratio	Isothermal calorimetry	In-situ XRD
C3A_2C \bar{S}	88	10	2					0.6	X	
C3A_3C \bar{S}	87	10	3					0.6	X	
C3A_4C \bar{S}	86	10	4					0.6	X	
C3A_5C \bar{S}	85	10	5					0.6	X	X
C3A_6C \bar{S}	84	10	6					0.6	X	
C3A_5C \bar{S} _10CKc	75	10	5	10				0.6	X	
C3A_5C \bar{S} _15CKc	70	10	5	15				0.6	X	
C3A_5C \bar{S} _20CKc	65	10	5	20				0.6	X	X
C3A_5C \bar{S} _30CKc	55	10	5	30				0.6	X	
C3A_5C \bar{S} _5CKf	80	10	5		5			0.6	X	
C3A_5C \bar{S} _10CKf	75	10	5		10			0.6	X	
C3A_5C \bar{S} _15CKf	70	10	5		15			0.6	X	
C3A_5C \bar{S} _20CKf	65	10	5		20			0.6	X	X
C3A_5C \bar{S} _30CKf	55	10	5		30			0.6	X	
C3A_5C \bar{S} _5CI	80	10	5			5		0.6	X	
C3A_5C \bar{S} _10CI	75	10	5			10		0.6	X	
C3A_5C \bar{S} _15CI	70	10	5			15		0.6	X	
C3A_5C \bar{S} _20CI	65	10	5			20		0.6	X	X
C3A_5C \bar{S} _30CI	55	10	5			30		0.6	X	
C3A_5C \bar{S} _10nLS	75	10	5				10	0.6	X	
C3A_5C \bar{S} _20nLS	65	10	5				20	0.6	X	
C3A_5C \bar{S} _30nLS	55	10	5				30	0.6	X	
C3A_10C \bar{S} _20CKc	60	10	10	20				0.6	X	
C3A_10C \bar{S} _20CKf	60	10	10		20			0.6	X	
C3A_10C \bar{S} _20CI	60	10	10			20		0.6	X	
C3A_15C \bar{S} _20CKf	55	10	15		20			0.6	X	
C3A_15C \bar{S} _20CI	55	10	15			20		0.6	X	
C3A_20C \bar{S} _20CKf	50	10	20		20			0.6	X	X
C3A_20C \bar{S} _20CI	50	10	20			20		0.6	X	X

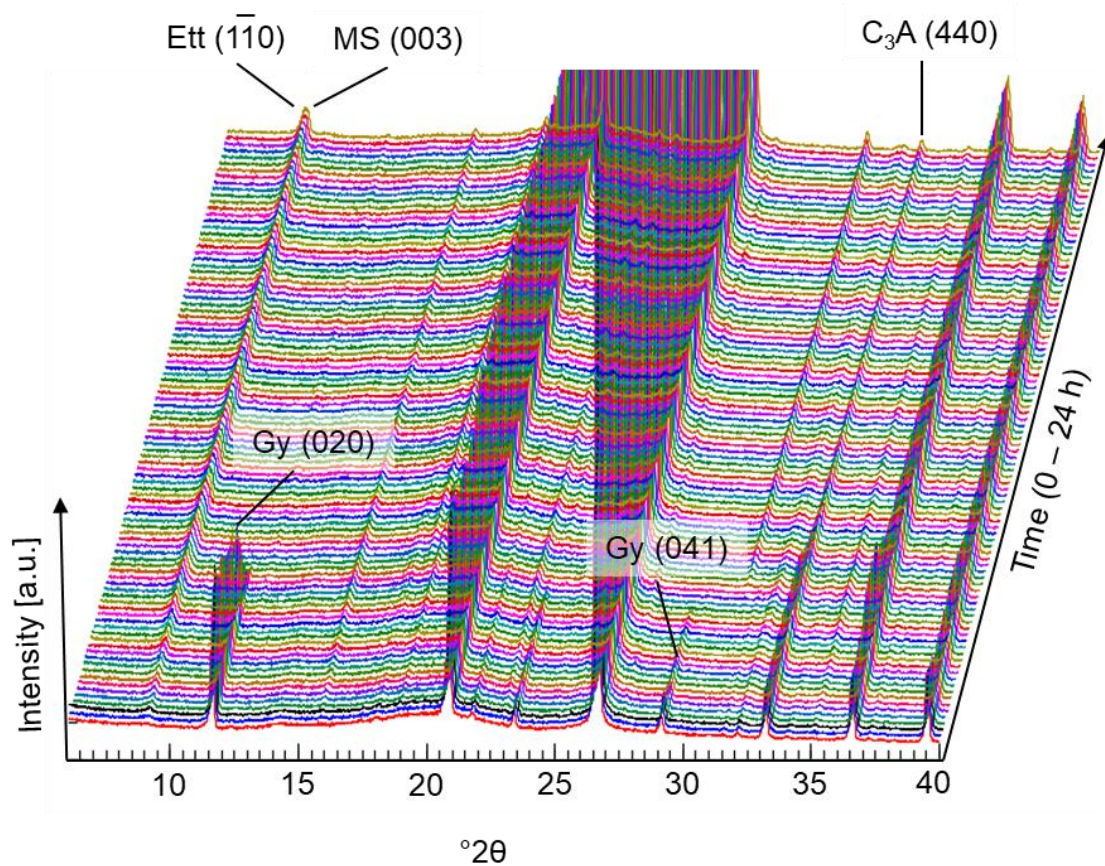


Figure S1 In-situ XRD patterns of C_3A_5CS

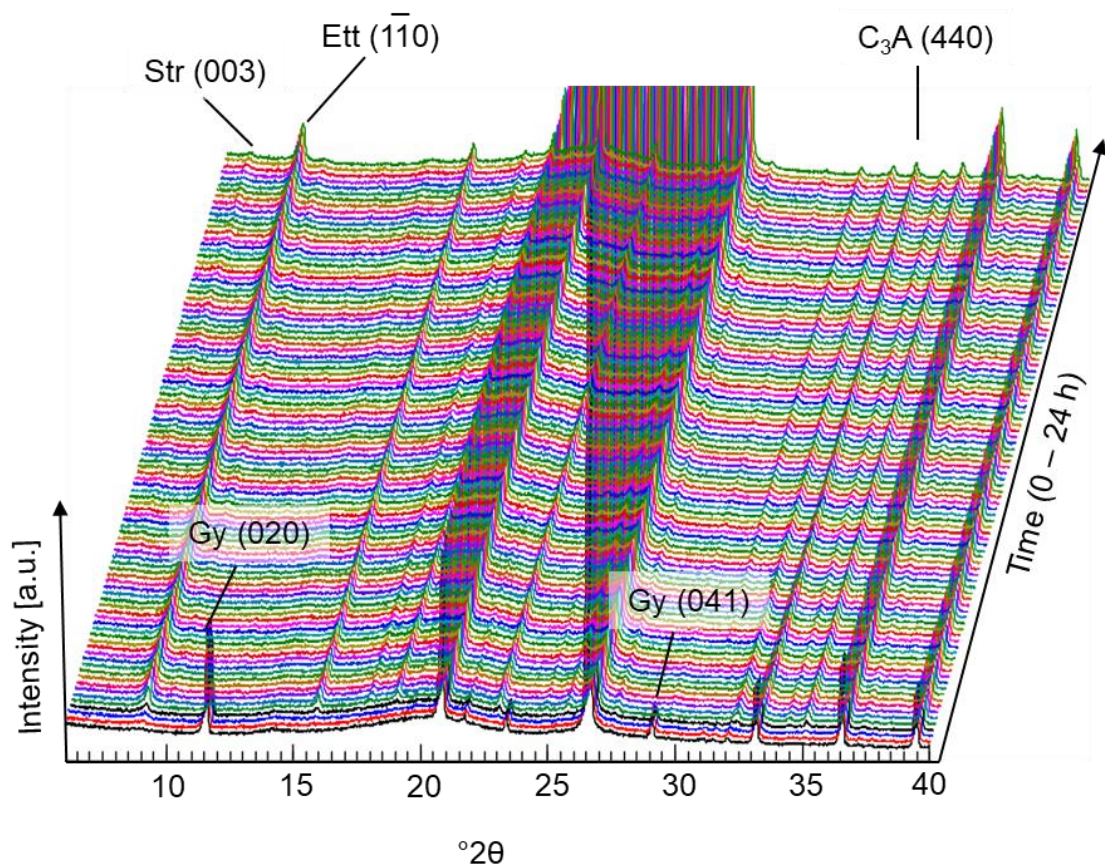


Figure S2 In-situ XRD patterns of $C_3A_5CS_{20CKf}$

8.3 Influence of particle characteristics of calcined clays and limestone on the early hydration and sulfate demand of blended cement

Reprint:

Published in "Cement and Concrete Research"

154, April 2022, p.106736; doi: 10.1016/j.cemconres.2022.106736

Authors: M. Maier, R. Sposito, N. Beuntner, K.-Ch. Thienel



Contents lists available at ScienceDirect

Cement and Concrete Research

journal homepage: www.elsevier.com/locate/cemconres

Particle characteristics of calcined clays and limestone and their impact on early hydration and sulfate demand of blended cement

Matthias Maier^{*}, Ricarda Sposito, Nancy Beuntner, Karl-Christian Thienel

Institute for Construction Materials, University of the Bundeswehr Munich, Werner-Heisenberg-Weg 39, Neubiberg 85579, Germany

ARTICLE INFO

Keywords:

Calcined clay
Supplementary cementitious material
X-ray diffraction
Sulfate demand

ABSTRACT

Supplementary cementitious materials (SCMs) can alter significantly the early hydration behavior of blended cement. While the underlying mechanisms have been intensively discussed in literature, they need to be extended regarding SCMs with complex mineralogy and surface properties, such as calcined clays. In this study, a blended Portland limestone cement was monitored during the first 48 h of hydration using in situ X-ray diffraction and isothermal calorimetry. The influence of a fine limestone and four different calcined clays, which vary in mineralogical composition and particle properties, was investigated at a replacement level of 30 wt%. The sulfate content was gradually adjusted and its influence on heat evolution and phase development was examined. It was shown, that depending on their particle properties, the investigated SCMs influence the aluminate and silicate clinker reaction by different mechanisms and to varying extents. The results underline the importance of proper sulfation of blended cements.

1. Introduction

The supply and usage of supplementary cementitious material (SCM) is a key element in the CO₂ reduction strategy of the cement industry [1]. The partial replacement of cement clinker up to 50 wt% by calcined clay, limestone and a minor amount of gypsum currently provides the greatest potential as a global short-term solution to reduce cement producer's greenhouse gas emission drastically [2]. The mechanical properties of concrete produced with these so-called LC³ blends are comparable to those with ordinary Portland cement. This is attributable to the synergetic effect of limestone and calcined clay, which induces the formation of additional hydration products combined with a stabilization of ettringite [3–6]. The early hydration behavior as well as the rheological properties however can alter significantly in presence of calcined clays [7–11].

The first hours of hydration of blended cements are predominantly influenced by pore solution chemistry (pH, water activity and dissolved ions) and physical effects of the used SCM [12,13]. The latter include the filler effect, which accelerates early cement hydration. It can be split up in three different mechanisms [14], which are described as “dilution effect” (additional space for hydration products and higher water-to-cement ratio [15]), “nucleation effect” (additional surface for nucleation of hydration products [16]) and “accelerated dissolution effect”

(faster dissolution of clinker due to higher shear rates caused by smaller interparticle distance [17]). In the case of limestone, it has been shown that it is a more effective filler than quartz [18] with regard to accelerating C-S-H formation, due to its interfacial properties [16] and/or induction of ion-exchange reactions with the C-S-H [19]. This was explained by a stronger interaction of the limestone surface with Ca²⁺ from the pore solution compared to quartz and Portland cement [20] and a higher undersaturation with regard to alite [21].

It is quite conceivable, that the special surface properties of calcined clays do influence the described effects to a different extend and in another way compared to established SCMs. As early strength development in calcined clay blended cement is significantly affected by sulfate content, an adjustment of sulfate carrier is mandatory [6]. However, it was stated elsewhere to be sufficient to optimize sulfate content only to prevent flash set, since excess calcium sulfate (C₃S) is able to form additional ettringite with aluminum from the calcined clay and portlandite after the aluminate peak. This reaction is supposed to reduce available portlandite for further C-(A)-S-H formation in the course of the pozzolanic reaction [22]. Investigations in clinker-free model systems proved the formation of ettringite by aluminum ions released from calcined phyllosilicates together with C₃S and portlandite [23]. The same reaction was observed in LC³ systems, provided that sufficient sulfate is available [4]. An enhanced ettringite formation was observed even

^{*} Corresponding author.

E-mail address: matthias.maier@unibw.de (M. Maier).

<https://doi.org/10.1016/j.cemconres.2022.106736>

Received 24 August 2021; Received in revised form 14 January 2022; Accepted 24 January 2022

Available online 2 February 2022

0008-8846/© 2022 Elsevier Ltd. All rights reserved.

during the first hours of hydration in calcined clay blended cement [8,24]. The role of $\text{C}\bar{\text{S}}$ on cement hydration in general has been reviewed recently [25]. The retardation of the C_3A hydration by $\text{C}\bar{\text{S}}$ is assigned to an adsorption of ion pair complexes onto the C_3A surface [25,26]. Jansen et al. [27] emphasize the essential role of adsorbed ions during hydration, but provide only evidence for the adsorption of Al and sulfate in context with sulfate depletion, but not of calcium. The influence of $\text{C}\bar{\text{S}}$ on the alite hydration is characterized by a retardation during the initial stage but an enhancement during the acceleration period. The higher degree of C_3S hydration in presence of $\text{C}\bar{\text{S}}$ has been observed for systems with and without aluminates, leading to the assumption that the mechanism results from a direct interaction between $\text{C}\bar{\text{S}}$ and C_3S hydration, independent of the aluminate reaction [28].

A question still not yet fully resolved is how the special particle characteristics of calcined clay minerals influence the hydration behavior of blended cements during early hydration. Zunino and Scrivener [29] state the filler effect introduced by the additional specific surface area (SSA) of the SCM as the dominating factor regarding the acceleration of the early silicate and aluminate clinker reaction. They relate the latter to the adsorption of sulfate onto C-S-H, which has been observed by several authors [17,30–32]. While several studies could prove the adsorption of huge amounts of Ca^{2+} from the pore solution on the initially negatively charged calcined clay particles [33–35], this mechanism was also implicated to affect the hydration of calcined clay minerals in clinker-free model systems [23]. Investigations in C_3A – $\text{C}\bar{\text{S}}$ systems blended with calcined clays linked an acceleration of the sulfate depletion to adsorption of SO_4^{2-} onto the positively charged Ca^{2+} layer formed on the surface of the calcined clay particles [36]. Adsorption of Ca^{2+} and SO_4^{2-} has been described for other SCMs as calcite [37] or blast furnace slag [38] as well. Even though aforementioned mechanisms are either directly or indirectly linked to the surface area and/or surface chemistry of the SCM, an influence of the aluminum content of the SCM on the optimal sulfate content of blended cement is still matter of debate [25,39]. A pronounced aluminate heat flow peak with enhanced ettringite precipitation was for instance also observed in clinker-free systems containing portlandite and $\text{C}\bar{\text{S}}$ [23]. However, it has not yet been verified, whether aluminates from calcined clays contribute to the ettringite formation before the aluminate peak in blended cements and therefore to its acceleration. It has been rather stated that the ettringite formation at this point is exclusively influenced by C_3A fineness and not by the type of SCM [28,29].

The present study aims to verify the discussed mechanisms that modify the course of the early hydration in cements blended with calcined clay and/or limestone, with a special focus on the aluminate reaction. Therefore, a Portland limestone cement replaced with 30 wt% of SCMs of different grain size distribution, SSA, surface charge, particle morphology and aluminum content is investigated. Influence of different concentrations of Ca^{2+} and SO_4^{2-} on the surface charge of these SCMs is investigated by measurement of zeta potential during titration experiments. The hydration of blended cements with the selected SCMs at different sulfate contents is followed by isothermal calorimetry and partially by in situ X-ray diffraction. The difference in the acceleration mechanism of various types of calcined clays and a fine limestone powder regarding the silicate and aluminate clinker reaction and their influence on early hydrate phase formation are discussed. This should allow a further differentiation between effects caused by a simple increase of the surface area and the incorporation of pozzolanic reactive SCMs with special particle properties and surface chemistry.

2. Materials and methods

A commercially available Portland limestone cement (PLC)

Table 1

Chemical composition (provided by supplier) and main phases (by Rietveld refinement, XRD) of the PLC used. The sulfate carrier mainly contains gypsum and anhydrite, but was calculated to an equivalent CaSO_4 ($\text{C}\bar{\text{S}}$) content based on the molar weights.

Oxides [wt%]		Phases [wt%]	
SiO_2	17.9	Alite	48.5
Al_2O_3	4.8	Belite	12.5
Fe_2O_3	2.7	C_3A	5.7
CaO	60.5	C_4AF	6.9
MgO	1.7	Calcite	14.7
SO_3	2.7	Dolomite	2.3
K_2O	0.7	$\text{C}\bar{\text{S}}_{\text{equ}}$	2.7
Na_2O	0.1		
TiO_2	0.3		
P_2O_5	0.3		

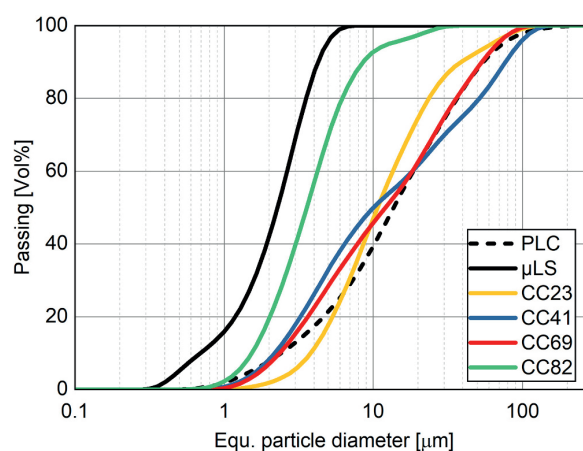


Fig. 1. Particle size distribution of the materials used.

complying with DIN EN 197-1 as CEM II/A-LL 32.5 R was used for the investigations. The chemical and mineralogical composition is provided in Table 1.

The influence of four calcined clays with different physical and mineralogical parameters (e.g. calcined kaolinite content) on the hydration behavior was investigated at a replacement level of 30 wt%. The clays were calcined for 1 h in a laboratory muffle furnace at 800 °C and ground for 10 min in a rotating disc mill. Additionally, one fine limestone powder (pure calcite), referred to as micro limestone (μLS), was used at the same replacement level for comparative investigations. As the used PLC already contains significant amounts of limestone, this allows to exclusively investigate the filler effect, since the SSA of the μLS is significantly higher compared to the PLC. The designation of the investigated calcined clays is CC for calcined clay together with a number that stands for the rounded calcined kaolinite (metakaolin) content. An industrially applied sulfate carrier, which contains gypsum (68.0 wt%) and anhydrite (19.9 wt%), was used to adjust sulfate content. The content of the sulfate carrier was calculated as an equivalent anhydrite content based on the molar weights and designated as $\text{C}\bar{\text{S}}$. The mixture design is summarized in Table A1. The particle size distribution of the materials used determined by laser diffraction is depicted in Fig. 1. The calcined kaolinite content of the calcined clays was measured and calculated as described in [40] and is given in Table 2 together with the SSA determined by BET method [41] and the D_{50} value from laser diffraction. Additionally, the evolved heat during 72 h (R^3 calorimetry

Table 2
Properties of the materials used.

	PLC	μ LS	CC23	CC41	CC69	CC82
Calcined kaolinite [wt%]	–	–	23.2	41.4	68.9	81.5
SSA [m^2/g]	1.8	5.4	6.6	7.9	42.4	20.4
D_{50} [μm]	13.8	2.3	10.7	10.0	12.1	3.6
R^3 evolved heat (72 h) [J/ g_{SCM}]	–	–	251	454	666	853
Al sol. [mmol/L]	–	–	2.3	4.0	8.5	11.3
Si sol. [mmol/L]	–	–	3.3	5.0	11.4	13.2

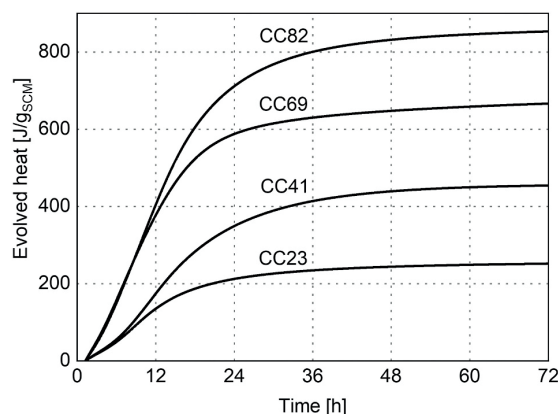


Fig. 2. Heat development during 72 h R^3 test of the investigated calcined clays.

test [42]) and solubility of Al and Si ions after elution for 20 h in 10% NaOH solution [43] is provided. The heat development during R^3 test is presented in Fig. 2. The mineralogical composition of the raw clays is presented in Table A2.

2.1. Zeta potential

In order to provide information on the surface charge of the calcined clays and the μ LS, their zeta potentials were determined in saturated portlandite solutions. The powders were suspended manually at a solid content of 50 wt% and measured over a time range of 5 min with about two measurements per minute. The zeta potential was calculated from the colloidal vibration current (CVI), which was determined by electroacoustic measurements using a DT-310 spectrometer (Dispersion Technology Instruments). Calibration was performed with a 10 wt% colloidal silica (LUDOX silica) suspension in 0.01 KCl. Titration experiments were carried out on selected samples in order to investigate adsorption of Ca^{2+} and SO_4^{2-} on the particle surfaces. For this purpose, the powders were dispersed in saturated portlandite solution ($\text{pH} = 12.7$) at a solid content of 25 wt% and stirred by a magnetic stirrer. An aqueous 1M CaCl_2 solution was added stepwise with an automatic titration system while the CVI was measured after every titration. Saturation was indicated when the values for zeta potential reached a plateau [34]. The pH was monitored and kept constant by dropwise addition of 1 M KOH solution. For the investigation of SO_4^{2-} adsorption, an amount of 10 mg CaCl_2 per g of solid was dissolved in the portlandite solution. This is the amount at which Ca saturation has been reached in all systems. A 1M Na_2SO_4 solution was then titrated analogously at constant pH.

2.2. Scanning electron microscopy

Particle morphology of the calcined clays and the μ LS was investigated in a scanning electron microscope. The samples were sprinkled as dry powder on adhesive carbon tabs and coated with gold (12 nm). An EVO® LS 15 microscope (Zeiss) was used to take secondary electron images at an acceleration voltage of 20 kV and a working distance, which was slightly varied between 7.5 and 9 mm, depending on the optimal focus of the respective sample.

2.3. Isothermal calorimetry

Heat flow of the reference system and the blended systems was measured in a TAM Air isothermal calorimeter at 25 °C during the first 48 h of hydration. The weighed starting materials were equilibrated at 25 °C for at least 12 h. The dry powders were homogenized for 30 s before water addition. The paste was prepared manually and approx. 3 g of the sample were placed in a calorimeter flask, which was inserted into the calorimeter within 2 min after water addition. A mixture of 2 g of quartz sand and 1 g of deionized water was used as reference. Heat flow was normalized to 1 g of the used Portland limestone cement. The full width at half maximum (FWHM) of the aluminate peak was determined using a peak deconvolution approach by a least-squares fitting routine in the software Fityk [44]. In this way the aluminate peak could be decoupled from the silicate peak. The peak shape was fitted most adequately by a symmetrical Pearson VII function. Integration of the heat flow over time yielded the cumulative heat, which was multiplied by 3.6 to adjust the unit to $\text{J}/\text{g}_{\text{cement}}$.

2.4. In situ X-ray diffraction

The phase development during the first 48 h of hydration was followed by in situ X-ray diffraction. Pastes were prepared analogously to Section 2.3 and transferred into a sample holder, which was covered by a 12 μm Kapton film in order to prevent water evaporation from the sample. The temperature controlled sample stage was set to 25 °C. The measurement was started within 4 min after water addition at 40 kV and 40 mA, collecting four scans from 6 to 40° 2 θ per hour in a PANalytical Empyrean diffractometer (CuK α , Bragg–BrentanoHD monochromator, PIXcel^{1D} linear detector). Rietveld refinement was performed for each diffraction pattern using Profex-BGMN [45]. The applied structures are provided in Table 3. The pattern of the Kapton film was retrieved from a scan of a silicon single-crystal sample carrier covered with the film [46]. The external standard method was applied in order to obtain the absolute mass fractions of the crystalline phases [47,48]. The retrieved

Table 3
Crystal structures used for Rietveld refinement.

Structure	Reference
Alite	[52]
Belite	[53]
$\text{C}_3\text{A}_{\text{cubic}}$	[54]
Calcite	[55]
Gypsum	[56]
Anhydrite	[57]
Ettringite	[58]
Hemicarboaluminate	[59]
Portlandite	[60]

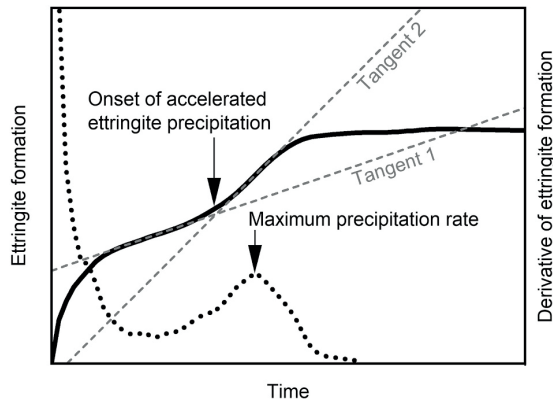


Fig. 3. Determination of the onset point of accelerated ettringite precipitation based on the development of ettringite content (solid line) and its derivative (dotted line).

quantities were partly corrected using theoretical considerations. The ettringite quantities were normalized to the theoretical maximum ettringite content based on the sulfate content of the PLC according to [49]. The starting values of alite were set to the value retrieved from the analysis of the dry cement and recalculated based on the used water-binder value, considering that the initial alite dissolution is below the standard deviation of quantitative in situ XRD results [50]. The degree of alite hydration was calculated based on the data gained from in situ quantification, smoothed by a FFT filter. The onset of the second accelerated ettringite formation was determined using the intersection of two tangents applied to the phase formation curve as described in Fig. 3. Calculation of evolved heat over a certain time was performed in order to compare results from XRD and isothermal calorimetry, using the enthalpies of reaction as provided in [51].

3. Results and discussion

3.1. Particle characteristics

3.1.1. Zeta potential

Zeta potentials of the calcined clays and the μ LS, dispersed in saturated portlandite solution are provided in Table 4. The zeta potential represents the electric potential at the shear plane between Stern layer and the diffuse layer of a particle in suspension [37,61]. While the calcined clays reveal strong negative values, with the strongest for CC69, the μ LS shows a low positive value. It is well established, that calcined clay minerals exhibit negative surface charges, both in pure water and alkaline solutions [34,62]. These negatively charged surfaces are known to adsorb huge amounts of dissolved Ca^{2+} [33–35]. Even though CC69 and CC82 possess the same amount of clay minerals, CC69 shows nearly twice the zeta potential of CC82, which might be attributed to the higher SSA and degree of disorder (Table A2).

The courses of the zeta potential of CC82, CC69 and μ LS in saturated portlandite solution with continuous CaCl_2 addition (Fig. 4a) allow conclusions on their adsorption behavior. μ LS starts at a low positive zeta potential (6.5 mV) and shows – after an initial drop – only a small increase with the addition of Ca^{2+} in the beginning, followed by a slight decrease at higher Ca^{2+} concentrations. Other authors report an initially negative zeta potential for calcite in alkaline solution, which rapidly increases with the amount of Ca^{2+} added [35,63]. The Ca^{2+} provided in

Table 4

Zeta potential of the SCMs dispersed in saturated portlandite solution at a solid content of 50 wt%.

	Zeta potential [mV]
μ LS	$+6.5 \pm 0.1$
CC23	-25.7 ± 0.6
CC41	-22.9 ± 0.5
CC69	-39.2 ± 0.4
CC82	-24.3 ± 0.4

the portlandite solution, which corresponds to 0.31 mg/g_{solid}, apparently is enough to lead to a saturation of the calcite surface, in a way that the zeta potential is hardly altered by further addition of CaCl_2 . This corresponds with observations of a rapid increase of an initially positive zeta potential of calcite suspensions due to the addition of $\text{Ca}(\text{OH})_2$, quickly leading to a saturation of the surfaces [37]. CC69 and CC82 indicate a strong dependence on the Ca^{2+} concentration, with both reaching a plateau at around 10 mg/g_{solid} Ca^{2+} . CC69 however reveals a more significant change of the initially stronger negative zeta potential during the same period and amount of Ca^{2+} added, as the stronger negatively charged surface leads to a stronger interaction with dissolved cations.

The influence of SO_4^{2-} on the zeta potential (Fig. 4b) was investigated in conditions, where the particle surfaces are assumed to be saturated by Ca^{2+} , which is estimated at a Ca^{2+} content of 10 mg/g_{solid} (dotted vertical line in Fig. 4a). All three samples are certainly influenced by the SO_4^{2-} concentration, indicated by an increasingly negative zeta potential with increasing SO_4^{2-} concentration. Pourchet et al. [37] also observed a significant decrease of the zeta potential of calcite with increasing SO_4^{2-} concentration, however, they quantified the amount of adsorbed sulfate to only a seventh of the adsorbed calcium at a similar relative change of zeta potential. This admonishes us not to draw quantitative conclusions from these measurements, especially since they could not be simply transferred to cementitious systems. Similar observations were made regarding the influence of sulfate on dispersed blast furnace slag and led back to formation of a positively charged Ca^{2+} layer, building up the first Stern layer, which attracted SO_4^{2-} in a second Stern layer [38]. Further, it was stated in another work [36] that an adsorption of SO_4^{2-} onto the Ca^{2+} layer on the surface of calcined clays can cause a strong acceleration of the C_3A hydration by accelerating the depletion of solid CS . This mechanism is further discussed in Section 3.2.2.

3.1.2. Particle morphology

The clay size fraction ($< 2 \mu\text{m}$) is usually underdetermined by laser diffraction due to the platy shape of clay minerals [64]. This fact however only partly explains the high discrepancy between the SSA and the particle size distribution of the calcined clays. In order to interpret the values of SSA, particle size distribution (Table 2) and their influence on early hydration correctly, the particle morphology was investigated using SEM. The μ LS (Fig. 5a) is characterized by scattered particles with compact grain shape in the range of 200 nm up to 5 μm . The calcined clay particles (Fig. 5b–d) tend to form larger agglomerations. This is most apparent for CC69 (Fig. 5c), where small platy particles with a size in the range of 100–600 nm form large agglomerations of several μm . The kaolinite agglomerations in CC82 and CC41 are smaller compared to CC69, while the primary particles are significantly larger. The morphology of the different types of SCM suggests a different impact on cement paste properties. Even though the depicted calcined clays provide a significantly higher SSA determined by nitrogen adsorption than

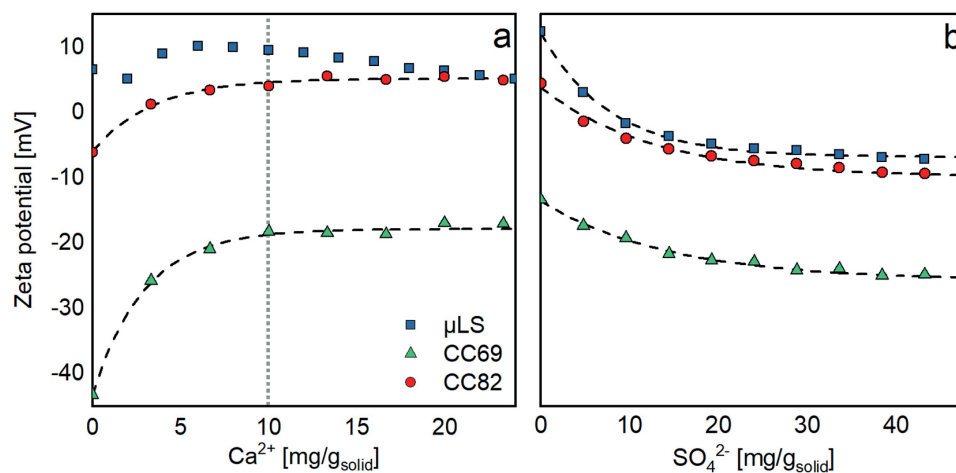


Fig. 4. Development of zeta potential of CC69 (pH = 12.0), CC82 (pH = 12.2) and μLS (pH = 12.5) in saturated portlandite solution at a solid content of 25 wt% (a) depending on the Ca^{2+} concentration and (b) with initially added CaCl_2 (10 mg Ca^{2+} /g_{solid}) depending on the SO_4^{2-} concentration.

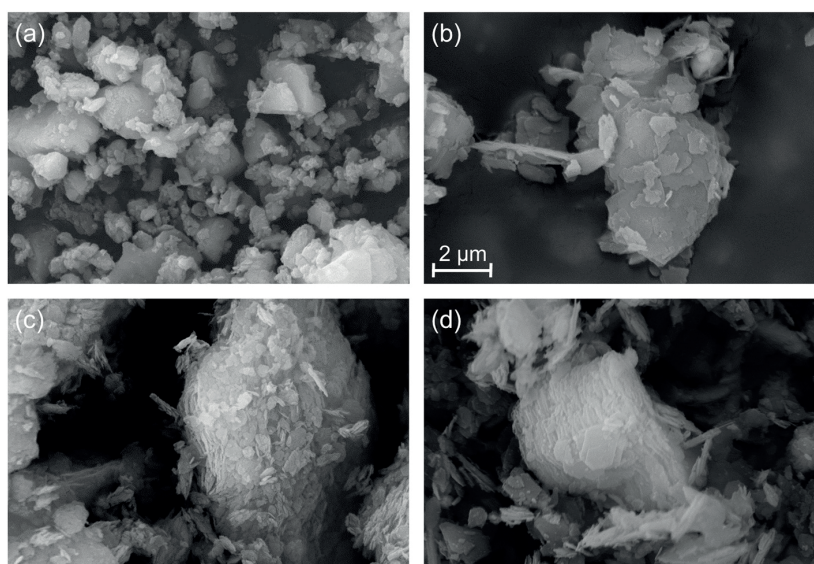


Fig. 5. SEM images of a) μLS , b) CC82, c) CC69 and d) CC41 (the scale in (b) holds for all images).

the μLS , the SEM images indicate a larger surface area usable as nucleation site for hydrate phases in the case of the μLS . This results from the fact, that a large part of the SSA of the calcined clays is attributed to their inner surface [65].

3.2. Impact on the early hydration

3.2.1. Early heat flow

The different SCMs used here alter the hydration of the PLC in very different ways (Fig. 6a). The reference (PLC) reveals a heat flow curve that shows two clearly separated peaks, with the silicate peak occurring at 11.6 h and the aluminate (sulfate depletion peak) at 17.4 h, indicating a properly sulfated system [25]. CC23, which represents the calcined

clay with the lowest metakaolin content and SSA, influences the silicate reaction only marginally. The heat flow during initial and induction period is just slightly enhanced, while the aluminate peak is clearly accelerated from 17.4 h to 12.8 h. With higher calcined kaolinite content and SSA, the sulfate depletion and the acceleration period of the silicate reaction occur at earlier times [11]. PLC_CC69 and PLC_CC82 exhibit the typical heat flow curve of undersulfated systems, as the silicate and aluminate peak are strongly overlapped [25]. The course of the heat flow of PLC_ μLS differs from that of the calcined clays. While the initial heat flow – as far as recorded – is in the range of the calcined clay blended systems with comparable SSA, the onset of the silicate reaction appears significantly earlier as compared to the calcined clay systems, while the acceleration of the aluminate peak is slightly lower compared

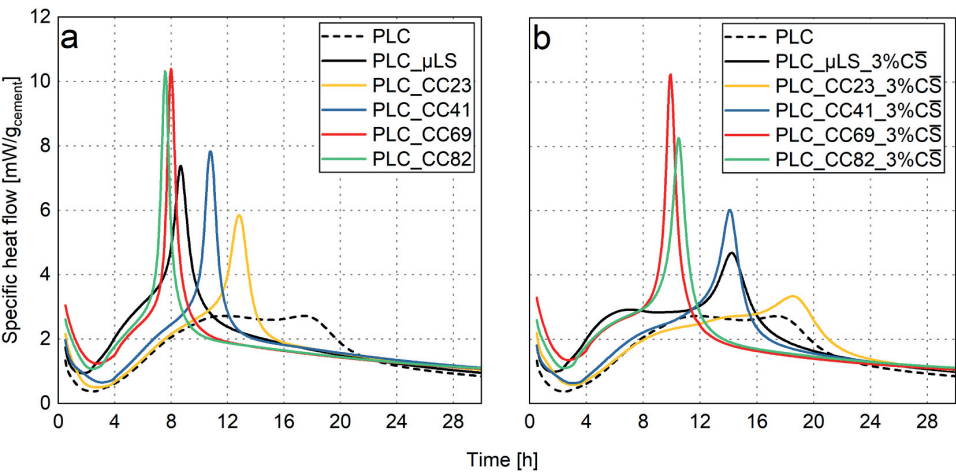


Fig. 6. Heat flow curves of PLC blended with 30 wt% μ LS and calcined clays (a) without sulfate addition and (b) with sulfate adjustment to 3 wt% CŠ.

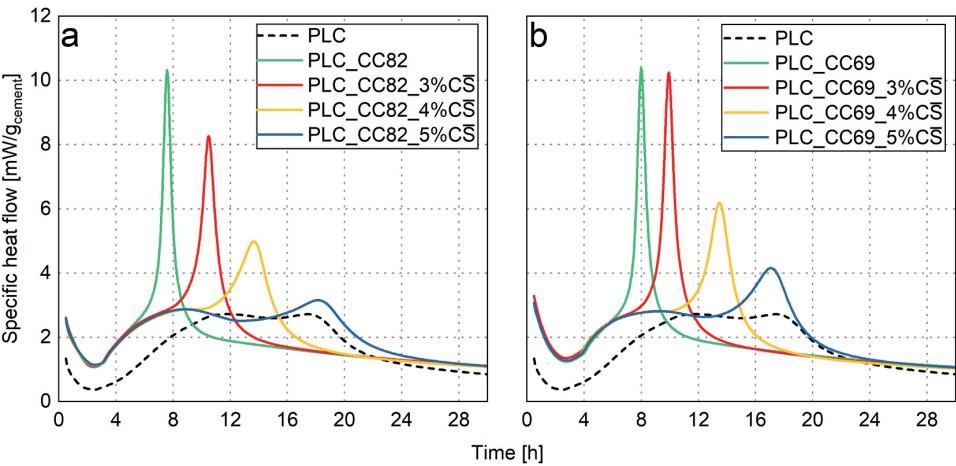


Fig. 7. Sulfate adjustment in the systems (a) PLC_CC82 and (b) PLC_CC69.

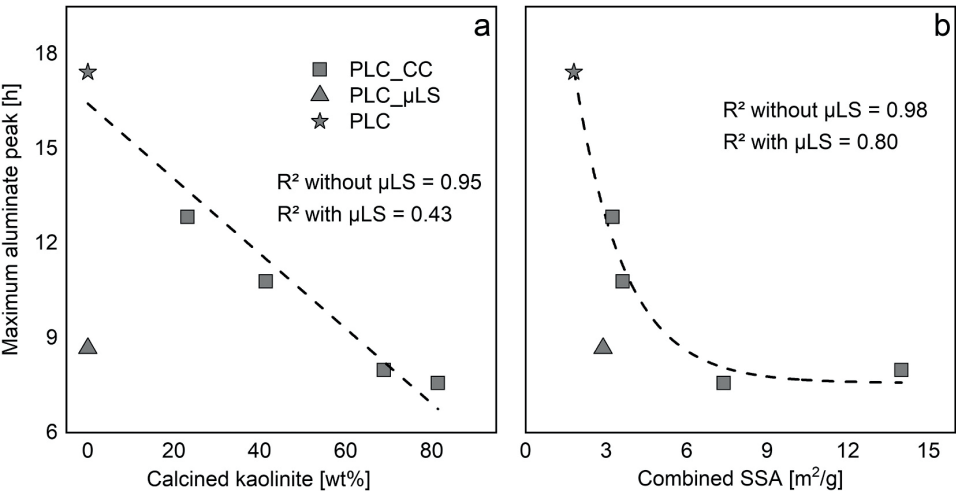


Fig. 8. Influence of calcined kaolinite content (a) and combined specific surface area (b) on the position of the aluminate heat flow maximum.

to CC69 and CC82. Still, there is a clear overlap of silicate and aluminate peak, indicating an undersulfated system, due to the higher sulfate demand caused by the filler effect [29]. The addition of sulfate does affect neither the initial heat flow nor the silicate peak but shifts the aluminate peak to a later point (Fig. 6). This shift however differs significantly between the systems with calcined clays and PLC_μLS. Regarding the latter, an overall C \bar{S} content of 3 wt% is enough to reach a proper sulfation, characterized by two separated heat flow peaks (Fig. 6b). The two calcined kaolinitic clays instead still show a strong overlap of the aluminate and silicate reaction at 3 wt% C \bar{S} . While in the system without additional sulfate, the sulfate depletion peak of PLC_μLS occurs clearly before the one of PLC_CC41, they occur at the same time in the system with 3 wt% C \bar{S} . Furthermore, the aluminate peak of the calcined clay blends appears to be higher and narrower, compared to the μLS blend. These facts reveal a difference in the behavior and mechanisms with respect to sulfate consumption between the systems with calcined clays and the one with μLS. Additionally, since the silicate peak appears later for the calcined clay blended systems, compared to the μLS system, a proper sulfation also means that the aluminate peak has to appear at a later point.

The two metakaolin-rich systems need an overall C \bar{S} content of 5 wt % to separate into two distinctive heat flow peaks (Fig. 7). Initial (as far as recorded), induction and acceleration period are unaffected by the sulfate content. Despite a lower calcined kaolinite content, PLC_CC69 demands a slightly higher sulfate addition for a comparable position of the aluminate peak as PLC_CC82. Moreover, the aluminate peak appears higher and narrower for PLC_CC69 at identical sulfate content.

3.2.2. Factors influencing the position of the aluminate peak

The position of the aluminate heat flow peak in pure cement pastes or model cement is influenced by the amount of sulfate in the system [66] and the amount of precipitated C-S-H and ettringite before sulfate depletion [28,30], which depends on cement composition and fineness. The calcined kaolinite content of the SCM (Fig. 8a) and the calculated combined SSA of the blended system (Fig. 8b) seem to correlate well with the heat flow maximum of the aluminate peak in the systems without extra sulfate addition, if only the reference and the calcined clay blended systems are taken into account. The calcined kaolinite content also correlates well with the evolved heat during 72 h of R³ reactivity test, which is given in Table 2, as already observed in previous studies [40,67]. The influence of the surface area on the position of the aluminate peak has been explained by an enhanced C-S-H formation, driven by the filler effect, leading to more sulfate being adsorbed onto C-S-H [29]. The same authors reported stronger acceleration of the aluminate peak by limestone compared to metakaolin and led it back to the preferred surface for C-S-H nucleation. Limestone is known to be more effective in accelerating the cement hydration than other fillers, e. g. quartz, since it provides a preferred surface for nucleation of C-S-H [16–18,68]. Fig. 8b corroborates these observations as the μLS accelerates the aluminate reaction stronger than the calcined clays with comparable surface area, confirming previous results, which refuted a correlation between alumina content of the SCM and sulfate demand [29]. Furthermore, it is derivable from Fig. 6, that the silicate reaction is significantly enhanced in PLC_μLS, compared to all systems with calcined clay – independent of the SSA of the system.

However, looking solely at the SSA, the effects of the calcined clays on the silicate reaction would be still expected to be stronger. An inhibiting factor regarding the silicate reaction could be a higher aluminum concentration in the pore solution of the calcined clay blended systems, as aluminum is well known to slow down C₃S

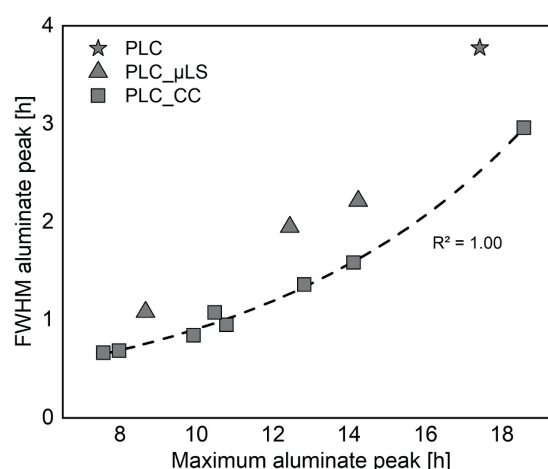


Fig. 9. Correlation of the position of the aluminate heat flow maximum with the full width at half maximum (FWHM) of the aluminate peak for the different systems with different sulfate additions provided in Fig. 6 and additionally the system PLC_μLS 2.66% C \bar{S} .

dissolution [69]. Another, in the view of the authors, crucial reason becomes clear from the SEM images (Fig. 5). The calcined kaolinite particles in CC82 tend to agglomerate to stacks of a size of several μm. This effect is even stronger for CC69, which exhibits a significantly higher SSA but a coarser PSD and where the small calcined kaolinite platelets tend to form large, spherical agglomerates of up to 10 μm. This causes a large inner surface of the particles. The inner surface seems to be, at least partly, accessible for adsorption of N₂ during BET measurements as well as for ions from the cement pore solution (Fig. 4). The strong agglomeration of the single calcined clay mineral particles weakens the filler effect, especially the accelerated clinker dissolution and the nucleation effect, as the inner surface area of the agglomerated particles is not available as nucleation site. The interparticle distance in the calcined clay blended cements is decreased to a lower amount as compared to the PLC_μLS, due to the scattered μLS particles. This is indicated by the PSD of the calcined clays, which is significantly coarser as their SSA would suggest based on the data of the μLS. From this point of view, it is remarkable, that PLC_CC69 and PLC_CC82 still reveal a stronger acceleration of the aluminate peak compared to PLC_μLS, while the silicate peak seems to be less enhanced (Fig. 6). A possible explanation for this effect could be additional adsorption of sulfate onto the surface of the calcined clays, as already derived from experiments in C₃A-C \bar{S} model systems [36]. The zeta potential measurements in presence of Ca²⁺ and in dependence of SO₄²⁻ reveal such adsorption effects on the μLS as well as on the calcined clays. However, the high, Ca-saturated surface area of the calcined clays seems to be host for more SO₄²⁻ as the μLS and thus a stronger accelerator of the aluminate reaction.

3.2.3. Factors influencing the shape of the aluminate peak

While the aluminate heat flow peak appears later with increasing sulfate content of the system, this usually goes along with an increase of peak width. This has been reported for C₃A-C \bar{S} model systems [36,66] as well as real composite cements [70] and can be seen in Fig. 7. Besides the different impact on the position of the aluminate peak, the μLS and

the calcined clays investigated in this study also modify the peak shape in a differentiated manner. This can be derived from the correlation of the peak position and the peak's FWHM for the different systems with varied sulfate additions (Fig. 9 and Table A3). Even if the aluminate peak in a calcined clay blended system appears at a similar position as the reference or the μ LS blended system, it reveals a significantly narrower shape. We can consider three possible mechanisms as driving forces for this increased heat evolution rate during the aluminate peak:

1. Calcined clays could serve as a preferred nucleation area for ettringite and therefore promote its precipitation after sulfate depletion. This is to some extent supported by observations in [36], but is not considered as the dominant mechanism here, as there is already enough ettringite present at this point to serve as nucleation area for further precipitation.
2. According to Jansen et al. [27], the fast increase of aluminum concentration in the pore solution after sulfate depletion is the trigger for the increased ettringite precipitation rate. A release of Al ions by the metakaolin could further increase Al concentration at the point of sulfate depletion and in this way contribute to the accelerated ettringite formation, which increases the rate of heat development. Since the role of aluminum from the metakaolin is minor at this point in early hydration, as previously reported [29] and verified in the present findings, this effect is considered to be minor.
3. The sharpness of the peak could be influenced by the host of the sulfate ions. Possibly, the SO_4^{2-} is attached stronger to the C-S-H as to other surfaces (e.g. calcined clays), and therefore is released at a lower rate after sulfate depletion. This is supported by the data presented in Section 3.3.1, as the progress of silicate reaction at sulfate depletion is higher in the reference and the μ LS system compared to the calcined clay blended systems and therefore more

sulfate can be adsorbed by C-S-H. While this mechanism can explain the observations most evidently, it needs to be verified in further investigations.

3.3. Hydrate phase formation

3.3.1. Alite hydration

The phase development of the clinker phases and the crystalline hydration products were derived from the quantitative in situ XRD

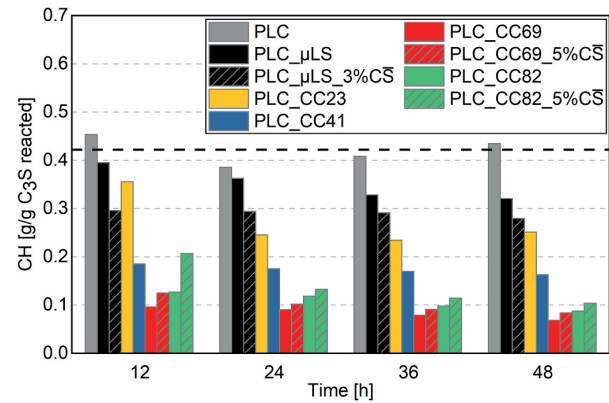


Fig. 11. Portlandite content normalized on the C_3S hydration degree for all investigated systems after 12, 24, 36 and 48 h. The dashed line represents the theoretical value [50].

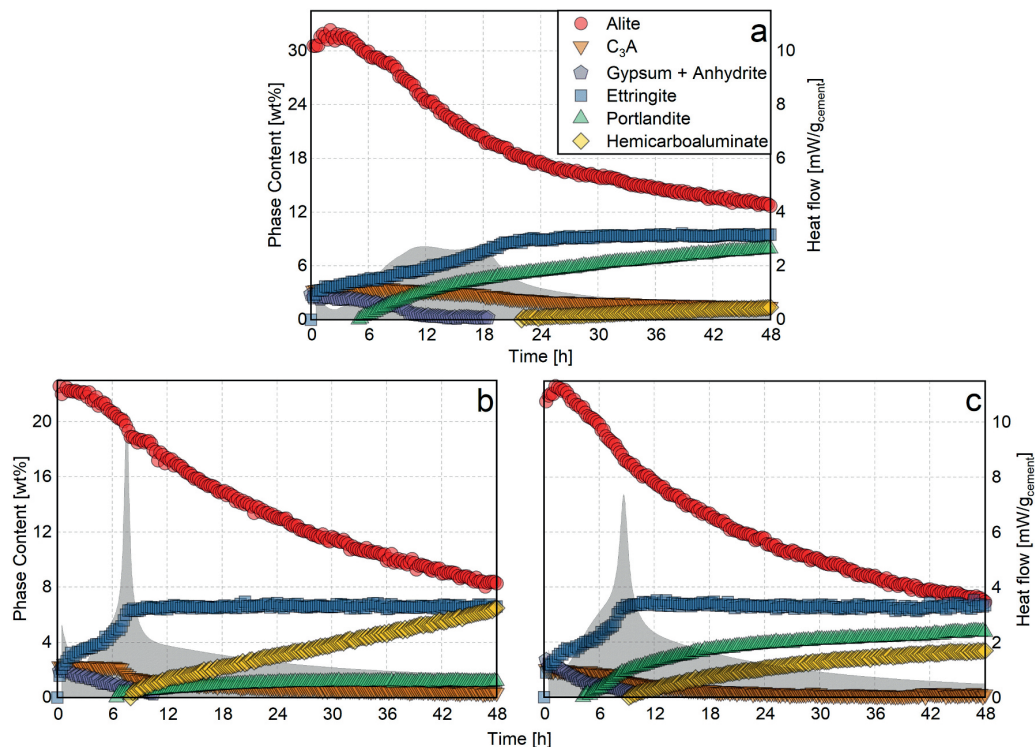


Fig. 10. In situ XRD results of (a) PLC, (b) PLC_CC82 and (c) PLC_μLS. Note the different scale on the left y-axis of the upper diagram (a), due to the higher initial amount of clinker phases. The error is below ± 1.5 wt% for alite, ± 1.0 for ettringite and ± 0.5 wt% for other phases.

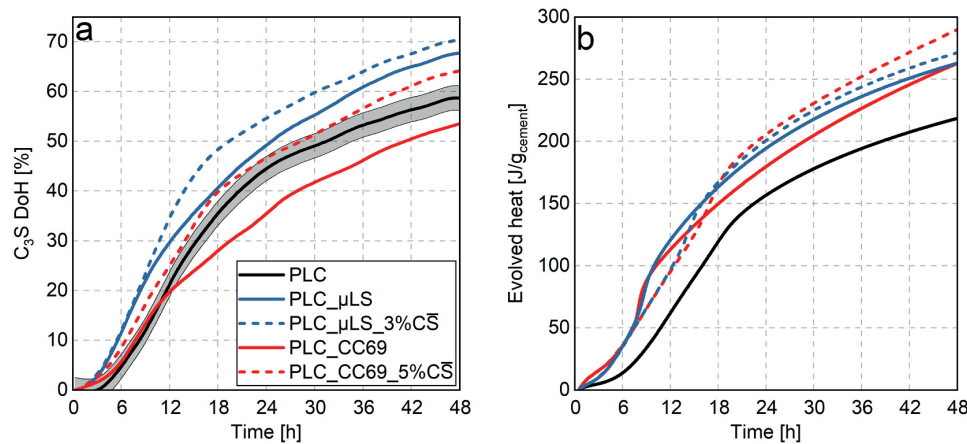


Fig. 12. Influence of the sulfate content on (a) the degree of alite hydration (C₃S DoH) and (b) the evolved heat for PLC, PLC_μLS and PLC_CC69 during the first 48 h.

measurements. The results for the systems PLC, PLC_CC82 and PLC_μLS are presented in Fig. 10, while all quantified systems can be found in Fig. A1. The influence of the calcined clays on the early alite hydration, which is detected by isothermal calorimetry (Fig. 6) appears to be minor compared to the μLS, which causes a significant acceleration already during the first hours. This is in line with the enhanced filler effect of limestone described in Section 3.2.2.

Portlandite formation therefore already sets in after 4.5 h for PLC_μLS compared to 6.5 h for PLC_CC82. The portlandite content of the calcined clay blended systems, especially at a high calcined kaolinite content, is significantly reduced compared to PLC and PLC_μLS during the first 48 h. From this observation, a pozzolanic contribution of the calcined clays, after 6 h at the latest can be assumed. This becomes more obvious from Fig. 11, where the portlandite content is normalized to the hydration degree of C₃S. With the dissolution of 1 mol C₃S theoretically 1.3 mol of portlandite precipitate [50]. Thus, every gram of C₃S can form 0.42 g of portlandite, as indicated by the dashed line in Fig. 11. This value is approximately reached by the PLC throughout the first 48 h. The

portlandite consumption of the calcined clays increases with their calcined kaolinite content. Naber et al. [39] could show in a metakaolin blended cement that 26 wt% of the calcined kaolinite has reacted within one day, while its reaction in ternary blends containing limestone is assumed to be further enhanced [6], indicating that the presented amount of portlandite consumption is quite conceivable. Apparently, even though the calcined kaolinite content and the chemical reactivity determined by R³ test after 72 h (Table 2) is lower for CC69 compared to CC82, its portlandite consumption is about the same or even slightly higher. These observations, however, are in line with the similar heat development of CC69 and CC82 during the first 10 h of R³ test (Fig. 2). This could be drawn back to the higher SSA and degree of disorder (provided in Table A1) in the raw kaolinite of CC69, which both cause faster reaction kinetics [40]. Possible differences in the Ca/Si ratio of the C-S-H could also cause differences regarding the amount of consumed portlandite between the different systems. Another explanation might be adsorption of Ca²⁺ onto the surfaces of the calcined clays, which was also assumed to accelerate portlandite consumption in clinker free

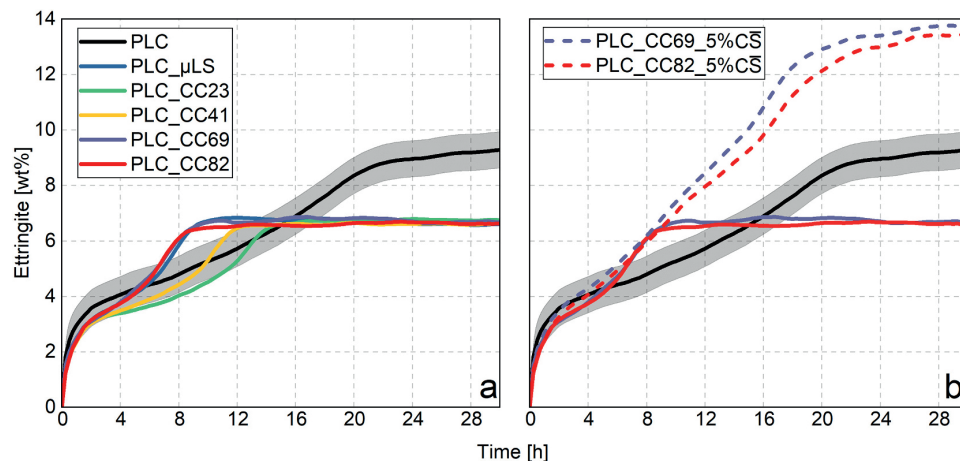


Fig. 13. a) Ettringite formation during the first 30 h in the systems without sulfate adjustment and b) the influence of adequate sulfation on the ettringite formation in the metakaolin-rich systems.

M. Maier et al.

Cement and Concrete Research 154 (2022) 106736

systems [23]. The stronger interaction with Ca^{2+} of CC69 compared to CC82 is in line with the slightly higher portlandite consumption in PLC_{CC69}. The sulfate content only marginally influences the consumption of portlandite during the first 48 h for most systems investigated. Even though there are some significant differences in the systems PLC_{μLS} and PLC_{CC82} after 12 h, these are becoming smaller in the further course of hydration.

The impact of undersulfation on the silicate reaction is most evident for the system PLC_{CC69} (Fig. 12a). After the sulfate depletion at around 8 h, there is an obvious kink in the C_3S reaction curve and the reaction rate is significantly reduced from this point onwards. The adequately sulfated system PLC_{CC69_5%CS} reveals a clear increase in the degree of alite hydration of approx. 20% after 48 h. In the system PLC_{μLS}, the correct sulfation only slightly enhances the degree of hydration after 48 h, while the effect is most dominant between 9 and 15 h. This represents the time after sulfate depletion, where the silicate reaction is superimposed by the aluminate reaction in the undersulfated system. These observations correspond well with findings by Bergold et al. [71], who investigated a synthetic cement at different sulfate contents and proved a strong interference of the silicate reaction at the point of renewed C_3A dissolution.

The findings are supported by the hydration heat of the respective systems (Fig. 12b), which, however, depicts the aluminate reaction as well. Nevertheless, the differentiated influence of the sulfate content on the reaction rate can be also deduced from the hydration heat. The overall higher hydration heat of the system PLC_{CC69_5%CS} compared to PLC_{μLS_3%CS} can be attributed to a stronger aluminate reaction in the calcined clay blended system. The results at hand emphasize the importance of a correct sulfation of blended cements concerning a clear separation of the aluminate and silicate heat flow peaks in order to impede interference of both reactions.

3.3.2. Aluminate reaction

Ettringite formation in the blended systems without sulfate adjustment (Fig. 13a) proceeds at three different rates. The fast initial precipitation is similar in all systems and almost reaches the amount, which is determined for the reference system. Thus, the amount per gram of cement is significantly higher in the blended systems. As the difference between the single blended systems is marginal, despite significant differences in the physical and chemical properties of the used SCM, particularly their alumina content, the dilution effect seems to be the driving force for the enhanced ettringite formation. This can be explained by a higher water-to-clinker ratio, which enhances the initial C_3A dissolution. A potential influence of aluminum released by the calcined kaolinite seems to be negligible at this very early point of time. The pozzolanic contribution of the calcined clays through the release of Al ions only takes place after the precipitation of portlandite, which is needed as reaction partner to form ettringite (Fig. 11). In the undersulfated systems, this point is reached close to the sulfate depletion peak, so the influence of ettringite, which incorporates Al from the calcined kaolinite, on the sulfate balance is negligible. A significant difference in the precipitation rate only sets in with the renewed ettringite formation as a consequence of sulfate depletion. Accelerated ettringite formation is observable when an increased C_3A dissolution takes place, which is the case during the initial period and at sulfate depletion. An increased C_3A reaction rate increases the amount of ettringite formed and therefore impacts the sulfate balance [28]. Jansen et al. [27] observed the fast increase in aluminum concentration after sulfate depletion to be the trigger for enhanced ettringite precipitation. In this case, a further increase of the aluminum concentration through metakaolin dissolution

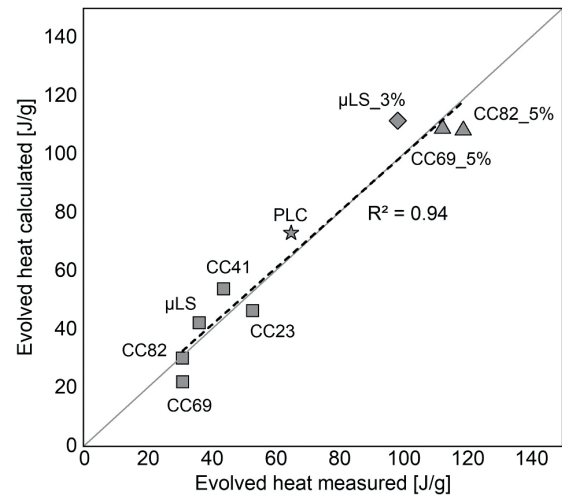


Fig. 14. Evolved heat between 0.5 h and the onset point of enhanced ettringite formation at sulfate depletion. Data on the x-axis is calculated based on the measured heat flow. Data on the y-axis is calculated from the C_3S and ettringite phase content, based on the reaction enthalpies.

could contribute to enhance the ettringite precipitation rate, as described in Section 3.2.3, while the driving force for the increase in aluminum concentration can be attributed to the renewed C_3A dissolution. The effect of sulfate adjustment on the ettringite formation in the systems with the metakaolin-rich calcined clays is shown in Fig. 13b. Apparently, the sulfate content has a minor impact on the amount of

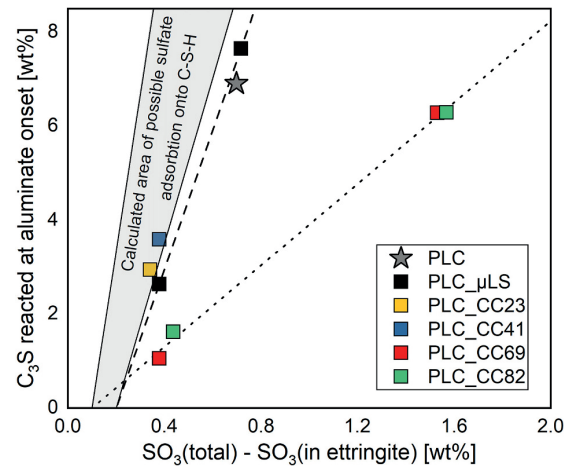


Fig. 15. Correlation of SO_3 content (taking into account the SO_3 bound by ettringite) and amount of reacted C_3S at the onset of accelerated ettringite precipitation. The light grey shaded area represents the theoretical amount of adsorbed sulfate onto C-S-H based on a S/Ca ratio of 0.04–0.06 [28] and a composition of $\text{C}_{1.7}\text{SH}_{2.6-4.0}$ [71,72]. The dashed line extrapolates the connecting line of the PLC_{μLS} systems; the dotted line shows a linear fit through the PLC_{CC69} and PLC_{CC82} systems.

precipitated ettringite during the first 8 h, as already indicated by the heat flow in Fig. 7. It just leads to a more constant precipitation rate and a continued formation after 8 h. Thus, it can be stated, that not the amount of ettringite formed until this point is the factor that impedes the silicate reaction but rather the renewed C_3A dissolution, which increases the aluminum concentration in the pore solution.

The onset of the second accelerated ettringite formation at sulfate depletion was determined for the different systems as described in Fig. 3. The released heat between 0.5 h and the second ettringite onset, determined for each system, is plotted on the x-axis of the diagram in Fig. 14. The same parameter was calculated based on the enthalpies of reaction using the phase development between 0.5 h and the second ettringite onset. The results retrieved by both methods correlate well along the 1:1 line. The amount of evolved heat until second ettringite onset differs significantly between the different systems. All blended systems show a lower amount of evolved heat compared to the PLC. If sulfate adsorption occurred exclusively on C-S-H, all systems with similar sulfate content would show the second ettringite onset after a comparable amount of released heat, considering the fact that initial ettringite formation is similar for all blended systems.

The calcined clays with the highest amount of metakaolin and largest surface area (CC82 and CC69) reveal sulfate depletion at the lowest amount of evolved heat. This indicates that the more sulfate is adsorbed directly onto the surface of the SCM, the lesser amount of hydrate phase formation (especially C-S-H) is needed for the sulfate to deplete. It can be further noticed, that these systems yield a higher heat flow between initial and induction period (Fig. 6). This could possibly be traced back to an enhanced C_3A dissolution, as the surfaces of the SCM and the C_3A might compete for the early dissolved sulfate. However, the underlying data do not provide sufficient accuracy to verify this hypothesis. Thus, further investigations of the early C_3A dissolution in model systems are needed.

Additional evidence for a further sulfate host, apart from C-S-H and ettringite, in the metakaolin-rich systems is provided in Fig. 15. There, the remaining SO_3 content (total SO_3 of the systems minus SO_3 bound in ettringite) is correlated with the amount of C_3S reacted until onset of accelerated ettringite precipitation. The correlation reveals that PLC, CC69 and PLC, CC82 would need significantly more C-S-H for the adsorption of all sulfate left in the system than what is calculated based on the reacted C_3S (light grey shaded area). It is further shown, that the linear fits of the differently sulfated systems intersect with the x-axis at low positive values (0.1–0.2 wt%). This could be related to the sulfate dissolved in the pore solution and corresponds to measured values in the literature [11,27]. The appropriate range was therefore considered for the calculation of the grey area.

Precipitation of hemicarboaluminate sets in in all systems after maximum ettringite content is reached (Fig. A1). The precipitation rate is enhanced with higher metakaolin content, which is in line with [4]. While in the system with μ LS, the initial formation rate of hemicarboaluminate is enhanced compared to the reference, the content approaches a maximum, as the system seems to run out of aluminum ions. This is not the case for the calcined clay blended systems, where a continuous formation takes place until the end of the in situ measurements.

4. Conclusion

The presented results reveal that the acceleration of early clinker hydration by calcined clays and μ -limestone is influenced by different mechanisms and to a varying extent due to different particle properties, which also imply a different sulfate demand. The acceleration of the aluminate reaction in blended cements can be attributed most likely to three mechanisms:

1. Enhanced initial ettringite formation, mainly caused by dilution effect and possibly in combination with an enhanced initial dissolution of C_3A .
2. Adsorption of SO_4^{2-} onto newly formed hydrates (mainly C-S-H), where formation of the latter is sped up by the filler effect, confirming previous studies.
3. Direct adsorption of SO_4^{2-} onto the surface of SCMs or onto a positively charged Ca layer formed on their surface.

None of these mechanisms is directly coupled to the SCM's alumina content, confirming previous results, that the latter is not the dominant factor regarding the sulfate balance of blended cements. The filler effect of the investigated calcined clays is significantly lower compared to limestone, even if they introduce significantly more surface area. This is partly related to strong agglomeration of calcined clay platelets. The surface area of calcined clay minerals is only partially available as nucleation site, while it seems to be a strong adsorbent for ions from the pore solution. While the μ -limestone reveals a positive zeta potential in saturated portlandite solution, the calcined clays show strongly negative values. Even though, adsorption of sulfate ions occurs on all investigated SCMs, if sufficient calcium is available, the presented results indicate a higher amount of adsorbed ions in the metakaolin-rich systems. The reduction of alite hydration in the undersulfated systems, which can hinder optimal strength development, indicates its impeding by increased aluminum concentration. This proves that proper sulfation should not only be applied to prevent flash setting, but also to guarantee an unimpeded silicate reaction, indicated by two separate heat flow maxima. The amount of portlandite available for the pozzolanic reaction is not reduced by sulfate addition, since the formation of carboaluminates consumes portlandite at the same rate, during the first 48 h. Different hypotheses were discussed regarding the faster reaction rate during aluminate reaction, indicated by a sharper sulfate depletion peak, in the calcined clay blended systems. While a verification of these mechanisms should be subject of further research, a slower release of adsorbed SO_4^{2-} from the C-S-H compared to the calcined clay surface was considered to be the most reasonable mechanism. Results from quantitative in situ X-ray diffraction and isothermal calorimetry yielded good correlation regarding the reaction kinetics, as well as the calculated heat of reaction until sulfate depletion.

CRedit authorship contribution statement

Matthias Maier: conceptualization, methodology, investigation, writing-original draft preparation, writing-reviewing and editing.

Ricarda Sposito: conceptualization, investigation, writing-reviewing and editing.

Nancy Beuntner: supervision, writing-reviewing and editing.

Karl-Christian Thienel: supervision, writing-reviewing and editing.

Declaration of competing interest

The authors declare that they have no known competing financial interests or personal relationships that could have appeared to influence the work reported in this paper.

Acknowledgements

This research did not receive any specific grant from funding agencies in the public, commercial, or not-for-profit sectors. The authors would like to thank sh minerals GmbH for providing the μ -limestone, Strobel Quarzsand GmbH, Quarzwerke GmbH, Hubert Gerharz Tonbergbau GmbH, and Tongrube Degelhof for providing the raw clays, Schwenk Zement KG for the cement and HeidelbergCement AG for the sulfate carrier.

Appendix A

Table A1

Mixture design and SSA of the systems investigated.

	PLC [wt%]	SCM [wt%]	C \overline{S} [wt%] ^a	w/b [–]	SSA [m ² /g]
PLC	100	–	2.7	0.5	1.8
PLC_CC69	70	30	1.9, 3.0, 4.0, 5.0	0.5	14.0
PLC_CC82	70	30	1.9, 3.0, 4.0, 5.0	0.5	7.4
PLC_CC41	70	30	1.9, 3.0	0.5	3.6
PLC_CC23	70	30	1.9, 3.0	0.5	3.2
PLC_μLS	70	30	1.9, 3.0	0.5	2.9

^a Based on an anhydrite equivalent. The first number represents the C \overline{S} provided by the PLC. Additional C \overline{S} was added maintaining the initial PLC/SCM ratio.

Table A2

Mineralogical composition and degree of kaolinite disorder of the raw clays before calcination.

Phase [wt%]	CC23 raw	CC41 raw	CC69 raw	CC82 raw
Quartz	33.2	47.7	12.6	15.5
Kaolinite	25.7	45.0	70.6	83.9
Muscovite/illite	36.1	3.1	12.9	–
Goethite	4.3	3.3	–	–
Other	0.7	0.9	3.9	0.6
Kaolinite disorder (AGFI)	n.d.	1.24	0.54	0.85
Kaolinite disorder (P ₀)	n.d.	0.96	0.92	1.14

Table A3

Position and full width at half maximum (FWHM) of the aluminate peaks in the systems presented in Fig. 9.

	Maximum aluminate peak [h]	FWHM aluminate peak [h]
PLC	17.4	3.8
PLC_CC69	8.0	0.7
PLC_CC82	7.6	0.7
PLC_CC41	10.8	1.0
PLC_CC23	12.8	1.4
PLC_μLS	8.7	1.1
PLC_μLS_2.66%	12.4	2.0
PLC_μLS_3%	14.2	2.2
PLC_CC69_3%	9.9	0.8
PLC_CC82_3%	10.5	1.1
PLC_CC41_3%	14.1	1.6
PLC_CC23_3%	18.6	3.0

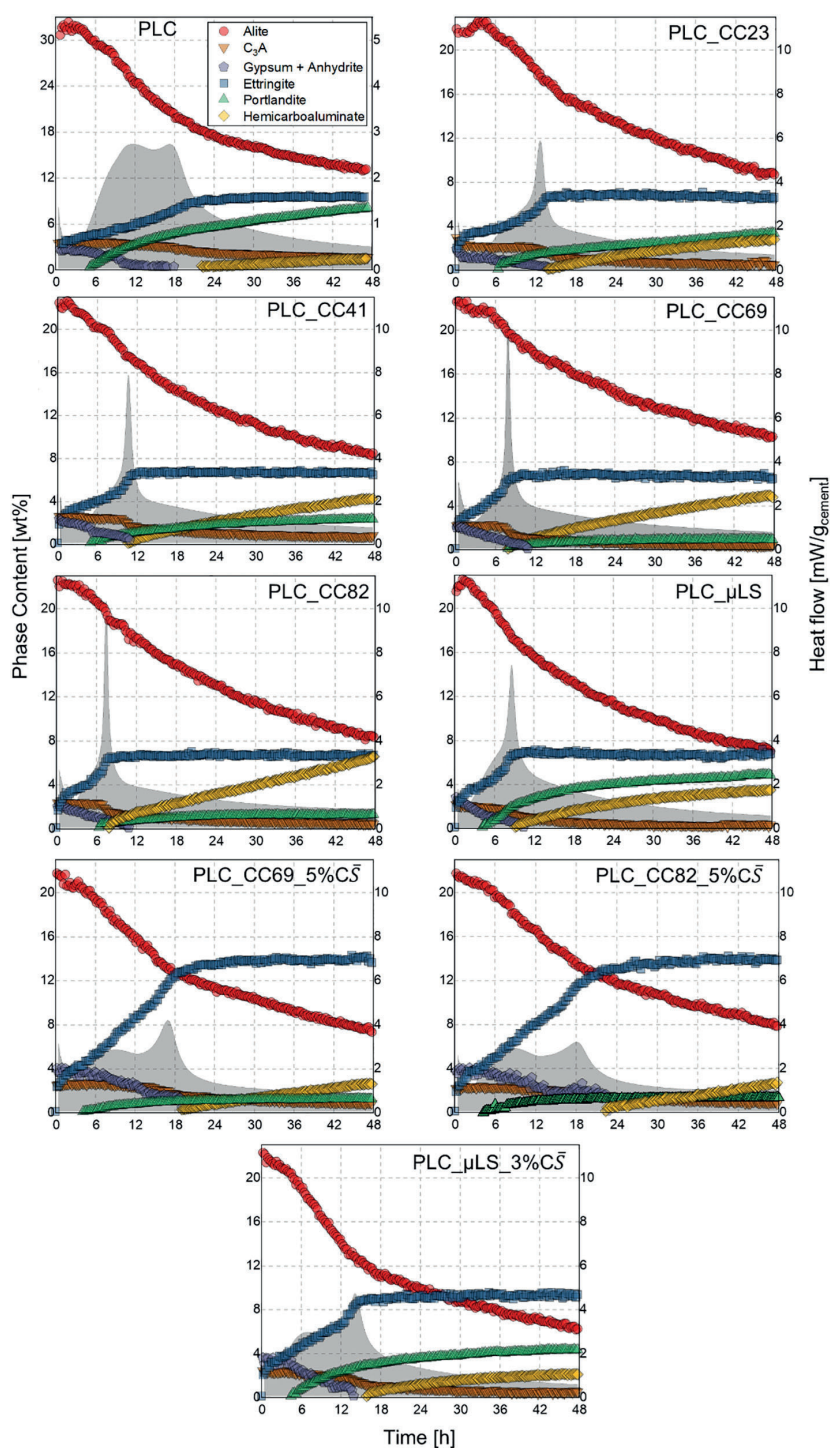


Fig. A1. XRD quantifications (left axis) and heat flow curves (right axis) of all investigated systems. The error is below ± 1.5 wt% for alite, ± 1.0 for ettringite and ± 0.5 wt% for other phases.

References

- [1] M. Schneider, The cement industry on the way to a low-carbon future, *Cem. Concr. Res.* 124 (2019), 105792.
- [2] G. Habert, et al., Environmental impacts and decarbonization strategies in the cement and concrete industries, *Nat. Rev. Earth Environ.* 1 (11) (2020) 559–573.
- [3] K. Scrivener, et al., Calcined clay limestone cements (LC3), *Cem. Concr. Res.* 114 (2018) 49–56.
- [4] F. Zunino, K. Scrivener, The reaction between metakaolin and limestone and its effect in porosity refinement and mechanical properties, *Cem. Concr. Res.* 140 (2021), 106307.
- [5] M. Sharma, et al., Limestone calcined clay cement and concrete: a state-of-the-art review, *Cem. Concr. Res.* 149 (2021), 106564.
- [6] M. Antoni, et al., Cement substitution by a combination of metakaolin and limestone, *Cem. Concr. Res.* 42 (12) (2012) 1579–1589.
- [7] R. Sposito, et al., Early hydration behavior of blended cementitious systems containing calcined clays and superplasticizer, in: J. Gemrich (Ed.), 15th International Congress on the Chemistry of Cement, Research Institute of Binding Materials Prague, Prague, Czech Republic, 2019, p. 10.
- [8] S. Scherb, et al., The early hydration of cement with the addition of calcined clay - from single phyllosilicate to clay mixture, in: H.-B. Fischer, A. Volke (Eds.), 20. Internationale Baustofftagung ibaustil, F.A. Finger-Institut für Baustoffkunde, Prof. Dr.-Ing. H.-M. Ludwig, Weimar, Germany, 2018, pp. 658–666.
- [9] R. Sposito, N. Beuntner, K.-C. Thienel, Rheology, setting and hydration of calcined clay blended cements in interaction with PCE-based superplasticisers, *Mag. Concr. Res.* 73 (15) (2021) 785–797.
- [10] F. Zunino, F. Martirena Hernández, K. Scrivener, Limestone calcined clay cements (LC3), *ACI Mater. J.* 118 (3) (2012) 49–60.
- [11] N. Beuntner, K.-C. Thienel, Pozzolanic efficiency of calcined clays in blended cements with focus on the early hydration, *Adv. Cem. Res.* (2022) 1–32 (ahead of print).
- [12] B. Lothenbach, K. Scrivener, R.D. Hooton, Supplementary cementitious materials, *Cem. Concr. Res.* 41 (12) (2011) 1244–1256.
- [13] J. Skibsted, R. Snellings, Reactivity of supplementary cementitious materials (SCMs) in cement blends, *Cem. Concr. Res.* 124 (2019), 105799.
- [14] Z. Zhang, et al., A new hydration kinetics model of composite cementitious materials, part 2: physical effect of SCMs, *J. Am. Ceram. Soc.* 103 (6) (2020) 3880–3895.
- [15] M. Cyr, P. Lawrence, E. Ringot, Mineral admixtures in mortars: quantification of the physical effects of inert materials on short-term hydration, *Cem. Concr. Res.* 35 (4) (2005) 719–730.
- [16] T. Oey, et al., The filler effect: the influence of filler content and surface area on cementitious reaction rates, *J. Am. Ceram. Soc.* 96 (6) (2013) 1978–1990.
- [17] E. Berodier, K. Scrivener, Understanding the filler effect on the nucleation and growth of C-S-H, *J. Am. Ceram. Soc.* 97 (12) (2014) 3764–3773.
- [18] D.P. Bentz, et al., Limestone and silica powder replacements for cement: early-age performance, *Cem. Concr. Compos.* 78 (2017) 43–56.
- [19] A. Kumar, et al., The filler effect: the influence of filler content and type on the hydration rate of tricalcium silicate, *J. Am. Ceram. Soc.* 100 (7) (2017) 3316–3328.
- [20] X. Ouyang, et al., Insights into the mechanisms of nucleation and growth of C-S-H on fillers, *Mater. Struct.* 50 (5) (2017) 213.
- [21] Y. Briki, et al., Impact of limestone fineness on cement hydration at early age, *Cem. Concr. Res.* 147 (2021), 106515.
- [22] S. Krishnan, A.C. Emmanuel, S. Bishnoi, Hydration and phase assemblage of ternary cements with calcined clay and limestone, *Constr. Build. Mater.* 222 (2019) 64–72.
- [23] S. Scherb, et al., Reaction kinetics during early hydration of calcined phyllosilicates in clinker-free model systems, *Cem. Concr. Res.* 143 (2021), 106382.
- [24] N. Beuntner, Zur Eignung und Wirkungsweise calcinierter Tone als reaktive Bindemittelkomponente in Zement (On the suitability and mode of action of calcined clays as reactive binder components in cement), in: Fakultät für Bauingenieurwesen und Umweltwissenschaften, Universität der Bundeswehr München, Neubiberg, 2017, p. 207.
- [25] J.d.S. Andrade Neto, A.G. De la Torre, A.P. Kirchheim, Effects of sulfates on the hydration of Portland cement – a review, *Construction and Building Materials* 279 (2021) 122428.
- [26] R.J. Myers, et al., Role of adsorption phenomena in cubic tricalcium aluminate dissolution, *Langmuir* 33 (1) (2017) 45–55.
- [27] D. Jansen, et al., The early hydration of OPC investigated by in-situ XRD, heat flow calorimetry, pore water analysis and ¹H NMR: learning about adsorbed ions from a complete mass balance approach, *Cem. Concr. Res.* 109 (2018) 230–242.
- [28] F. Zunino, K. Scrivener, Factors influencing the sulfate balance in pure phase C3S/C3A systems, *Cem. Concr. Res.* 133 (2020), 106085.
- [29] F. Zunino, K. Scrivener, The influence of the filler effect on the sulfate requirement of blended cements, *Cem. Concr. Res.* 126 (2019), 105918.
- [30] A. Quennoz, K.L. Scrivener, Interactions between alite and C3A-gypsum hydrations in model cements, *Cem. Concr. Res.* 44 (2013) 46–54.
- [31] L. Valentini, et al., In-situ XRD measurement and quantitative analysis of hydrating cement: implications for sulfate incorporation in C-S-H, *J. Am. Ceram. Soc.* 98 (4) (2015) 1259–1264.
- [32] B. Mota, T. Matschei, K. Scrivener, The influence of sodium salts and gypsum on alite hydration, *Cem. Concr. Res.* 75 (2015) 53–65.
- [33] R. Li, et al., Effectiveness of PCE superplasticizers in calcined clay blended cements, *Cem. Concr. Res.* 141 (2021), 106334.
- [34] M. Schmid, J. Plank, Interaction of individual meta clays with polycarboxylate (PCE) superplasticizers in cement investigated via dispersion, zeta potential and sorption measurements, *Appl. Clay Sci.* 207 (2021), 106092.
- [35] P. Pardo, et al., Surface properties of calcined clays and their dispersion in blended Portland cement pastes, in: 13th International Congress on the Chemistry of Cement, 2011, Madrid, Spain.
- [36] M. Maier, et al., Hydration of cubic tricalcium aluminate in the presence of calcined clays, *J. Am. Ceram. Soc.* 104 (7) (2021) 3619–3631.
- [37] S. Pourchet, et al., Chemistry of the calcite/water interface: influence of sulfate ions and consequences in terms of cohesion forces, *Cem. Concr. Res.* 52 (2013) 22–30.
- [38] A. Habbaba, J. Plank, Surface chemistry of ground granulated blast furnace slag in cement pore solution and its impact on the effectiveness of polycarboxylate superplasticizers, *J. Am. Ceram. Soc.* 95 (2) (2012) 768–775.
- [39] C. Naber, et al., The PONKCS method applied for time resolved XRD quantification of supplementary cementitious material reactivity in hydrating mixtures with ordinary Portland cement, *Constr. Build. Mater.* 214 (2019) 449–457.
- [40] M. Maier, N. Beuntner, K.-C. Thienel, Mineralogical characterization and reactivity test of common clays suitable as supplementary cementitious material, *Appl. Clay Sci.* 202 (2021), 105990.
- [41] Determination of the specific surface area of solids by gas adsorption - BET method, Beuth-Verlag, Berlin, 2003, p. 19.
- [42] ASTM C1489 - 15, in: Standard Specification for Lime Putty for Structural Purposes, ASTM International, West Conshohocken, PA, 2015, p. 2.
- [43] A. Buchwald, et al., Untersuchung zur Reaktivität von Metakaolinen für die Verwendung in Bindemittelsystemen, in: Gesellschaft Deutscher Chemiker e.V. -Jahrestagung, 2003, Munich, Germany.
- [44] M. Wojdyr, Fityk: a general-purpose peak fitting program, *Journal of Applied Crystallography* 43 (5 Part 1) (2010) 1126–1128.
- [45] N. Doebelin, R. Kleeberg, Profex: a graphical user interface for the rietveld refinement program BGMN, *J. Appl. Crystallogr.* 48 (5) (2015) 1573–1580.
- [46] S. Scherb, et al., Quantitative X-ray diffraction of free, not chemically bound water with the PONKCS method, *J. Appl. Crystallogr.* 51 (6) (2018) 1535–1543.
- [47] M.D. Raven, B.H. O'Connor, M.D. Raven, Application of the Rietveld refinement procedure in assaying powdered mixtures 3 (1988) 2–6.
- [48] D. Jansen, et al., A remastered external standard method applied to the quantification of early OPC hydration, *Cem. Concr. Res.* 41 (6) (2011) 602–608.
- [49] C. Hesse, F. Goetz-Neunhoeffer, J. Neubauer, A new approach in quantitative in-situ XRD of cement pastes: correlation of heat flow curves with early hydration reactions, *Cem. Concr. Res.* 41 (1) (2011) 123–128.
- [50] D. Jansen, et al., The hydration of alite: a time-resolved quantitative X-ray diffraction approach using the G-factor method compared with heat release, *J. Appl. Crystallogr.* 44 (5) (2011) 895–901.
- [51] D. Jansen, et al., The early hydration of ordinary Portland cement (OPC): an approach comparing measured heat flow with calculated heat flow from QXRD, *Cem. Concr. Res.* 42 (1) (2012) 134–138.
- [52] Á.G. De La Torre, et al., The superstructure of C3S from synchrotron and neutron powder diffraction and its role in quantitative phase analyses, *Cem. Concr. Res.* 32 (9) (2002) 1347–1356.
- [53] K.H. Jost, B. Ziemer, SR, Redetermination of the structure of β-dicalcium silicate, *Acta Crystallographica (B33)* (1977) 1696–1700.
- [54] P. Mondal, J.W. Jeffery, The crystal structure of tricalcium aluminate, Ca₃Al₂O₆, *Acta Crystallogr. B* 31 (3) (1975) 689–697.
- [55] S.A. Markgraf, R.J. Reeder, High-temperature structure refinements of calcite and magnesite, *Am. Mineral.* 70 (5–6) (1985) 590–600.
- [56] P. Comodi, et al., High-pressure behavior of gypsum: a single-crystal X-ray study, *Am. Mineral.* 93 (2008) 1530–1537.
- [57] P. Hartmann, On the unit cell dimensions and bond lengths of anhydrite, *Eur. J. Mineral.* 1 (5) (1989) 721–722.
- [58] F. Goetz-Neunhoeffer, J. Neubauer, Refined ettringite (Ca₆Al₂(SO₄)₃(OH) 12·26H₂O) structure for quantitative X-ray diffraction analysis, *Powder Diffraction* 21 (1) (2005) 4–11.
- [59] T. Runcevski, et al., Crystal structures of calcium hemihydrate and carbonated calcium hemihydrate from synchrotron powder diffraction data, *Acta Crystallogr. B* 68 (5) (2012) 493–500.
- [60] L. Desgranges, et al., Hydrogen thermal motion in calcium hydroxide: Ca(OH)₂, *Acta Crystallogr. B* 49 (5) (1993) 812–817.
- [61] G. Plusquellec, A. Nonat, Interactions between calcium silicate hydrate (C-S-H) and calcium chloride, bromide and nitrate, *Cem. Concr. Res.* 90 (2016) 89–96.
- [62] R. Sposito, N. Beuntner, K.-C. Thienel, Characteristics of components in calcined clays and their influence on the efficiency of superplasticizers, *Cem. Concr. Compos.* 110 (2020), 103594.
- [63] J. Plank, B. Sachsenhauser, J. de Reese, Experimental determination of the thermodynamic parameters affecting the adsorption behaviour and dispersion effectiveness of PCE superplasticizers, *Cem. Concr. Res.* 40 (5) (2010) 699–709.
- [64] M. Celia Magno, et al., A comparison between laser granulometer and sedigraph in grain size analysis of marine sediments, *Measurement* 128 (2018) 231–236.
- [65] L.J. Michot, F. Villieras, Chapter 12.9 surface area and porosity, in: F. Bergaya, B.K. G. Theng, G. Lagaly (Eds.), *Developments in Clay Science*, Elsevier Netherlands, The Netherlands, 2006, pp. 965–978.
- [66] A. Quennoz, K.L. Scrivener, Hydration of C3A-gypsum systems, *Cem. Concr. Res.* 42 (7) (2012) 1032–1041.
- [67] F. Avet, et al., Development of a new rapid, relevant and reliable (R3) test method to evaluate the pozzolanic reactivity of calcined kaolinitic clays, *Cem. Concr. Res.* 85 (2016) 1–11.

M. Maier et al.

Cement and Concrete Research 154 (2022) 106736

- [68] Y. Dhandapani, et al., Towards ternary binders involving limestone additions — a review, *Cem. Concr. Res.* 143 (2021), 106396.
- [69] E. Pustovgar, et al., Influence of aluminates on the hydration kinetics of tricalcium silicate, *Cem. Concr. Res.* 100 (2017) 245–262.
- [70] S. Adu-Amankwah, et al., Effect of sulfate additions on hydration and performance of ternary slag-limestone composite cements, *Constr. Build. Mater.* 164 (2018) 451–462.
- [71] S.T. Bergold, F. Goetz-Neunhoeffer, J. Neubauer, Interaction of silicate and aluminate reaction in a synthetic cement system: implications for the process of alite hydration, *Cem. Concr. Res.* 93 (2017) 32–44.
- [72] E. Gartner, I. Maruyama, J. Chen, A new model for the C-S-H phase formed during the hydration of Portland cements, *Cem. Concr. Res.* 97 (2017) 95–106.

9 Appendix

A list of all publications prepared and talks given during the doctorate:

2022:

- Snellings, R., Almenares-Reyes, R., Hanein, T.; Irassar, E. F., Kanavaris, F., **Maier, M.** et al. (2022). "Paper of RILEM TC 282-CCL: Mineralogical characterization methods for clay resources intended for use as supplementary cementitious material." *Materials and Structures* 55: 149.
- Alujaz Diaz, A., Almenares Reyes, R. S., Hanein, T., Irassar, E. F., Juenger, M., Kanavaris, F., **Maier, M.** et al. (2022). „Properties and occurrence of clay resources for use as supplementary cementitious materials. A paper of RILEM TC 282-CCL." *Materials and Structures* 55: 139.
- Sposito, R., **Maier, M.**, Beuntner, N., Thienel, K.-Ch. (2022). "Physical and mineralogical properties of calcined common clays as SCM and their impact on flow resistance and demand for superplasticizer." *Cement and Concrete Research*, 154: 106743.
- **Maier, M.**, Sposito, R., Beuntner, N., Thienel, K.-Ch. (2022). "Particle characteristics of calcined clays and limestone and their impact on early hydration and sulfate demand of blended cement." *Cement and Concrete Research*, 154: 106736.

2021:

- Hanein, T., Thienel, K.-Ch., Zunino, F., Marsh, A., **Maier, M.**, Wang, B. et al. (2021). "Clay calcination technology: state-of-the-art review by the RILEM TC 282-CCL." *Materials and Structures* 55: 3.
- Sposito, R., **Maier, M.**, Beuntner, N., Thienel, K.-Ch. (2021). "Evaluation of zeta potential of calcined clays and time-dependent flowability of blended cement with customized polycarboxylate-based superplasticizers." *Construction and Building Materials* 308: 125061.
- **Maier, M.**, Scherb, S., Beuntner, N., Thienel, K.-Ch. (2021). „The hydration of C₃A in presence of calcined clays." 3rd International Conference on the Chemistry of Construction Materials (ICCCM 2021), Online.
- Scherb, S., **Maier, M.**, Beuntner, N., Thienel, K.-Ch., Neubauer, J. (2021). "Reaction kinetics during early hydration of calcined phyllosilicates in clinker-free model systems." *Cement and Concrete Research* 143: 106382.
- **Maier, M.**, Scherb, S., Neißer-Deiters, A., Beuntner, N., Thienel, K.-Ch. (2021). "Hydration of cubic tricalcium aluminate in the presence of calcined clays." *Journal of the American Ceramic Society* 104(7): 3619-3631.
- **Maier, M.**, Beuntner, N., Thienel, K.-Ch. (2021). "Mineralogical characterization and reactivity test of common clays suitable as supplementary cementitious material." *Applied Clay Science* 202: 105990.

2020:

- **Maier, M.**, Beuntner, N., Thienel, K.-Ch. (2020). Potential of calcined recycling kaolin from silica sand processing as supplementary cementitious material. *Calcined Clays for Sustainable Concrete - Proceedings of the 3rd International Conference on Calcined Clays for Sustainable Concrete*. S. Bishnoi. Singapore, Springer. RILEM Bookseries Vol. 25: 75-83.
- **Maier, M.**, Beuntner, N., Thienel, K.-Ch. (2020). An approach for the evaluation of local raw material potential for calcined clay as SCM, based on geological and mineralogical data: Examples from German clay deposits. *Calcined Clays for Sustainable Concrete - Proceedings of the 3rd International Conference on Calcined Clays for Sustainable Concrete*. S. Bishnoi. Singapore, Springer. RILEM Bookseries Vol. 25: 37-47.